University of Alberta

Multi-scale Modelling of Structured Reactors

by

Teng-Wang Nien

A thesis submitted to the Faculty of Graduate Studies and Research
in partial fulfillment of the requirements for the degree of

Doctor of Philosophy
in
Chemical Engineering

Department of Chemical and Materials Engineering

Fall 2013
Edmonton, Alberta

Abstract

The overall objective is to research methods for the efficient simulation of structured reactors using models that can capture as much of the real micro scale phenomena as possible within the constraint of running in a realistic amount of computer time. The problem of modelling a complete reactor can be visualized as one of *multi-scale modelling*. Taking monolith reactors as an example, at the molecular level (micro-scale) there are the mechanistic models for the reaction kinetics. The meso scale can be defined as the channel level, in which the diffusion and reaction steps in the washcoat are considered, as is the mass and energy transfer between the fluid in the channel and the solid wall. The macro-scale is defined as the entire reactor that is modelled as a continuum. The challenge is to determine a method to capture the micro-scale information in the macro-scale model. Furthermore, the micro-scale model will be based on data determined in an appropriate experimental apparatus. In this study, the use of data based models for the monolith reactor and a gauze type reactor are explored. The information for the small scales is pre-compiuted and stored in a look-up table, which is accessed during execution of the macro-model. Through the analysis of the CFD simulation, it has been shown that this method can reduce the computation time significantly with good results.

Acknowledgements

First of all I would like to express my deepest appreciation to my supervisor Prof. Robert E. Hayes for the continuous support and guidance of my research and life. What he has done is far beyond my imagination. Needless to say, without his persistent help this dissertation would not have been possible.

I would like to thank Dr. Joe Mmbaga for his patience and positive attitude on everything and Dr. Rajab Litto for his encouragement and inspiring discussion. I would like also thank Dr. Andres Donoso-Bravo for the cooperation and assistance on the ammonia oxidation project. My sincere thanks also go to Anton Fadic for showing his passion of life.

Furthermore I would also like to acknowledge Dr. Martin Votsmeier of Umicore AG with much appreciation for many discussions and instruction in industrial area.

Financial support for this work was provided by the Auto21 Network of Centres of Excellence program and the Natural Sciences and Engineering Research Council of Canada (NSERC) via a Strategic Grant.

Last but not the least, I would like to thank my loved ones, my parents, and family, especially my wife Wan-Ying Lin for her companion and support for many years. And my son Jayden, thanks for coming.

Table of Contents

Chapter 1:

Chapter 2:

Chapter 3:

Chapter 4:

Chapter 5:

Chapter 6:

List of Tables

List of Figures

Chapter 1:

Introduction and Background

1.1 Introduction

The use of mathematical models for physical and chemical systems has been a feature of the scientific and engineering landscape probably since the inception of mathematics itself. The reduction of a complex natural system to a series of equations offers many advantages to the practicing scientist or engineer. Provided that the equations can be solved, computer modelling allows for the rapid evaluation of many design scenarios, can eliminate some experiments and reduce the amount of prototyping that must be done. Computer models can also be used as a diagnostic tool to understand physical and chemical phenomena that cannot be measured easily by experiment.

As any scientist or engineer today is aware, there has been, and continues to be, a rapid evolution in the power of computers. This development is accompanied by increases in the development of sophisticated numerical techniques and commercial software which implements these techniques. The combined result is the ready availability of relatively inexpensive tools for the study of complex chemical and physical systems. A concurrent development with this trend to faster and more reliable computational tools is the desire to solve more complex and advanced problems, on a bigger scale. Thus there remains, and likely will always remain, a need to improve computational methodologies to allow for this latter desire to be realized.

The purpose of the work described in this thesis was to develop some coherent methodologies for the simulation of multi-scale systems. The development of these methodologies is performed in the context of modelling some structured catalytic reactors, primarily the monolith reactor but also a gauze type reactor. In this, the introductory chapter, an outline of the thesis will first be presented. This is followed by a general background of these reactor types, and a discussion of multi-scale modelling in a reactor context.

1.2 Outline of thesis and statement of contributions

This thesis is presented in paper format, and is based on four papers. Two are in print and two more will be submitted shortly. This section describes the outline of the remainder of the thesis, and details my contribution to each paper. Chapters 2, 3, 4 and 5 are each based on a paper that is appeared or will be submitted for publication. In each case, the material presented here is modified to some extent from the publication version. Chapter 6 gives a discussion and analysis of the methodology with some insight into the future directions possible. That chapter finishes with conclusions and recommendations.

As noted, the papers have been modified somewhat, and an effort has been made to eliminate duplication of material. However, to retain completeness in each chapter, and to ensure that each chapter can stand alone, some duplication has remained.

Chapter 1 presents some background information on reactor modelling. Some of this material was from the presentations of Hayes (2009) and Nien et al. (2012).

Chapter 2 is a modified version of the paper:

> T. Nien, J.P. Mmbaga, R.E. Hayes and M. Votsmeier, Hierarchical multi-scale model reduction in the simulation of catalytic converters, *Chemical Engineering Science,* **93** 362-375 2013.

This chapter describes the complete stepwise development of a multi-scale model for a catalytic monolith reactor, from the smallest scale to the full scale reactor implementation. I did all of the work for this paper.

Chapter 3 is a modified version of the paper:

> R. Litto, T. Nien, R.E. Hayes, J.P. Mmbaga, M. Votsmeier, Parametric Study of a Recuperative Catalytic Converter, *Catalysis Today*, **188** 106-112 2012.

The work for this paper was performed during the development of the methods described in Chapter 2. It represents the first effort at coupling the micro-scale methodology (the look-up tables) into a full size reactor model. My contribution was to develop and couple these models into the COMSOL simulator developed by Litto, who subsequently performed most of the reactor simulations.

Chapter 4 is a modified version of the paper:

> A. Fadic, T. Nien, J.P. Mmbaga, R.E. Hayes and M. Votsmeier, A Case Study in Multiscale Model Reduction: Effect of Cell Density on Methane Ignition in Monolith Reactors, to be submitted to the *Cdn J. of Chem. Eng.*

The work for this chapter was done after the work for Chapter 2 was finished. The chapter describes a parametric study of the effect of cell density on the ignition of methane in a monolith reactor. To include correctly all of the heat and mass transfer effects, and to use mechanistic kinetics, required the use of high level look-up tables, described in Chapter 2. My contribution was to develop all of the tables required for the six cell types studied, and to interface them in the larger scale simulation. The simulations were performed by MSc student Anton Fadic.

Chapter 5 is a modified version of the paper:

> A. Donoso-Bravo, T. Nien, J.P. Mmbaga, R.E. Hayes and M. Votsmeier, CFD Modelling of a Gauze Reactor for Ammonia Oxidation, to be submitted

In this paper, the multi-scale methodology is applied to a gauze reactor for ammonia oxidation. The basic COMSOL model for the reactor was developed jointly by me, Mmbaga and Donoso-Bravo. I developed the final model, including the development and implementation of the look-up tables. I ran all of the simulations for the parametric studies reported in the thesis and for the final paper.

In addition to these publications, my work has been or will be presented at the following conferences. The name of the presenter is underlined.

T. Nien, J.P. Mmbaga, R.E. Hayes and M. Votsmeier. CFD Modelling of a Gauze Reactor for Ammonia Oxidation, *ICOSCAR4*, Sep. 2013, Beijing, China.

A. Fadic, T. Nien, J.P. Mmbaga, R.E. Hayes and M. Votsmeier, Effect of Cell Density on Methane Ignition in Monolith Reactors, *ICOSCAR-4*, Sep. 25-27, 2013, Beijing, China.

A. Fadic, T. Nien, J.P. Mmbaga, R.E. Hayes and M. Votsmeier, A Case Study in Multiscale Model Reduction: The Effect of Cell Density on Catalytic Converter Light-Off, *Third International Symposium on Modelling of Exhaust-Gas Aftertreatment*, Badherrenalb/Karlsruhe, September 2013.

T. Nien, R.E. Hayes and M. Votsmeier, Using rate mapping methods for model reduction in the simulation of catalytic converters, *Ninth International Congress on Catalysis and Automotive Pollution Control*, *CAPOC-9*, Brussels, August 2012.

T. Nien, R.E. Hayes and M. Votsmeier, Efficient simulation of catalytic converters using a rate mapping approach, *22th Canadian Symposium on Catalysis*, Quebec City, May 2012.

R. E. Hayes, A. Fadic, T. Nien and J. Mmbaga, Optimization of an Automotive Catalytic Converter using Computational Fluid Dynamics, *XXV Interamerican Congress of Chemical Engineering*, Santiago, Chile, November 2011.

T. Nien, M. Votsmeier and R.E. Hayes, Simulation of a monolith reactor using data mapping methods, *21th Cdn. Symposium on Catalysis*, Banff, May 2010.

T. Nien, C. Sola, R.E. Hayes, J. P. Mmbaga, F.H. Bertrand, M. Votsmeier, Development and Validation of Computational Design Tools for Catalytic Converters, *AUTO21 HQP Meeting*, Hamilton, ON, May 2009

T. Nien, C. Sola, R.E. Hayes, J. Mmbaga and M. Votsmeier, An Investigation of Optimisation Tools for Modelling a Diesel Oxidation Catalyst, *57th Canadian Chemical Engineering Conference,* Edmonton, Oct. 2007.

1.3 Introduction to catalytic reactors

The chemical reactor is at the heart of most process plants, and plays a key role in many pollution abatement technologies (Hayes and Mmbaga, 2012; Heck and Farrauto, 2009). Chemical reactors are classified a number of different ways, but can be broadly separated into *non-catalytic* and *catalytic*. The difference is the presence or absence of a catalyst, whose role is to enhance the reaction rate. Reactors are also divided into homogeneous and heterogeneous. In a homogeneous system, all of the components are in the same phase, including the catalyst, if present. In a heterogeneous system, more than one phase is present. Heterogeneous systems can be catalytic or non-catalytic. For the remainder of this work, we will deal only with heterogeneous catalytic reactors, where the catalyst is present as a solid and the reactants are present in the gas phase.

1.4 Catalyst types

Solid catalysts come in a wide variety of forms, with different shapes and sizes. One of the common types of catalyst consists of a metal, either on pure form, or as an oxide or other compound. For the applications discussed in this thesis, we restrict ourselves to the use of metal catalysts from the precious metals group, i.e. platinum, palladium and rhodium. These metals may be used in their pure metallic form, either singly or as part of a bimetallic alloy. Alternatively, they may be spread out on a porous support to increase the catalytic surface area. The presence of a porous structure in the catalyst introduces important heat and mass transfer effects that must be included in any comprehensive reactor model (Hayes and Mmbaga, 2012).

1.5 Structured catalytic reactors

The catalyst may be present in the reactor in a number of different ways. The most common form of a catalytic reactor is the fixed or packed bed reactor. In this scenario, the catalyst is typically in the form of porous pellets that are randomly dumped into a reactor vessel, forming an unconsolidated porous medium through which the process stream flows. Another form of reactor is the fluidized bed, in which the gas flows upwards through a bed of small diameter catalyst pellets, entraining them and giving the appearance of a fluid. Both of these reactor types are called unstructured reactors, because of the random placing of the catalyst particles.

Structured reactors are those where the reactor internals have some predefined geometric pattern. Two common types, both of which are used in this thesis, are the monolith reactor and the gauze reactor. In the gauze reactor, the catalyst is in the form of screens made from solid wire catalyst, through which the reacting fluid flows. Gauze reactors are typically used where a very short contact time is required. They are discussed further in Chapter 5, which reports on a modelling study for this reactor type as used for the oxidation of ammonia.

The majority of the work presented in this thesis deals with monolith reactors; therefore they will be described here in some detail, and will also be used to illustrate the concept of multi-scale modelling. Monolith reactors are used where there is a desire for a very low pressure drop, and a high geometric surface area for the mass transfer between the fluid and the solid. The monolith substrate is made from either ceramic or thin metal, and consists of thousands or parallel passages or ducts through which the fluid flows. When ceramic is used for the substrate, they are made by extrusion and practically the channels have triangular, hexagonal or square shape. When metal is used, the channels often resemble a sinusoidal shape. The size of the channel varies from about 0.5 mm to several mm, or even cm for larger scale industrial units. The channel size is usually reported as the number of cells per square inch (CPSI). The most common application of monolith reactors is in automotive exhaust gas after treatment systems. In this application, the cell size usually used ranges from 0.5 to about 1 mm. The cells are coated with a porous washcoat that contains a catalyst for this application. Scanning electron micrographs of three washcoated monolith reactors are shown in Figure 1.1 (Hayes and Kolaczkowski, 1994; Hayes, 2009).

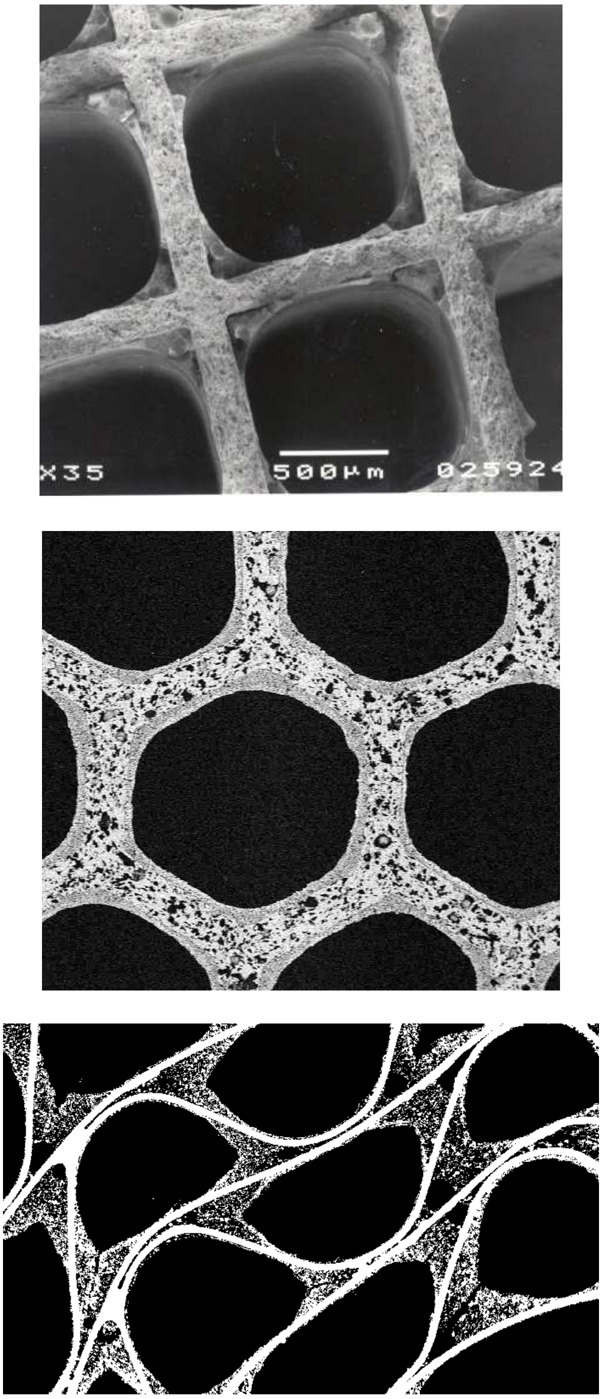

Figure 1.1 - Scanning electron micrographs of monoliths with a catalytic washcoat. Top: Ceramic monolith with square channels (Hayes and Kolaczkowski, 1994). Centre: Ceramic monolith with hexagonal channels. Bottom: Metal monolith with ‘sinusoidal’ channels. (Hayes, 2009)

1.6 Multi-scale modelling

The physical and chemical processes in a catalytic reactor occur on a wide range of spatial and temporal scales. We focus here on the spatial scale only. The smallest scale is the molecular scale, where the reactions occur between species adsorbed on the catalyst surface. This scale is usually represented in a global model via a set of rate equations, either mechanistic or empirical in nature.

When the catalyst is porous, the chemical reaction occurs on the surface of the pores in the catalyst. These pores typically have a size range from a few nanometres to a few tens of nanometres. The reactants and products must diffuse into and out of these pores from the bulk gas at the catalyst external surface.

For a monolith reactor, the next size scale is the channel scale, which, for an automotive application, is around 1 mm in size. The fluid flow in the channel may be in the laminar or turbulent regime. The transport of the reactants from the bulk gas to the catalyst external surface (gas/solid interface) is a key part of the overall reaction rate, and should be modelled correctly.

The final scale in the monolith reactor is the full size converter. In automotive applications, the reactor is of the order of 15 cm in length 10 cm in diameter, although there are many variations. Converters for trucks, especially heavy duty vehicles, are much larger. Even converters for small passenger cars contain upwards of 7000 to 10000 channels.

The normal method to model a catalytic converter is to solve the governing partial differential equations using appropriate numerical method (e.g. finite volume or finite element). These methods require the discretization of the spatial domain into a series of elemental volumes. Clearly, with such a wide variety of scales, this presents a serious challenge. When developing a model for a catalytic converter, therefore, it is clear that many choices must be made. Often, this entails ignoring, or only roughly approximating, the smaller scale phenomena. The problem addressed in this thesis is the development of fast computational methodology that will include all of the small scale information in a rigorous manner, yet still execute on a reasonably priced computer in an acceptable amount of time. The methodology selected for this purpose was to use look-up tables. This method, its history and development, and our subsequent implementation in the context of a catalytic converter are described in Chapter 2.

1.7 Mechanistic kinetic modelling

The various spatial scales described in Section 1.5 present challenges to a modeller. These problems can be compounded by the use of complicated kinetic models. Traditionally, when modelling catalytic converters for automotive and other catalytic combustion applications, relatively simple kinetic expressions are used. Recently, the use of more highly detailed mechanistic kinetics has become popular in these systems (Deutschmann et al., 1996; Mukadi and Hayes, 2002; Salomons, et al., 2007). If these types of kinetic models are coupled to models for the reactor, the execution time required for the resulting simulation is often prohibitive, even with fast computers. In this thesis, we combine detailed mechanistic kinetics with multi-scale models and show how the resulting models can be constructed to execute in relatively small amounts of time.

1.8 Summary

This thesis focuses on the multi-scale model reduction of catalytic reactors to develop computationally efficient models that execute in practicable times. The detailed methodology is developed in Chapter 2 for a catalytic converter for the combustion of methane. A detailed multi-step reaction mechanism taken from the literature is used. Chapters 3 and 4 show some applications of the method, also for methane combustion. Chapter 5 extends the method to a different reactor type, with different reactions, the partial oxidation of ammonia in a gauze reactor. A comprehensive parametric study is presented for this reactor.

References

Deutschmann, O., Schmidt, R., Behrendt, F., Warnatz, J. Numerical modeling of catalytic ignition. Symposium (International) on Combustion 26, 1747–1754, 1996.

Hayes, R.E., Kolaczkowski, S.T., Mass and heat transfer effects in catalytic monolith reactors. Chemical Engineering Science 49, 3587–3599 1994.

Hayes, R.E., Modelling of catalytic converters: Mass, energy and momentum transport. *International Symposium on Modelling of Exhaust-Gas Aftertreatment*, Badherrenalb/Karlsruhe, September 2009.

Hayes, R.E. and Mmbaga, J.P., Introduction to Chemical Reactor analysis, Taylor Francois, New York, 2012.

Heck, R.M. Farrauto, R.J. Gulati, S.T., Catalytic Air Pollution Control, Commercial Technology, Wiley, New York, 2009.

Mukadi, L.S., Hayes, R.E. Modelling the three-way catalytic converter with mechanistic kinetics using the Newton-Krylov method on a parallel computer, *Computers and Chemical Engineering,* **26**(3) 439-455 2002.

Nien, T., Hayes, R.E., Votsmeier, M., Efficient simulation of catalytic converters using a rate mapping approach, *21th Canadian Symposium on Catalysis,* Quebec City, May 2012.

Salomons, S., Hayes, R.E., Votsmeier, M., Drochner, A., Vogel, H., Malmberg, S., Gieshoff, J., On the use of mechanistic CO oxidation models with a platinum monolith catalyst, *Applied Catalysis B: Environmental*, **70**(1-4) 305 - 313 2007.

Chapter 2:

Hierarchical multi-scale model reduction in the simulation of catalytic converters

Overview

This paper presents a methodology for multi-scale modelling using pre-computed data for the small scales. By pre-computing the required data at the micro and meso scales and storing them in a look-up table, these small-scale effects can be captured in a macro scale model that executes with practicable execution times. The methodology is presented in the context of modelling a washcoated monolith reactor for the catalytic combustion of methane using a detailed multistep mechanistic model. The modelling is illustrated as a sequence of steps of increasing model simplification. In the first instance, only the reaction rates are pre-computed. Then the washcoat diffusion is included using a 2D axisymmetric model with a washcoat of uniform thickness, then with a non-symmetrical channel with a washcoat of non-uniform thickness. It is shown how a simple 1D single channel model can accurately account for the presence of a non-uniform washcoat. Finally, the external transport resistance is included in the pre-computation step, and it is shown that a simple one dimensional pseudo-homogeneous single channel model can be used provided the effective average rates are appropriately calculated. Execution times are shown to decrease by several orders of magnitude at minimal loss of solution accuracy. The use of pre-computed data allows for the inclusion of complex heat and mass transfer phenomena, as well as complex kinetics in full scale converter models at relatively small computational cost. The implementation of look-up tables into full scale CFD models is described, and optimal strategies proposed.

This chapter is a modified version of the paper --- **T. Nien,** J.P. Mmbaga, R.E. Hayes and M. Votsmeier, Hierarchical multi-scale model reduction in the simulation of catalytic converters, *Chemical Engineering Science*, **93** 362-375 2013.

2.1 Introduction

The treatment of automotive engine exhaust using catalytic converters is essential to meet government mandated limits on the emission of carbon monoxide (CO), oxides of nitrogen (NO_X) and hydrocarbons (HC). Since their introduction *circa* 1975, catalytic exhaust gas after treatment (CEGAT) systems have become increasingly complicated, especially for lean burn engines. Although early development was largely empirical, computer aided design methodologies are now routinely being used in the development of catalytic converters. These methods require appropriate mathematical models, which ideally should have low execution times, especially for process control models. Modelling the converter is an exercise in multi-scale modelling, with length scales ranging from nanometres (catalyst pore level), micrometres (washcoat level), through millimetres (channel scale) to centimetres (converter scale). Ideally, a model should capture accurately all of the physics and chemistry that occur at each level, however, if this type of simulation is carried out using traditional solution methodologies, the computational requirements are too demanding to be practicable.

To set the context for this work, and to clarify where the most efficient cost saving measures can be introduced, the different modelling scales and their phenomena are briefly reprised. The reactor used for CEGAT has a monolith honeycomb design consisting of thousands of parallel channels, the surfaces of which are coated with a washcoat containing a catalyst. The channels, which have a dimension of one mm or less, can have a variety of cross sectional shapes, including square, hexagonal, and triangular (Hayes et al., 2004, 2009). Because of the manufacturing method, the washcoat layer is usually non-uniform in thickness around the channel perimeter. Typical variations of washcoat thickness in square channels range from less than 10 micrometres at the sides of the channels to 150 micrometres or more in the corners, measured diagonally (Hayes and Kolaczkowski, 1994). The reacting fluid flows down the channel in the laminar regime, the reactants diffuse to the gas solid interface, thence diffuse into, and react within, the washcoat. Large internal and external mass transfer resistances are often present (Leung et al., 1996). Molecular diffusion through a boundary layer controls transport of reactants to the washcoat surface. The diffusion into the washcoat occurs in pores on the nanometre scale, and follows a tortuous path.

Models for CEGAT systems can be divided into two types, the single channel model (SCM) and the entire converter model (ECM). Each of these two model types exists in several forms, depending on the underlying approximations. As with all reactor simulations, we may utilize fully discrete models, in which the full spatial domain of both fluid and solid are resolved. Most single channel models are discrete. If the complete space of each phase is modelled the result is a distributed parameter system. If the number of space dimensions is reduced by using average values for any parameter, the result is a lumped parameter model.

We consider first the SCM. As noted earlier, the channel is rarely if ever axi-symmetric, and thus a correct representation of it requires a spatially three dimensional model. The partial differential equations that describe the reactor behaviour are usually solved using the finite volume or finite element methods. The scale difference between the washcoat and channel, and also the aspect ratio between the transverse and axial dimensions of the channel, implies that an accurate solution may require a mesh consisting of many thousands, possibly hundreds of thousands of degrees of freedom (DOF), leading to long computational times, especially if the momentum balance equation is included (Raja, et al., 2000; More et al., 2006). For steady state simulations, the three dimensional shape can be approximated using a pseudo 3D model where the axial diffusion terms are ignored (discussed in more detail later in this paper) (Votsmeier, 2009), but a transient model requires the full spatially 3D solution. Even at this high level of simulation, the porous nature of the washcoat is normally approximated with a continuum model using an effective diffusion coefficient (Hayes and Kolaczkowski, 1997), although there are some recent papers that attempt to model diffusion in the actual porous micro-structure of the washcoat (e.g. Koci, et al., 2010). We note without further discussion that the continuum model is adopted for the washcoat throughout the present work.

The three dimensional SCM being so expensive to solve for routine work, the first level of approximation is to use a geometric re-parameterization, and to model the monolith channel as a right circular cylinder with a uniform thickness of washcoat in the form of an annulus (Hayes and Kolaczkowski, 1997). The resulting axisymmetric domain can then be solved as a 2D problem using cylindrical coordinates. Although this 2D solution domain can still result in extended execution times, it is vastly faster to execute than the 3D models, and thus is much more common in the literature. Correct mapping of the 3D geometry into two dimensions can yield close approximations between the 2D and 3D solutions, however, it has been shown (Hayes et al., 2004; More et al., 2006) that there are situations under which the approximate 2D solution deviates markedly from the 3D one. In particular, it has been shown (Hayes et al. 2004, 2005) that the fillet shape of washcoat can generate different average reaction rates compared to a uniform washcoat of equivalent cross sectional area at the same surface temperature and reactant concentration, especially for intermediate values of the effectiveness factor. The significance of these effects is examined shortly.

The 2D and 3D models are both distributed parameter models. Further simplification can be made by using fewer model dimensions than physically exist, which results in a lumped parameter model. These models typically use a one dimensional approximation for either or both of the channel or the washcoat. To reduce the channel to 1D, it is necessary to ignore radial variations in concentration and temperature in the fluid, and to express the fluid phases in terms of mixing cup temperature and concentration (lumped parameters). This approximation creates a discontinuity at the wall (gas/solid interface) that is incorporated using heat and mass transfer coefficients. The choice of these heat and mass transfer coefficients determines the accuracy of the simulation, and much attention has been paid to their correct selection, especially in the developing flow region (e.g. Groppi, et al., 1995; Hayes and Kolaczkowski, 1999; Gupta and Balakotaiah, 2001). A suitable model for the washcoat and wall must be coupled to the 1D fluid model, and there are essentially two options. The first would use a full 2D model for the washcoat and wall (Hayes et al., 2007). The second would be to use a lumped model for the wall as well, and to solve a 1D problem in the axial direction. The average reaction rate at each point on the wall can be computed using an effectiveness factor, or by solving a local 1D diffusion reaction problem in the depth of the washcoat. Both methods usually assume a uniform washcoat thickness. This approach of modelling only the depth coordinate of the washcoat is sometimes used when the gas phase is modelled in two dimensions; the model being called the 2D-1D model (Hayes et al., 1996). The SCM discussed thus far are all what is referred to as heterogeneous models, because both fluid and solid phases are separately considered. At the simplest level, a one dimensional SCM might ignore the washcoat entirely and express the reaction rate in terms of the mixing cup conditions of the fluid in the channel, which is equivalent to ignoring both internal and external mass transfer effects. This type of model is called a pseudo-homogeneous model.

If we consider the model for the entire converter (the ECM), then the practical choices are limited. A fully discrete model that includes a spatial discretization at the channel and washcoat level (such as used in the 2D and 3D SCM) for even a small monolith section is computationally very expensive to solve, even with specialized modelling methods (Bertrand et al., 2012). Thus the monolith is usually approximated using a continuum model, where it is represented as a porous medium with appropriate axial and transverse permeability (Liu et al., 2007; Hayes et al., 2012). The use of volume averaging inherent in such a model results in a loss of all spatial resolution at the channel level, and the models are all in effect lumped parameter models at the channel scale, although they are distributed parameter models at the converter scale. In effect the continuum approach uses a one dimensional model to represent the channels, and thus the issues of the correct representation of the heat and mass transfer coefficients, and the average reaction rate in the washcoat, are again paramount. A compromise is the representative channel method, in which only a few channels are modelled in detail and an interpolation made between them (e.g.

Groppi and Tronconi, 1996; Tischer, et al, 2001). For computational reasons, only a few channels are considered in detail. If the representative channels are modelled as one dimensional, the model is equivalent to a continuum model.

The use of both pseudo-homogeneous and heterogeneous models for the SCM was mentioned. In a pseudo-homogeneous model, the reactor is considered to be a single phase, and there is no differentiation between the fluid and solid temperatures or concentrations. In effect, all mass and heat transfer resistances are ignored. This type of model is common for packed bed reactors and has been used for monolith systems. Although it is rare in single channel models, the concept can be used, as mentioned earlier. On the other hand, the heterogeneous model considers both the fluid and solid temperatures and concentrations. We stress that the coordinates of fluid and solid properties are the same, because the spatial resolution has been lost.

All of these modelling difficulties exist regardless of the rate expressions used. Indeed, even for simple kinetic models the computational requirements can be profound for 3D models. These difficulties are magnified by orders of magnitude when complex kinetic schemes with many species (possibly hundreds) are introduced. Recently, the use of highly detailed mechanistic kinetics has become popular in the modelling of CEGAT and other catalytic combustion systems (Deutschmann et al., 1996; Mukadi and Hayes, 2002; Salomons, et al., 2007). From a modelling perspective, the ideal solution for an ECM would be one that can use a detailed mechanistic model, capture correctly the internal and external heat and mass transfer resistances in the real washcoat and channel shape, yet still execute in a reasonable amount of time. To achieve this objective, new modelling paradigms must be used. A first step towards the development of such fast monolith reactor models was reported by Votsmeier (2009), who used the concept of repro-modelling to reduce the computation time spent on the calculation of mechanistic reaction rates. This work was extended by Votsmeier et al. (2010) and Scheuer et al., (2011, 2012).

In this chapter, we adopt a hierarchical approach to present a systematic study of multi-scale model reduction by successive implementation of pre-computed source terms, which include reaction, and heat and mass transfer effects. We show how the small scale detail can be preserved at the macro level by the correct selection of the pre-mapped source terms. This work follows on from Votsmeier (2009), and the reader is referred there for more detail. In the following sections, the background is summarized for completeness. We explore the use of these data mapped models for SCM and ECM, and demonstrate their implementation in discrete and continuum models. Heterogeneous and pseudo-homogeneous approximations are discussed.

2.2 Development of pre-computed data

As mentioned in the introduction, the use of detailed mechanistic kinetics for the solution of reactor problems poses a severe numerical challenge. A proposed solution is to pre-compute the reaction rates over some solution space, and store the result in an efficient manner in a look-up table. During the execution, the look-up table is simply accessed for the solution at the desired temperature and concentration. Although the look-up table can be expensive to build, once built it can be used for many applications, provided that a sufficiently broad range of parameters is selected. The use of pre-computed rate data for complex reacting flows was pioneered in the field of gas phase kinetics (where it is sometimes called repro-modelling), see for example (Meisel and Collins, 1973; Turanyi, 1994a, 199b). Some work has also been done in 3D simulation with complex kinetics using In Situ Adaptive Tabulation (ISAT) (Kumar and Mazumder, 2010), a technique reported by Pope (1997) which gave some speed-up. The use of surface B-splines fitting in adsorption processes has also been reported (Santos, et al, 2010).

The key issues arising in repro-modelling include the selection of the overall methodology, identification of key species, construction of the solution maps, etc. In this work, we use multivariate spline functions to represent the rate data on a regular multi-dimensional grid. Multi-dimensional splines can be efficiently evaluated if the coefficients of the individual polynomials are pre-computed and stored in a database.

2.3 Modelling methane combustion with a look-up table

Although there are many mechanistic heterogeneous models extant, for illustration purposes we selected the model for the catalytic combustion of methane over a platinum catalyst, as described by Deutschmann et al., (1996), with their model parameters. This model and its variations are widely used in the literature. If we ignore the gas phase reactions, we are left with 24 surface reactions and 11 surface species, plus the gas phase species (methane, water and oxygen). The calculation of source terms (reaction rates) for each of the gas phase and adsorbed species was done as described in Deutschmann et al. (1996). We assume that the adsorbed surface species are in equilibrium with the given gas phase composition. This assumption is reasonable considering the time scales for adsorption and reaction. In the first instance, the source terms are calculated using the open source software package Cantera (Goodwin, 2003).

For the first level of model reduction, we simply build a look-up table to replace the reaction rate terms generated by Cantera, which can subsequently be used in a reactor simulator. This step is essentially the same as followed by Votsmeier (2009), and is briefly described here for completeness. For identification purposes, we shall refer to this look-up table as T1.

The first step in building the table is to identify the important parameters. In this case, the significant gas phase concentrations are methane, oxygen and water, with a fourth variable being the temperature. It is then necessary to decide the parameter space that the look-up table will cover. A table covering a broad range of parameters will be more generally useful, however, an application specific table covering a smaller range will be cheaper to build and access. In any case, we elected to use the range of parameters shown in Table 2.1.

Table 2.1 - The range of each parameter used in the look-up table.

Parameter	Minimum	Maximum
Temperature	600 K	1200 K
Methane concentration	0.1 ppm	1 %
Water concentration	1 ppm	10 %
Oxygen concentration	4 %	20 %

After selecting the parameter space, it is necessary to train the look-up table, which is equivalent to determining its resolution (or dimensionality). The general procedure is to increase the size of the look-up table gradually, and at each step to compute a prediction error. To this end, we used a data test set consisting of 10,000 combinations of the four parameters. The accuracy of the look-up table was then evaluated by calculating an error using this test set and the equation:

$$error = \left[\sum_{i=1}^{N} \frac{1}{N} \left(\frac{R_i - R_{\mathrm{spline},i}}{R_i} \right)^2 \right]^{0.5} \tag{2.1}$$

The initial table contains two values only for each parameter, being the end points of the solution space; this table is denoted [2 2 2 2]. The next step is to build four new tables; in each table the dimensionality is increased for one of the parameters, thus leading to tables denoted [3 2 2 2], [2 3 2 2], [2 2 3 2], and [2 2 2 3]. The table that gives the lowest error was accepted, and this became the new starting point. The next set of four tables was built in a similar manner, and the process continued until an acceptable error was achieved. The evolution of the error and the size of the table are given in Table 2.2. From this table it can be seen that the most significant parameter is the concentration of methane, with the others having roughly equal weight. The final table size will depend on the range of parameters selected. A graphical depiction of the evolution of the relative error for three different spline types is given in Figure 2.1. Both results show that the cubic spline approximation gives the lowest residual error, followed closely by the quadratic spline. The example calculation of the smallest table [2 2 2 2] is descripted in appendix.

Table 2.2 - The evolution of the grid number for each parameter for lookup table T1

Step	Percent error			Parameter				Total entries
	Linear	Quadratic	Cubic	*T*	CH_4	H_2O	O_2	
1	80.47%	80.47%	80.47%	2	2	2	2	16
2	62.60%	53.07%	53.07%	3	2	2	2	24
3	46.80%	29.04%	29.04%	3	3	2	2	36
4	40.90%	22.31%	22.14%	3	5	2	2	60
5	31.73%	12.35%	12.74%	3	5	2	3	90
6	17.53%	4.57%	4.31%	5	5	2	3	150
7	14.15%	3.26%	3.24%	5	9	2	3	270
8	10.59%	2.31%	2.45%	5	9	2	5	450
9	9.73%	1.42%	1.24%	5	9	3	5	675
10	5.10%	0.84%	0.78%	9	9	3	5	1215
11	4.82%	0.44%	0.32%	9	9	5	5	2025
12	3.67%	0.25%	0.23%	9	17	5	5	3825
13	2.59%	0.13%	0.17%	9	17	5	9	6885
14	2.51%	0.11%	0.09%	9	17	9	9	12393
15	2.28%	0.11%	0.09%	9	33	9	9	24057

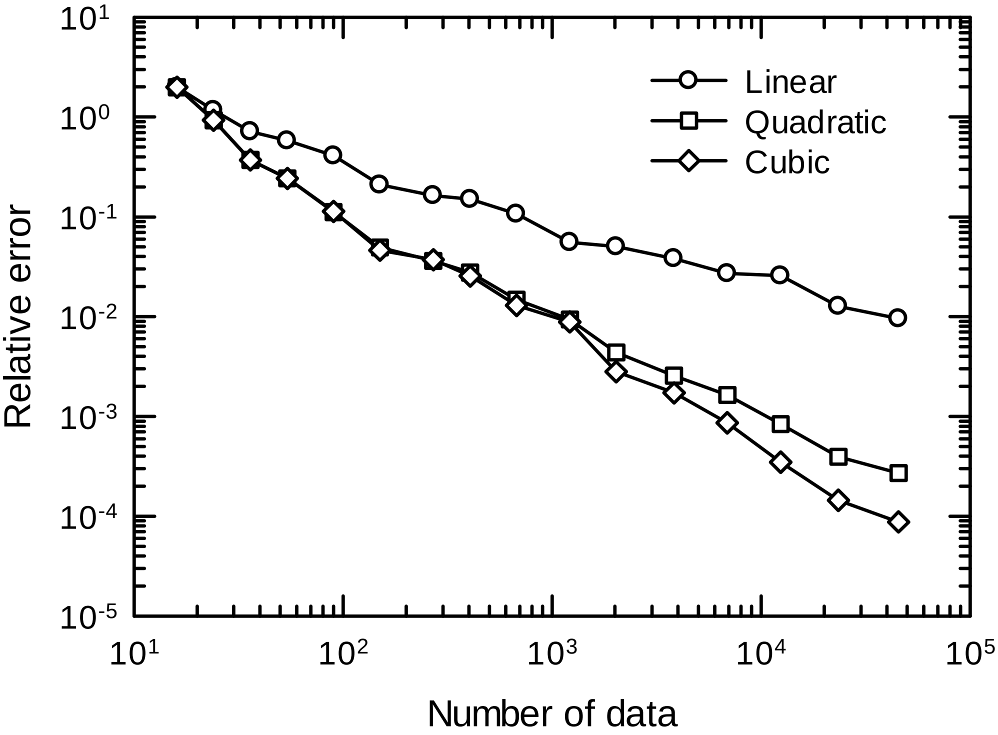

Figure 2.1 - The relative error vs. the number of pre-computed data for lookup table T1.

Both quadratic and cubic splines give acceptable results with a reasonable number of data points. Two comparisons can be made between the two spline types; the execution time required to access the tables, and the amount of storage required. Figure 2.2 shows the execution time required to compute 10,000 data points using the two splining methods. Figure 2.3 compares the storage required. Not surprisingly, cubic splines require more time and storage, although for the examples shown here the differences were not important. For the remainder of this work, we used cubic splines. We used the same methodology to construct all of the look-up tables described in this chapter, and Chapters 3 and 4.

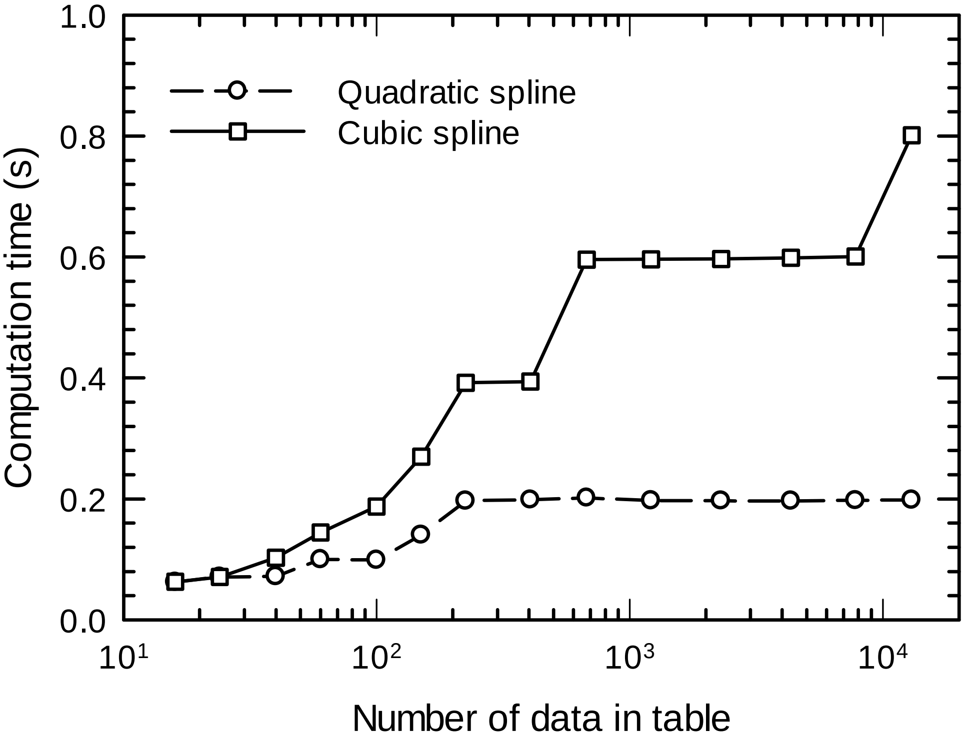

Figure 2.2 - The time required to calculate 10,000 data points using quadratic and cubic spline methods, as a function of lookup table size.

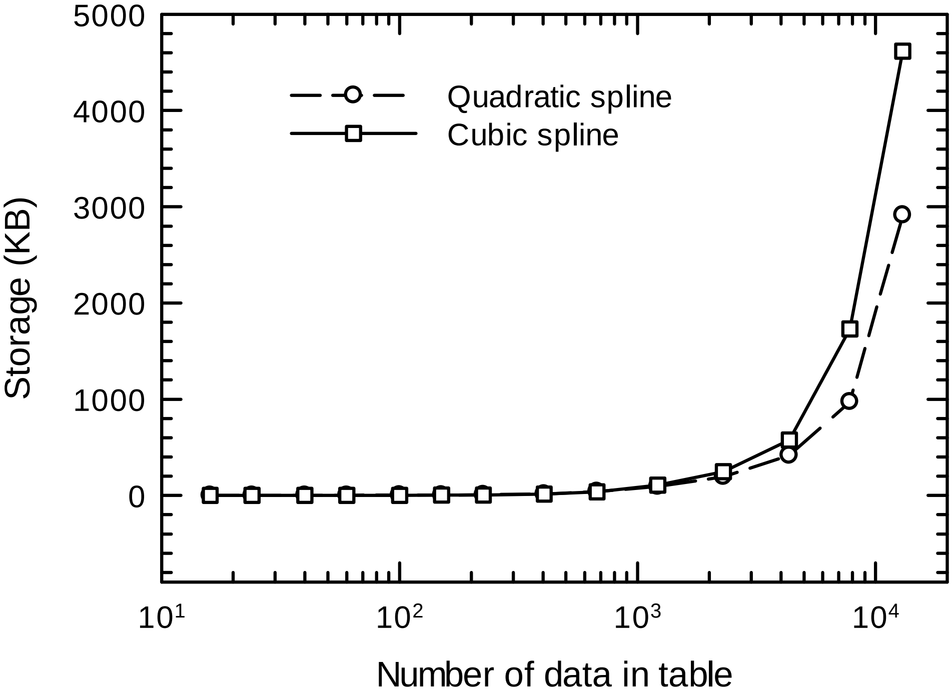

Figure 2.3 - The storage needed for lookup tables as a function of table size.

2.4 Validation of primary (T1) look-up table

The look-up table T1 described in the foregoing is essentially the same as the one generated by Votsmeier (2009), which was demonstrated to be successful in reproducing the results in a single channel monolith reactor. He used a 3D model of the channel; however, we will begin with an axi-symmetric model of the single monolith channel. As discussed in the introduction, this representation is commonly employed, and uses a uniform washcoat thickness. The relevant chemical and physical parameters used in the model are given in Table 2.3.

Table 2.3 - Simulation parameters for light-off curves used with the uniform washcoat case.

Channel radius	5.643×10^{-4} m
Channel length	1.5×10^{-1} to 2.5×10^{-1} m
Thermal conductivity of wall	1.5 W/(m·K)
Thermal conductivity of washcoat	0.75 W/(m·K)
Thickness of the washcoat layer	5.19×10^{-5} m
Mole fraction of methane	0.5 %
Mole fraction of oxygen	20 %
Mole fraction of Water	0.0001 %

For completeness, we give the conservation equations for the channel (Hayes et al., 1992). We considered steady state simulations. In this first case we solved the mass and energy balances in the fluid and the washcoat. The fluid phase mass and energy balances for species *i* are:

$$\nabla\left(D_i\,\rho\nabla w_i\right)-\rho v_z\nabla w_i = 0 \tag{2.2}$$

$$\nabla\left(k_f\nabla T\right)-\left(\rho\,C_P\right)_f v_z\nabla T = 0 \tag{2.3}$$

We did not solve the momentum balance, but rather imposed a fully developed parabolic velocity profile that was corrected for the local temperature according to the ideal gas law (Hayes et al., 1992). Thus the velocity has only an axial component, the value of which depends on the radius. Conceptually, there would be no difference in adding the momentum balance equation if, for example, it was considered important to capture accurately the radial velocity gradients. These might be significant in the entrance region and areas of sharp temperature rise. The steady state mass and energy balances in the washcoat are:

$$\nabla\left(D_{\mathrm{eff}}\,\rho\nabla w_i\right) + S_i = 0 \tag{2.4}$$

$$\nabla\left(k_{\mathrm{eff}}\nabla T\right) + \left(\Delta H_R\right)S_{\mathrm{CH_4}} = 0 \tag{2.5}$$

The source term is the rate of formation by chemical reaction. The diffusion coefficients in the gas phase were calculated using the correlations of Fuller (Hayes and Kolaczkowski, 1997). The diffusion coefficients in the washcoat were calculated assuming that Knudsen diffusion dominates in the pores. The effective diffusion thus depends on temperature and molecular mass of the species. The formula for the effective diffusion coefficient is:

$$D_{\mathrm{eff}} = 4.85\times10^{-7}\sqrt{T/M_i} \quad \frac{\mathrm{m}^2}{\mathrm{s}} \tag{2.6}$$

The simulations were performed using COMSOL Multiphysics (versions 3.5, 4.2a and 4.3). The look-up table was constructed with the aid of MATLAB using the splining toolbox (De Boor, 1978), and the interface to Cantera was done via a MATLAB framework.

The solution domain (channel and washcoat) was meshed using a structured rectangular mesh with 100 quadratic elements in the axial direction. There were 10 elements in the fluid radial direction and 20 in the depth of the washcoat, giving 1000 fluid elements and 2000 washcoat elements. Note that we have not included the substrate in these illustrative examples. For steady state simulations, the effect of the substrate is to increase the axial conduction through the solid phase, which effect we are thus not considering here. A series of steady state simulations was performed at constant inlet velocity with a stepwise increasing inlet temperature. For each run the fractional conversion at the outlet was determined. In the first case the reaction source terms were calculated using Cantera, and in the second case the look-up table T1 was used. A variety of monolith lengths and inlet velocities was tested. A typical result is shown in Figure 2.4, which compares the fractional conversion as a function of inlet temperature (steady state light-off curve) for the two cases. It is evident that the results are essentially the same. A comparison of the execution times for the two methods is given in Table 2.4. Using look-up table T1 gives a 40 to 50 fold increase in execution speed compared to the use of Cantera. The timings reflect the use of a 2.00 GHz Intel® Core™ Duo T2450 processor with 3 GB of RAM.

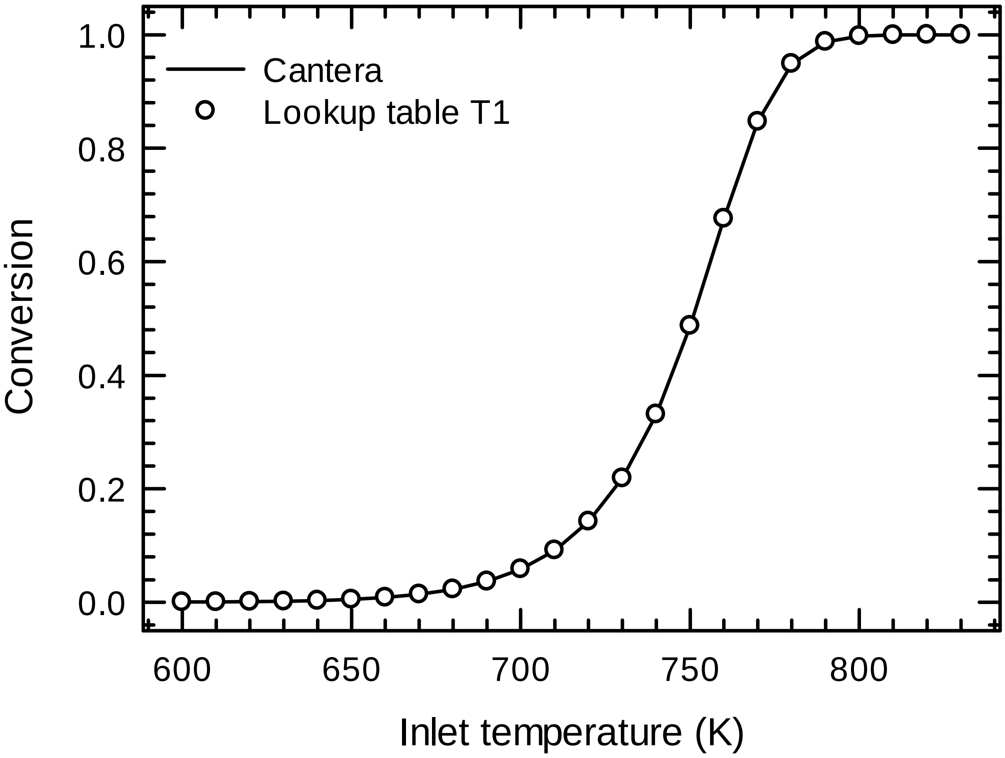

Figure 2.4 - Comparison of the light-off curves built by lookup table T1 and Cantera. The two dimensional axi-symmetric model was used.

Table 2.4 - The simulation time of different approaches.

Tin	Simulation time (s)		
	Cantera	T1	T2
600	911.5	35.8	4.5
650	2036.2	49.7	4.6
700	2407.9	51.1	4.6
750	2831.6	50.1	4.9
800	3601.4	69.1	6.2

2.5 Second level model reduction:
Incorporating washcoat diffusion in the table

It is clear from the results presented thus far that the look-up table T1 is able to replace the use of Cantera in the model with a considerable cost saving, and Votsmeier (2009) concluded as much. The next logical extension of the model reduction process is to include the effects of internal transport resistance (washcoat diffusion) in a look-up table. This would obviate the necessity of solving the diffusion reaction problem in the washcoat during the reactor simulation. It is well known (Hayes and Kolaczkowski, 1997) that inclusion of washcoat diffusion in the model gives a large increase in execution times. To eliminate the washcoat diffusion, it is necessary to have the values of the effective average reaction rate at the catalyst external surface. The problem then is transposed to the best method to approximate this value. The obvious solution is to approximate the diffusion reaction problem in the washcoat by a one dimensional problem, that is, to ignore the axial diffusion in the washcoat. This assumption is considered reasonable (Leung et al. 1996), and is the same approximation used in the so-called 2D-1D model of the channel (Hayes et al., 1996). Thus, in the washcoat annular ring we solve the mass balance:

$$\frac{1}{r}\frac{d}{dr}\left(D_{\mathrm{eff}}\,\rho\, r\frac{d w_i}{d r}\right) + S_i = 0 \qquad (2.7)$$

The boundary conditions are an imposed mass fraction and temperature at the fluid/washcoat interface, and a zero flux condition at the washcoat/substrate interface. The washcoat is considered isothermal, which has been shown to be a good approximation for a thin washcoat (Leung et al. 1996), and which we also observed for the simulations reported here. Invoking this assumption gives the method for the construction of a look-up table that we call T2, which contains the spline coefficients necessary to compute the average reaction rate for a given set of surface conditions. The general scheme for building the table T2 follows that used for T1. That is, we use a training dataset, and alter the table's dimensionality until the required error tolerance is reached. The difference is that instead of simply calling Cantera to compute a reaction rate, we solve a 1D diffusion reaction problem over the thickness of the washcoat for specified surface temperatures and concentrations. One can use T2 to generate either an average reaction rate (in kg/m^{3}s, based on washcoat volume) or the flux at the surface (in kg/m^{2}s based on the gas/solid interfacial area). We store the flux (as will be seen later this is very convenient), which can then be used directly as a boundary condition at the reactor wall in the 2D model. The mass and energy balances are given by Equations (2.2) and (2.3) as before, but subject to the following boundary conditions at the wall:

$$-D_i\,\rho\left(\frac{\partial w_i}{\partial r}\right)_{r=R} = \left(N_i\right)_2 \qquad \text{and} \qquad -k_f\left(\frac{\partial T}{\partial r}\right)_{r=R} = \left(\Delta H_{\mathrm{CH_4}}\right)\left(N_{\mathrm{CH_4}}\right)_2 \qquad (2.8)$$

Here N_i is the mass flux of species i in kg/m^{2}s of surface, where a positive value signifies a flux into the washcoat. The subscript 2 denotes that the value is obtained from table T2. We also point out that the construction of table T2 can be facilitated by using T1. That is, rather than computing the local rates in the washcoat depth from Cantera, we obtain these values from Table T1 because we know it is a good approximation for the rate. We built T2 using both Cantera and T1, and observed that the results were essentially the same, with the construction using T1 being appreciably faster. The relative error trajectories obtained during the training of table T2 are shown in Figure 2.5 for the three spline types.

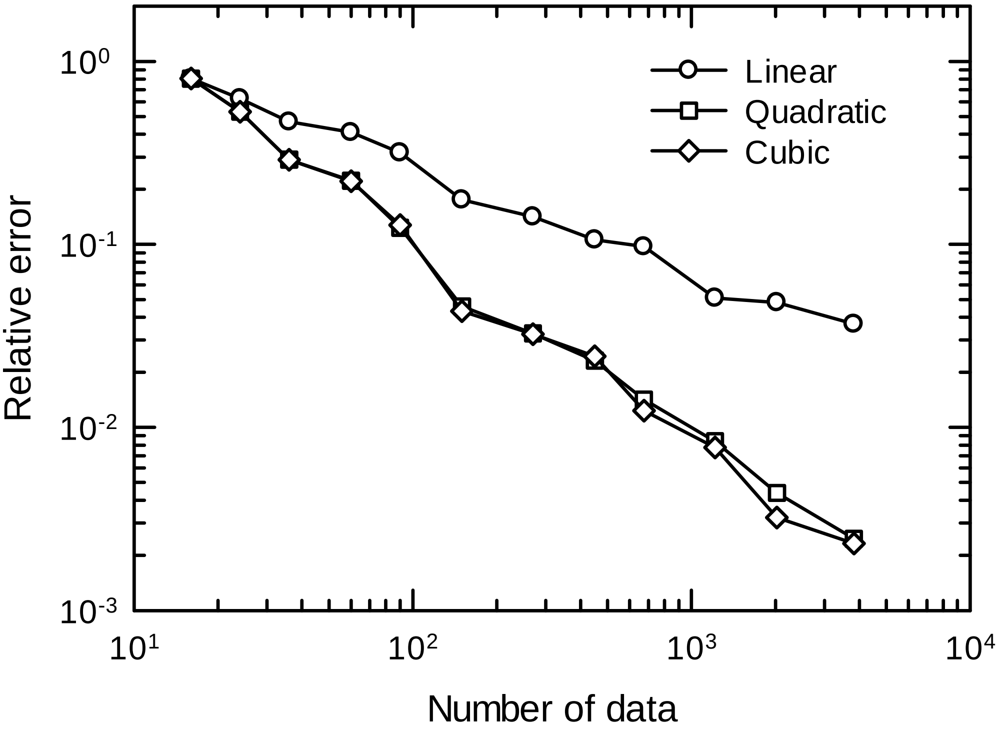

Figure 2.5 - The relative error vs. the number of pre-computed data of lookup table T2.

One advantage of using a 1D approximation for the washcoat depth is the ability to use a much larger number of elements for the washcoat than is realistically possible for the 2D model. Although, for the parameter values studied here, a mesh of 20 radial elements was found to be sufficient, under some scenarios of very low effectiveness factors an extremely fine mesh might be required near the surface, and this modelling paradigm allows for that eventuality.

The use of Equations (2.2) and (2.3) with the boundary conditions of Equation (2.8) obtained from the lookup table does not account for the effect of axial conduction of energy in the solid. In the examples presented here, we have only the thin washcoat, and thus do not expect a significant error to be introduced by neglecting this term. If it is desired to include axial conduction in the wall, there are two options. In the first option, one could simply use a two dimensional representation of the wall, along with the 2D representation of the channel. The thickness of the washcoat could be added to the wall, or simply ignored. The look-up table would generate a source term as before. However, the radial temperature gradients in the wall are usually small, and it is simpler to use a lumped capacitance 1D problem for the wall. The general algorithm would be similar to that proposed by Hayes et al. (1992), which is briefly described here. The 1D energy balance for the solid at steady state is:

$$\frac{A_C}{P}\frac{d}{dz}\left(k_S\frac{dT_S}{dz}\right)+k_f\left(\frac{\partial T_f}{\partial r}\right)_{r=R}+\left(-\Delta H_R\right)\left(N_{\mathrm{CH_4}}\right)_2 = 0 \tag{2.9}$$

A_C is the cross sectional area of the solid, and P is the channel perimeter. The solid temperature obtained by the solution of this equation becomes a boundary condition for the energy balance of the fluid phase, rather than the flux term used in Equation (2.8). See Hayes et al. (1992) for details.

The results from T1 and T2 are first compared using the conversion of methane along the channel at different inlet temperatures. The results are shown in Figure 2.6 for a 15 cm long monolith, where it is seen that the agreement between the two methods is good. Table 2.4 also shows the increase in execution speed resulting from the use of T2. Note that, for consistency, the execution times in Table 2.4 correspond to the 25 cm monolith with an inlet velocity of 0.5 m/s. Generally, we observed about an order of magnitude increase in the speed. This speed-up factor will be mesh dependent, so when a finer mesh is required to model steep gradients in the washcoat then a larger speed-up factor would be expected..

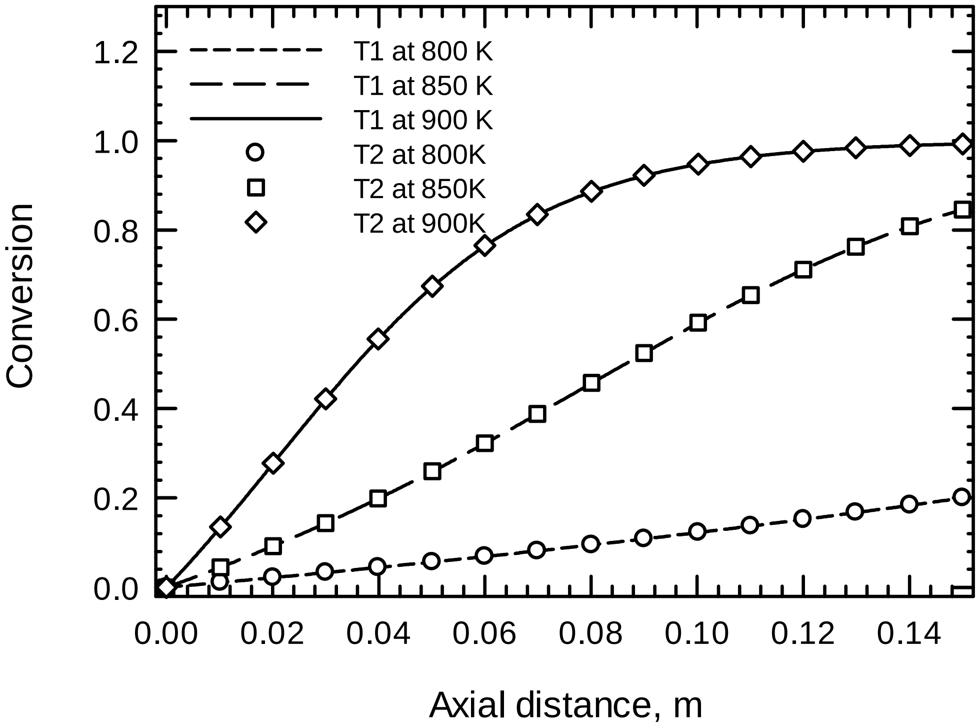

Figure 2.6 - Axial conversion profiles obtained with lookup tables T1 and T2 at three reactor inlet temperatures.

For the simulations shown thus far, the effectiveness factors were all greater than about 0.7. One might expect that the T2 table would be better at higher effectiveness factors, and therefore the comparisons were repeated with lower values of effectiveness factor. The inlet velocity was increased, so that to achieve complete conversion a higher temperature was required, which in turn decreases the effectiveness factor. The steady state light-off curves for different inlet velocities are shown in Figure 2.7(a). Again, we see good agreement in all cases, which shows that the approximation is valid.

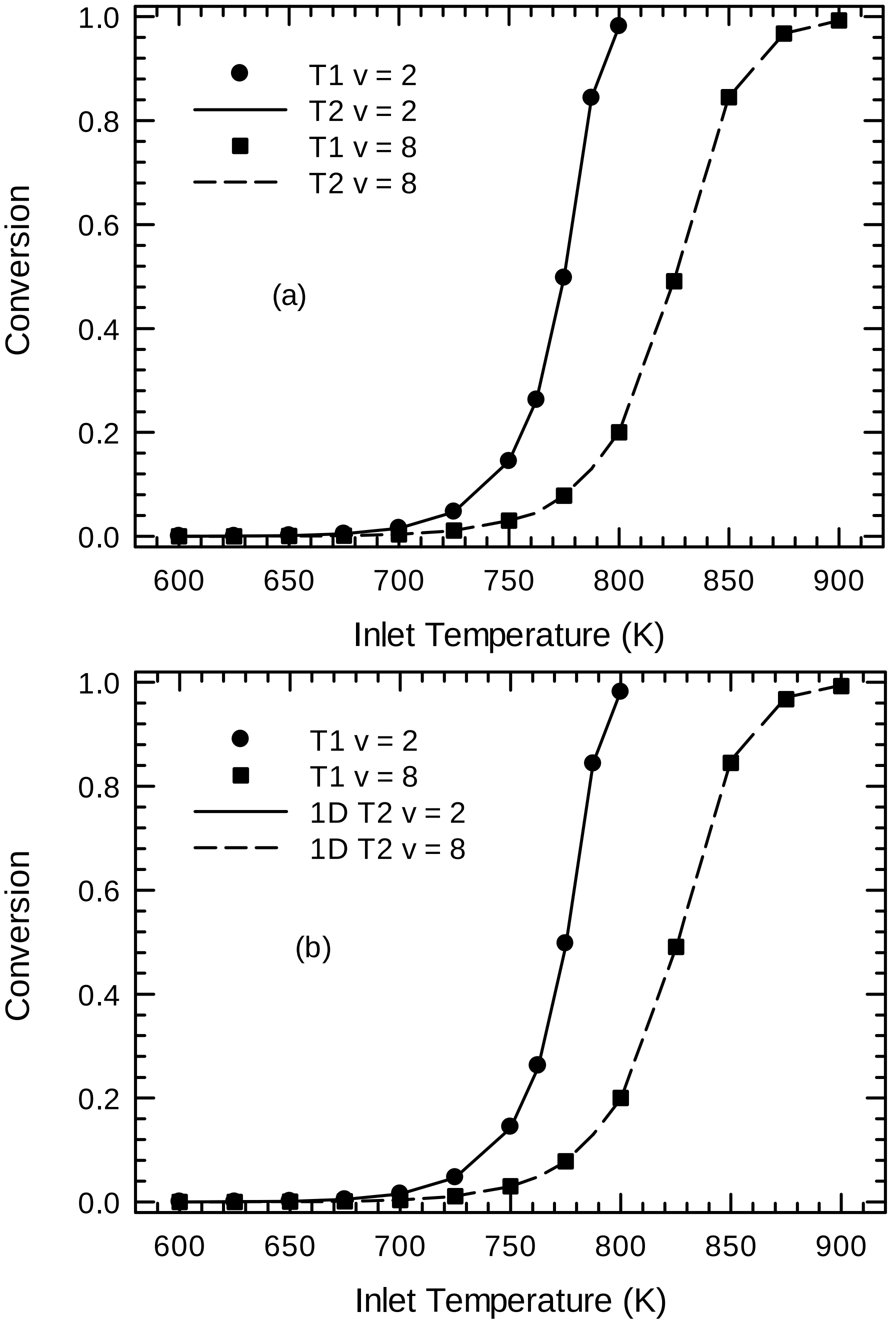

Figure 2.7 - The light-off curves generated by using lookup table T1 and T2 with different inlet velocity and hence different effectiveness factors. (a) 2D-axisymmetric model for the fluid and (b) 1D model for the fluid with Sh=Nu=4.36.

2.6 Coupling the look-up table (T2) to a 1D channel model

It is common in catalytic converter modelling to use a one dimensional SCM. When a whole converter is modelled (discussed later) using a continuum model, the fluid phase mass and energy balances are mathematically equivalent to using a 1D SCM. As an additional test, we compared the result from a one dimensional SCM coupled to the T2 look-up table. The 1D mass and energy balance equations expressed in terms of the surface fluxes are given in the following. The fluid phase mass balance is:

$$\frac{d}{dz}\left(D_I \rho \frac{dw_i}{dz}\right) - \rho v_z \frac{dw_i}{dz} - k_m \frac{4}{D}\rho\left(w_{i,f} - w_{i,S}\right) = 0 \tag{2.10}$$

The molecular diffusion coefficient in a 1D laminar flow is replaced by a dispersion coefficient, which can be approximated using the Taylor-Aris model (Hayes and Kolaczkowski, 1997).

$$D_I = D_i + \frac{v_z^2 D_H{}^2}{192 D_i} \tag{2.11}$$

At the solid surface, the flux at the washcoat surface balances the mass transfer to the fluid, thus the solid phase mass balance is:

$$k_m \rho\left(w_{i,f} - w_{i,S}\right) = \left(N_i\right)_2 \tag{2.12}$$

The 1D fluid phase energy balance is:

$$\frac{d}{dz}\left(k_f \frac{dT}{dz}\right) - \rho C_P v_z \frac{dT}{dz} - h\frac{4}{D}\left(T_f - T_S\right) = 0 \tag{2.13}$$

The solid phase energy balance, which includes axial conduction in the solid, is:

$$\frac{A_C}{P}\frac{d}{dz}\left(k_S \frac{dT}{dz}\right) - h\left(T_f - T_S\right) + (-\Delta H_R)\left(N_{\mathrm{CH_4}}\right)_2 = 0 \tag{2.14}$$

In this case the fluid and solid phases were coupled using a Sherwood number of 4.36, with results shown in Figure 2.7(b). The conversions are very close to those predicted from the 2D fluid phase models. For the simulations shown here, the axial conduction term was not significant.

2.7 Look-up tables for the non-uniform washcoat

We have discussed the more realistic scenario of the non-uniform washcoat, and this situation was considered in the preliminary work of Votsmeier (2009). Because it has been shown that the approximation of the fillet shape by a uniform washcoat can give rise to errors, we now explore methods for building a look-up table that incorporates diffusion in the washcoat for a fillet shape. This step requires some approximation. For example, it has been shown (Hayes et al., 2004, 2005) that the surface concentrations and temperatures vary along the washcoat external surface, and the effectiveness factor should be considered to be local. However, for simplicity and to facilitate the construction of the next look-up table, which we refer to as T3, we assume that the surface concentration and temperature are constant. To compute the average rate, we solve an isothermal 2D diffusion reaction problem over the domain of the fillet:

$$D_{\mathrm{eff}}\, \rho \cdot \left(\frac{\partial^2 w_i}{\partial x^2} + \frac{\partial^2 w_i}{\partial y^2} \right) + S_i \;=\; 0 \tag{2.15}$$

The solution for the concentration distribution in the fillet was once again performed using COMSOL, and the average reaction rate computed by the integration of the total flux along the boundary divided by the cross-sectional area of washcoat. As was done with T2, we store the average flux along the surface, rather than the average rate. The solution domain was discretized using a non-uniform unstructured mesh of 2016 triangular elements, with a higher element density near the surface, as shown in Figure 2.8. Figure 2.8 also shows a typical concentration profile for methane in the washcoat fillet. The presence of concentration gradients is evident. The look-up table giving the average reaction rate in the fillet (expressed as surface flux), called T3, was built using the same procedure used to build T1 and T2. It is advantageous to use T1 in the construction of T3, rather than Cantera, because of the large number of computations of the reaction source terms. It was verified that both methods (T1 and Cantera) gave the same result. We are effectively ignoring axial conduction in the solid, which makes the comparison a bit simpler. To include axial conduction requires a full 3D solution, which adds significantly to the execution time. The primary purpose here, however, is to compare the results obtained for the non-uniform look-up table. The use of this table in ECM simulations, including axial conduction, is shown later.

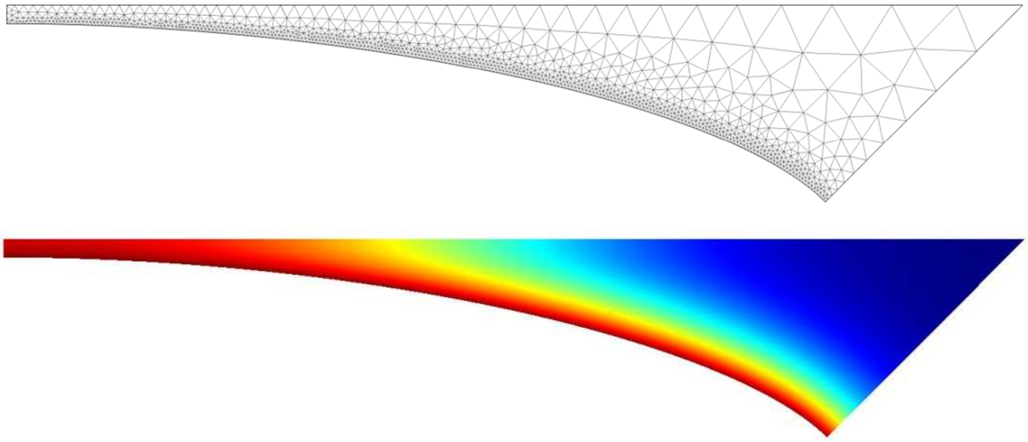

Figure 2.8 - Finite element mesh used to compute effectiveness factors in the non-uniform washcoat fillet. The mesh contains 2016 elements. The bottom picture shows a contour plot of a typical concentration profile, clearly showing the presence of concentration gradients.

2.8 Testing the table for the fillet shape in a 3D model

The first testing of the table T3 was done using what is called the pseudo-3D model (Hayes, et al., 2004; Votsmeier, 2009). In this model, the axial dispersion terms are all ignored, and the solution is obtained by marching a 2D slice of the monolith along the axis. From symmetry considerations, we can take the solution domain to be one eighth of the channel cross section. The solution domain and the finite element mesh, comprised of about 4000 elements, are shown in Figure 2.9. The washcoat thickness ranges from 10 to 150 microns.

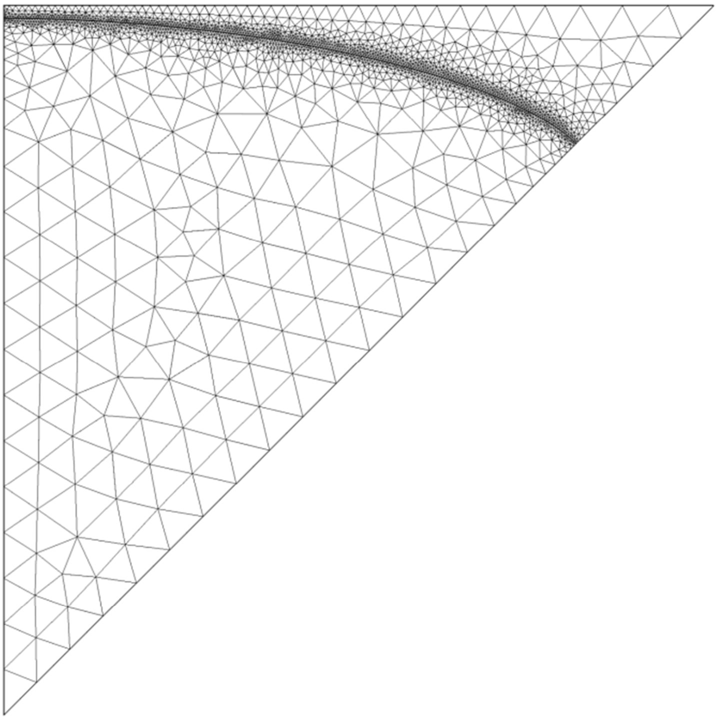

Figure 2.9 - Mesh used for the pseudo 3D geometry. There are 2002 elements in the washcoat region and 1753 elements in the gas phase.

Following Hayes et al. (2004), the velocity distribution is obtained by solving a diffusion like problem in the two dimensional domain corresponding to a channel slice. Thus solve:

$$\left(\frac{\partial^2 v_z}{\partial x^2}+\frac{\partial^2 v_z}{\partial y^2}\right)+S_v = 0 \tag{2.16}$$

The magnitude of the source term is selected to give the desired average velocity in the channel. The local velocity in the 3D simulation can then be adjusted to reflect the temperature at that point, assuming ideal gases. The mass balance equation for the channel is written:

$$v_z \frac{\partial w_i}{\partial z} = \frac{\partial}{\partial x}\left(D_i \frac{\partial w_i}{\partial x}\right) + \frac{\partial}{\partial y}\left(D_i \frac{\partial w_i}{\partial y}\right) \tag{2.17}$$

For the washcoat the mass balance is:

$$\frac{\partial}{\partial x}\left(D_{\text{eff}}\, \rho \frac{\partial w_i}{\partial x}\right) + \frac{\partial}{\partial y}\left(D_{\text{eff}}\, \rho \frac{\partial w_i}{\partial y}\right) + S_i = 0 \tag{2.18}$$

The energy balances for the fluid is:

$$(\rho\, C_P)_f\, v_z \frac{\partial T}{\partial z} = \frac{\partial}{\partial x}\left(k_f \frac{\partial T}{\partial x}\right) + \frac{\partial}{\partial y}\left(k_f \frac{\partial T}{\partial y}\right) \tag{2.19}$$

and for the washcoat it is:

$$\frac{\partial}{\partial x}\left(k_{\text{eff}} \frac{\partial T}{\partial x}\right) + \frac{\partial}{\partial y}\left(k_{\text{eff}} \frac{\partial T}{\partial y}\right) + (\Delta H_R)\, S_{\text{CH}_4} = 0 \tag{2.20}$$

The lookup tables were built and the simulations repeated for several values of the effective diffusion coefficient. We present the results from two sets. The first set used the standard value, whilst the second set used a value an order of magnitude lower. At 900 K the effectiveness factors corresponding to these effective diffusivities were about 0.62 and 0.35 respectively. The look-up table is used in conjunction with the channel mass and energy balances, where the average flux at the wall obtained from the look-up table is used as a boundary condition, in the same manner as with the 2D model. Figure 2.10 shows the ignition curves obtained for the different models using the standard value of the effective diffusion coefficient. To ensure clarity, we note again that the solid line represents the full 3D model solution, including diffusion and reaction in the washcoat, with the source terms computed from look-up table T1. The circular symbols represent the solution for the channel only, with the surface fluxes obtained from look-up table T3. Table 2.5 shows a comparison of execution times, as well as the outlet fraction conversion obtained for an inlet temperature of 900 K for both values of the effective diffusion coefficient. We see that the outlet conversion is essentially the same for the two cases, and that the use of the look-up table T3 gives of the order of a one thousand fold increase in execution speed compared to the use of Cantera. Clearly, there is a large time saving as a result of using the lookup tables in this manner.

Table 2.5 - Elapsed time and speedup factor of the lookup tables for different models

900K $\eta \cong 0.62$	Cantera	p3D-T1	p3D-T3	1D-T3	2D-uniform washcoat T1	2D-fillet washcoat T3
Conversion	71.65%	71.65%	71.52%	72.53%	77.57%	71.34%
Error	0	-0.002%	-0.180%	1.228%	8.260%	-0.435%
Time (s)	29684	169.63	28.24	0.7	144.02	38.54
speed up	1	175	1051	42405	206	770
900K (D_k/10) $\eta \cong 0.35$						
Conversion (%)	50.11%	50.11%	49.80%	50.74%	57.74%	49.49%
error	0	0.001%	-0.608%	1.257%	15.227%	-1.233%
Time (s)	30795	167.48	22.47	0.9	142.03	34.45
speed up	1	184	1370	34216	217	894

2.9 Testing the table for the fillet shape in a 2D model

The preceding result, although very impressive, still requires the use of a 3D model for the channel. We observe that in the simulations presented here, we have avoided a certain level of complexity by considering only steady state simulations, which allows the use of a pseudo-3D approximation. However, transient analysis requires a full 3D spatial model, which would still be time consuming, even though the use of Table T3 would reduce the execution time significantly. The next step therefore, was to compare the 3D results with a 2D approximation of the channel, which allows axi-symmetry to be used. We test and compare two cases. In the first case, we solve the problem using an axi-symmetrical 2D geometry with the washcoat configured as an annulus with the same cross sectional area as the fillet washcoat. This transformation is the classical one used for this level of model reduction (Hayes and Kolaczkowski, 1997), and the same as used in the previous sections of this paper. A new T2 look-up table was built for a washcoat of equivalent thickness as the non-uniform fillet. It was seen in this case that the conversion is appreciably different from the case with the fillet (see Table 2.5), especially in the intermediate conversion regions. The ignition curve for this case is represented by the square symbols in Figure 2.10 (where it is denoted modified T2). This result is consistent with that reported by More et al. (2006), who showed that light-off curves could be affected by the shape of the washcoat, everything else being equal. The next test was then to approximate the monolith channel using the same cylindrical geometry, but now, the look-up table T3 was used to compute the average rate. In effect, we reconfigure the channel, but use the effectiveness factors for the real washcoat geometry rather than that for the uniform washcoat. In this case we see from Table 2.5 that the outlet conversion is close to the value for the real channel. These results are represented by the triangular symbols in Figure 2.10. This result implies that we can use the much cheaper 2D solution for the channel, provided that the real washcoat effectiveness factor is used. Another conclusion is that the washcoat shape, and hence the internal diffusion effects, are more important than the channel shape for this geometry.

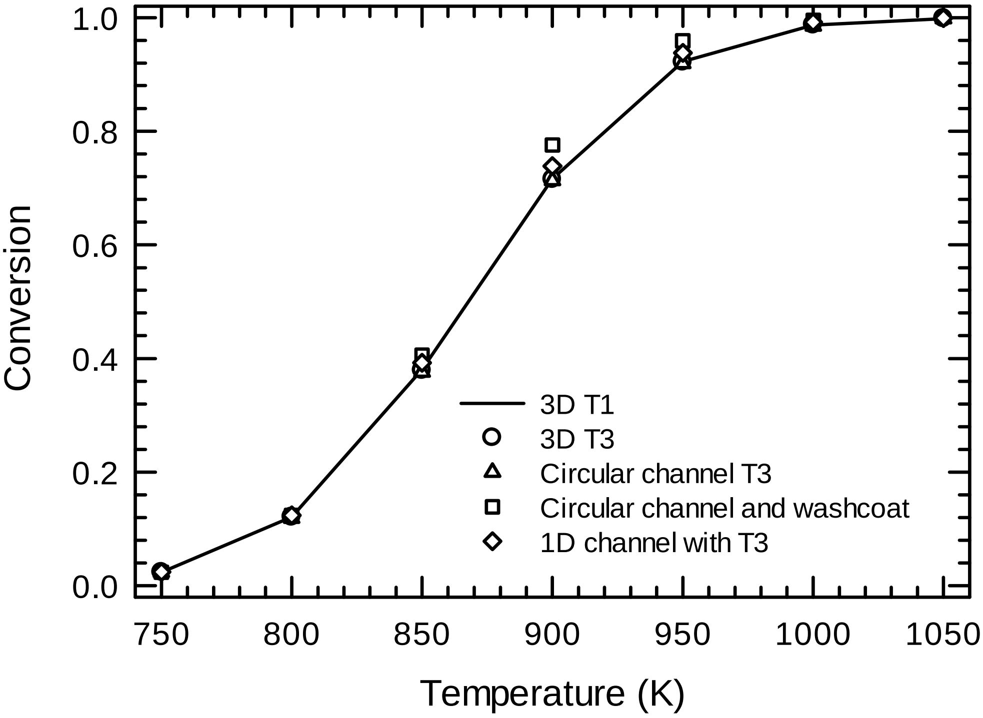

Figure 2.10 - Comparison of the accuracy of the 3D model using the T3 lookup table. The results are compared to the real solution of the washcoat, a 2D representation of the channel coupled to table T3, a 2D channel with an annular washcoat, and a 1D channel coupled to the T3 lookup table.

2.10 Testing the table for the fillet shape in a 1D model

The next approximation tested was to couple a 1D channel model to the look-up table T3, in the same manner as was done with T2 previously. The mass and energy balances for the fluid are given by Equations (2.10) and (2.13), whilst the solid phase mass and energy balances are:

$$k_m \rho\left(w_{i,f} - w_{i,S}\right) = \left(N_i\right)_3 \tag{2.21}$$

$$h\left(T_f - T_S\right) = \left(-\Delta H_R\right)\left(N_{\mathrm{CH}_4}\right)_3 \tag{2.22}$$

The fluid and solid phases were coupled using a Sherwood number of 4. To preserve consistency with the pseudo 3D model, axial conduction of energy was not included. The conversions predicted by this model are again slightly higher than for the real case, however, they are close enough for most modelling work. The result could again be improved by tuning slightly the Sherwood number. Certainly the speed-up for this final model justifies the approximations used. The results from these simulations are represented by the diamond shaped symbols in Figure 2.10.

2.11 Third level model reduction: Incorporating external diffusion resistance

The next level for model simplification is to include all of the diffusion resistances in the pre-computed look-up table, thus both the internal and external heat and mass transfer resistances are incorporated. We emphasize that this look-up table would be used exclusively with the 1D model, including models for the complete converter. The resulting 1D SCM is a simple pseudo-homogeneous type model, which will execute very fast, but at the same time allow the correct inclusion of all heat and mass transfer resistances. This look-up table is called T4.

We can envisage two options for the construction of the table T4. What is required to build the table is the ability to calculate the average reaction rate for a given value of the mixing cup temperature and concentration. In principle, these rates can be obtained by solving the single channel model (in either 2D or 3D) with the appropriate T2 or T3 look-up table for the internal diffusion. However, this method is somewhat time-consuming, because it is necessary to adjust the inlet concentrations in such a manner to achieve the required mixing cup values. A more rapid alternative makes use of the mass and heat transfer coefficients to compute the average rates at specified mixing cup values. That is, solve for each species, *i*, the mass balance equation:

$$k_m\, a_m\, \rho\left(w_{i,f} - w_{i,S}\right) = \left(-\bar{R}_i\right) \tag{2.23}$$

For the bulk temperature the equation is:

$$h\,a_m\left(T_f - T_S\right) = \left(\Delta H_R\right)\left(-\bar{R}_i\right) \tag{2.24}$$

The average reaction rate in the washcoat can be obtained from lookup table T2 or T3, depending on the washcoat that is to be used. Because the look-up tables are used to calculate surface flux, we solve iteratively the following two equations:

$$k_m\,\rho\left(w_{i,f} - w_{i,S}\right) = N_i \tag{2.25}$$

$$h\left(T_f - T_S\right) = \left(\Delta H_R\right) N_{\mathrm{CH_4}} \tag{2.26}$$

This method has the added advantage in that no COMSOL solutions are required, and the system of non-linear equations can be handled solely through the use of an appropriate MATLAB script (or indeed, Fortran or other computer language, according to user preference). It should be pointed out, however, that the energy balance implied by Equation (2.26) is only strictly valid for the steady state adiabatic case. Indeed, for the transient case (considered in the section on modelling of full scale converters), it is not possible to compute a general look-up table T4. For this work, the look-up table is built using table T2 if the washcoat is uniform in thickness (to give Table T4a), and Table T3 (to give Table T4b) if the fillet shape exists. It was shown that the 1D SCM coupled to table T3 gave a good approximation to the full 3D model, thus we expect a good result in this step.

The resulting T4 look-up tables are incorporated directly into the mass and energy balance equations as source terms. The 1D mass balance is:

$$\frac{d}{dz}\left(D_i\,\rho\frac{dw_i}{dz}\right) - \rho v_z\frac{dw_i}{dz} - a_m\left(N_i\right)_4 = 0 \tag{2.27}$$

Again, $\left(N_i\right)_4$ represents the surface flux and a_m is the surface area per unit of channel volume, thus making the units consistent. The energy balance is:

$$\frac{d}{dz}\left(k_f\frac{dT}{dz}\right) - \left(\rho C_P\right)_f v_z\frac{dT}{dz} + \left(-\Delta H_R\right)\left(N_{\mathrm{CH_4}}\right)_4 a_m = 0 \tag{2.28}$$

We should point out that, although all mass and heat transfer resistances are implicitly included, the solution does not give any information about the solid concentration and temperature.

In the first instance we compare the results from the 1D model with T4a with the results for the 2D axisymmetric model (see Figures 2.6 and 2.7). Figure 2.11 shows the ignition curves for the result (compare to Figure 2.7). It is seen that the difference in predicted conversion for the 1D model with T4a is very close to the full model values, showing that the approximation is good. Figure 2.12 shows the conversion as a function of axial position for three inlet temperatures, with the same values shown as obtained with Table T1. Compared to Figure 2.6, it is seen that the agreement is good.

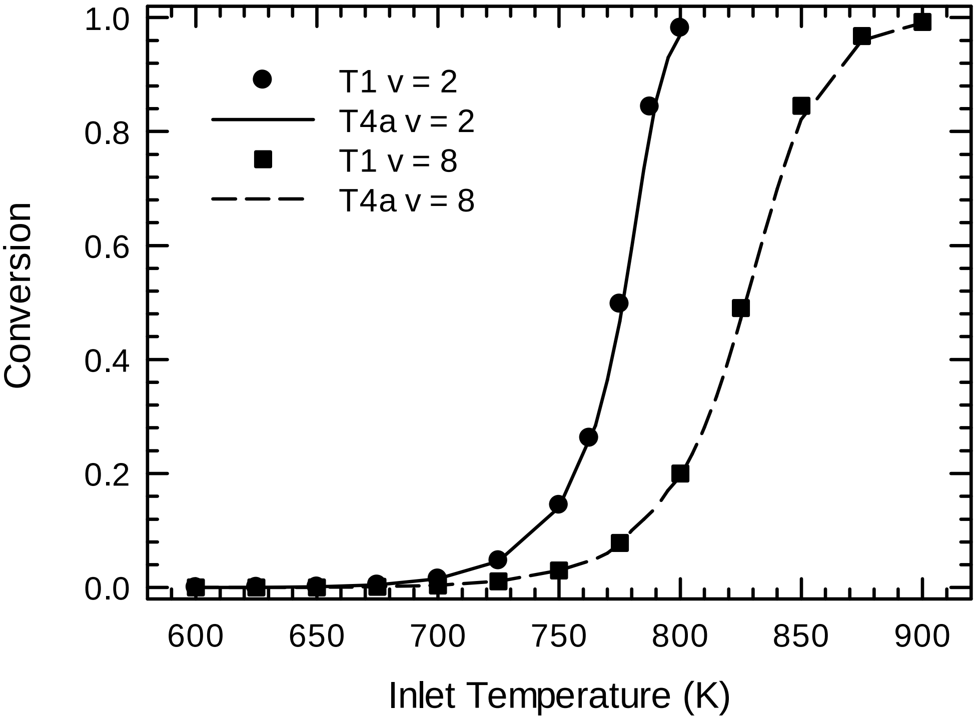

Figure 2.11 - The light-off curves generated by using lookup table T1 and T4a with different inlet velocity and hence different effectiveness factors.

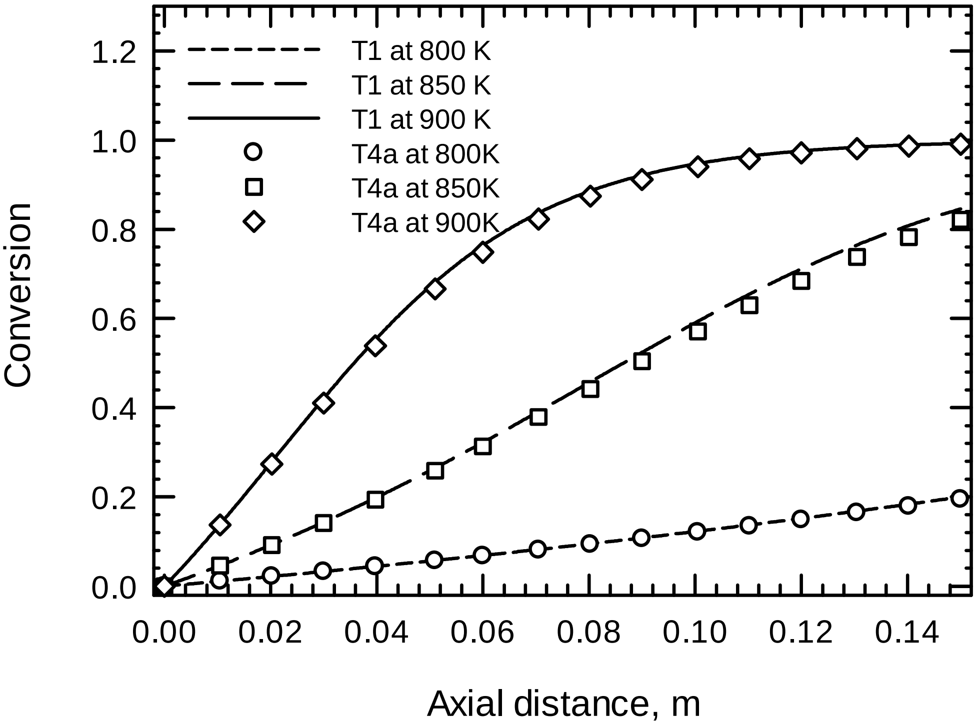

Figure 2.12 - Axial conversion profiles obtained with lookup tables T1 and T4a at three reactor inlet temperatures.

The same procedure applied to the fillet shaped washcoat, that is, Table T4b gave the results shown in Figure 2.13. The results obtained from the 1D T4b model are compared here with the real solution, as generated by the 3D model with lookup table T3. Again, it is seen that the agreement is acceptable. It is not meaningful to compare the execution time for this model. It took about the same amount of time as the simulations for the 1D models using T3. However, this time really reflects the time required to load the look-up table, and access it during execution. A more meaningful comparison will come with the implementation of the look-up tables in the full scale converter models, which is the subject of the final sections of this chapter.

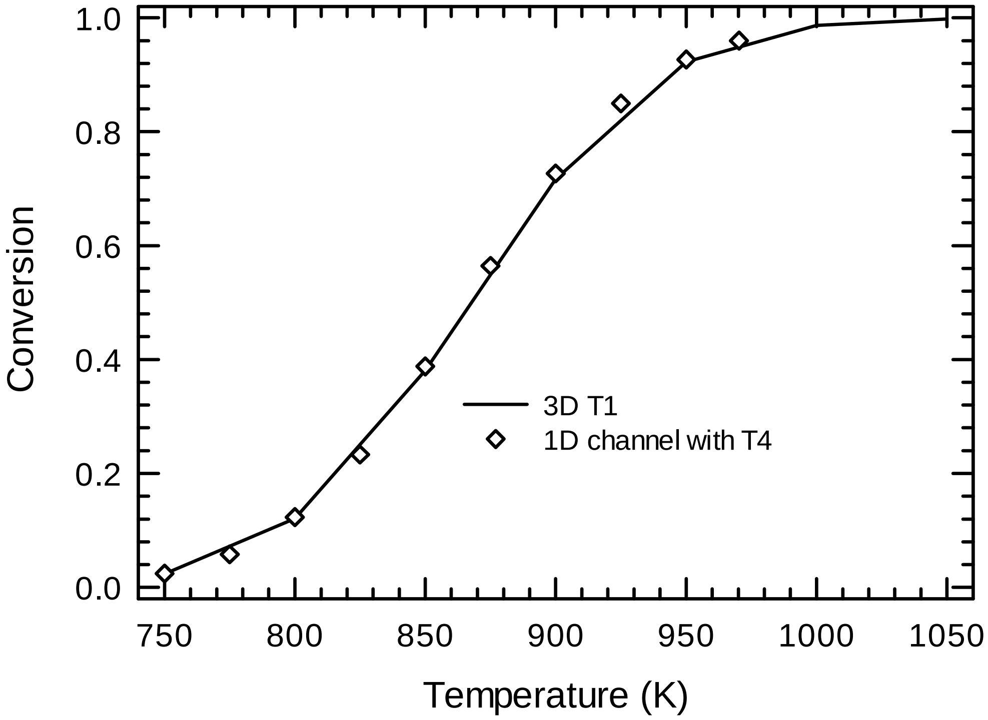

Figure 2.13 - Comparison of the accuracy of the 1D model using the T4b lookup table for the fillet shaped washcoat. The results are compared to the real solution of the washcoat, as given by the 3D model and the T1 lookup table.

2.12 Inclusion of look-up tables in full scale converter models

Having demonstrated the efficacy of the look-up table in the context of the single channel model, we now turn to its use in a full scale converter model. CFD modelling of catalytic converters has been the subject of many papers over the last decade or so, with various studies being reported. For a recent perspective, and a summary of the typical model equations required, see Hayes et al. (2012) or Liu et al. (2007). A brief description is given here. There are two types of solution domain in a converter system. The first is comprised of the open sections of the converter that correspond to the inlet and outlet pipes, and the two diffuser sections. The second domain is the monolith, which is treated as a porous medium using the continuum model.

The turbulent flow in the open sections can be modelled using the Reynolds averaged Navier-Stokes (RANS) momentum balance and continuity equations. The equations are given in Chapter 4, and are not repeated here.

The momentum balance in a porous medium can be developed using a volume average approach, where extra terms are introduced to account for the presence of the solid. The total mass conservation equation (continuity equation) remains the same:

$$\frac{\partial \rho_f}{\partial t} + \nabla \cdot \left(\rho_f v_S \right) = 0 \tag{2.29}$$

The velocity is the superficial velocity, defined as the channel velocity multiplied by the porosity. The momentum conservation equation is:

$$\frac{\partial}{\partial t}\left(\rho_f v_S \right) + \nabla \cdot \left(\rho_f v_S v_S \right) = -\nabla p + \nabla \cdot \tau - \left(\frac{\mu}{\mathbf{K}} v_S \right) \tag{2.30}$$

where $\mathbf{K}$ is the permeability tensor. For the monolith the flow is permitted along the channel direction only. We impose the Darcy permeability in the flow direction and a low permeability in the transverse directions. It is sufficient to impose a permeability value in these directions two orders of magnitude lower than in the flow direction for a monolith to ensure flow along the channels (Liu et al. 2007; Hayes et al., 2012).

The next paragraphs show the formulation of the mass and energy balance equations for the pseudo-homogeneous and the heterogeneous models in the context of the look-up table. We will present four variations on the equations, each of which uses a different look-up table.

In this work we have adopted the pseudo-steady state assumption for the gas phase (Hayes et al., 1992). In this approach, the fluid energy balance and the mass balance equations are steady state (the exception is the homogeneous model, which does not have a separate energy balance for the solid). The method has been long used, and an early discussion of the assumption and the relative time scales is given by T’ien (1981). We should point out, however, that the assumption is not always valid (see, for example, Sinha et al., 1985 or Karagiannidis and Mantzaras, 2010), and in such cases the full transient equations might be needed. The use of the lookup table should not be affected in such cases, however.

The first of our four models is the pseudo-homogeneous model. It should be emphasized here that the pseudo-homogeneous model, although conceptually the simplest, is rarely used in the literature. Although it traditionally requires the least amount of execution time, it has been shown that it may not be reliable, especially for transient simulations (see for example, Liu et al., 2007). However, it is worthwhile to include this model, both for completeness and comparison purposes. The species mass balance is:

$$\phi\nabla\left(D_I\,\rho\nabla w_i\right) - \rho v_s \nabla w_i + S_i = 0 \tag{2.31}$$

Although a 2D equation, it collapses to a *de facto* 1D problem, because the transverse to flow terms for diffusion and bulk flow disappear. The diffusion coefficient is set equal to zero in the orthogonal to flow direction. In the flow direction, the diffusion coefficient with laminar flow can be approximated using the Taylor-Aris model (Hayes and Kolaczkowski, 1997), as discussed earlier. The superficial velocity only has a value in the axial (flow) direction, and is zero in the transverse direction. The flow is restricted to unidirectional flow by making the transverse permeability very small (usually about two orders of magnitude lower than the flow direction). The source term accounts for all of the reactions, which for the case presented here is represented by the combustion of methane only. The units of the source term in this equation are kg/m^{3}s, where the volume is the total volume of the monolith, and therefore the values from the look-up table must be modified accordingly. For this model, the source term is obtained from the T4 level look-up table. If expressed as a flux, the mass balance is then written:

$$\phi\nabla\left(D_I\,\rho\nabla w_i\right) - \rho v_s \nabla w_i - a_m\left(N_i\right)_4 = 0 \tag{2.32}$$

The transient energy balance for the homogeneous model can be expressed as:

$$\nabla\left(k_{\text{eff}}\nabla T\right)-\rho C_P v_s \nabla T+\left(-\Delta H_R\right)\left(N_{\text{CH}_4}\right)_4 a_m=\left[(1-\varepsilon)\left(\rho C_P\right)_S+\varepsilon\left(\rho C_P\right)_f\right]\frac{dT}{dt} \tag{2.33}$$

The area term is the surface area (fluid/washcoat interfacial area) per unit monolith volume, therefore the units are consistent and the source term will have the correct basis. The contribution of the fluid to the transient term is minor and can be ignored. The calculation of effective thermal conductivities in monolith structures is addressed in Hayes et al. (2009). Note that the axial and transverse values are different, and depend on the physical and geometrical properties of the monolith. Also, note that the velocity in these conservation equations is the superficial velocity.

As noted in beginning of the section, the classical homogeneous model ignores heat and mass transfer limitations, because reaction rates are calculated at the fluid temperature and concentration. However, as we have seen, the look-up table T4 can be used with the homogeneous model, which provides source terms evaluated at the fluid phase values that nevertheless incorporate all heat and mass transfer effects, even for the non-uniform washcoat.

It is necessary to emphasize that the look-up table T4 is constructed as described earlier, using an assumed value of Nusselt and Sherwood number, and solving the coupled transport equations between fluid and solid (Equations(2.25) and (2.26)). We call this the non-isothermal look-up table T4, and for the purposes of this study it was built using look-up table T3. However, the energy balance represented by Equation (2.26) assumes that all thermal energy generated at the surface of the catalyst is transported to the fluid. This balance will not be true for transient simulations, or if significant temperature gradients occur in the monolith structure.

The remaining three models presented are variations of the heterogeneous model. The heterogeneous model requires a mass and energy balance for each phase. There are three options for these equations, depending on which look-up table is used. All variations yield information on both fluid and solid temperatures, however, if we want to retain information about the solid surface concentration, we must write the conservation equations using look-up table T3, giving two conservation equations for each phase. The fluid phase mass balance is:

$$\phi\nabla\left(D_I\,\rho\nabla w_i\right) - \rho v_s\nabla w_i - k_m\,a_m\,\rho\left(w_{i,f} - w_{i,S}\right) = 0 \tag{2.34}$$

At the solid surface, the flux from the washcoat balances the mass transfer to the fluid, thus the solid phase mass balance is:

$$k_m\,\rho\left(w_{i,f} - w_{i,S}\right) = \left(N_i\right)_3 \tag{2.35}$$

The energy balance for the fluid using the steady state assumption can be expressed as:

$$\nabla\left(k_{\text{eff}}\nabla T_f\right) - \left(\rho C_P\right)_f v_s\nabla T_f - h\,a_m\left(T_f - T_S\right) = 0 \tag{2.36}$$

The solid phase energy balance is:

$$\nabla\left(k_{\text{eff}}\nabla T_S\right) - h\,a_m\left(T_f - T_S\right) + a_m\left(-\Delta H_R\right)\left(N_{\text{CH}_4}\right)_3 = \left(\rho C_P\right)_S\frac{dT_S}{dt} \tag{2.37}$$

The effective thermal conductivities are selected according to direction and phase. We remind the reader that the look-up table T3 is evaluated at the solid temperature and concentration.

Alternatively, it is possible to use the T4 look-up table in the heterogeneous model, and thereby eliminate the explicit equation for the solid phase mass balance. There are two possibilities here, and the T4 table will be slightly different in each case. In both cases, the fluid phase mole balance is the same as for the homogeneous model:

$$\phi\nabla\left(D_I\,\rho\nabla w_i\right) - \rho v_s\nabla w_i - a_m\left(N_i\right)_4 = 0 \tag{2.38}$$

The fluid phase energy balance is given by Equation (2.36). The solid phase energy balance equation uses look-up table T4 for the flux, thus:

$$\nabla\left(k_{\text{eff}}\nabla T\right) - h\,a_m\left(T_f - T_S\right) + a_m\left(-\Delta H_R\right)\left(N_{\text{CH}_4}\right)_4 = \left(\rho C_P\right)_S \frac{dT}{dt} \tag{2.39}$$

As noted earlier with the homogeneous table, some care must be taken using table T4. In the first instance we generate what we call the non-isothermal T4 table, which is generated from T3 using Equations (2.25) and (2.26), as done for the single channel and the pseudo-homogeneous models. This table is evaluated using the fluid phase concentration and temperature. However, as noted earlier, the energy balance of Equation (2.26) is only valid for the steady state case without strong temperature gradients. Whilst we do not have another choice for the pseudo-homogeneous model, there is an alternative for the heterogeneous model. We can build a T4 table from T3 by solving the mass balance equation only (that is, Equation (2.25)) using an isothermal case (fluid and solid temperatures equal), which we call the isothermal T4. However, when this table is used for the converter solid energy balance (Equation (2.39)), the fluid phase concentration and the solid phase temperature are used.

In the following section, some steady state and transient simulations are tested and compared for these four models.

2.13 Results for the full scale converter models

We now consider some results from the four model types. All models will use the pseudo-steady state assumption for the gas phase, as discussed earlier. The models are (1) Pseudo-homogeneous model, with T4 table [Ho T4(ni)]; (2) heterogeneous model using T3 table [He T3]; (3) heterogeneous model using T4 non-isothermal table [He T4(ni)] and (4) heterogeneous model using T4 isothermal table [He T4(i)]. All of the tests were performed for one converter geometry with axisymmetry, see Figure 2.14. The monolith was 15 cm long (*L*) and 13.51 cm in diameter (*D*), which gives an *L/D* ratio of 1.11. An insulation layer 7 mm thick was placed between the monolith and the wall. The thermal conductivity of this layer was 0.2 W/(m·K). The monolith cell density was 400 CPSI with a 7 mil (0.178 mm) wall thickness. The washcoat fillet shape is the same as used earlier in this study. The inlet and outlet pipes are 5 cm in diameter (*DP*) and 2.5 cm long (*LP*). The diffuser angle is 60 degrees for both inlet and outlet. The inlet velocity profile to the pipe was uniform, with a value of 7.6 m/s at 300 K, to give a gas hourly space velocity (GHSV) of 25 000 h^{-1}, referenced at 300 K. The velocity was adjusted to account for a changing inlet temperature to give a constant mass flow rate. All tests used this GHSV with a feed consisting of 1000 ppm of methane with 6 % water and 6 % oxygen (all by volume) and the rest nitrogen. Table 6 shows some properties of the monolith used. Heat transfer to the external environment at 300 K occurred by convention, with a heat transfer coefficient of 15 W/(m^2·K).

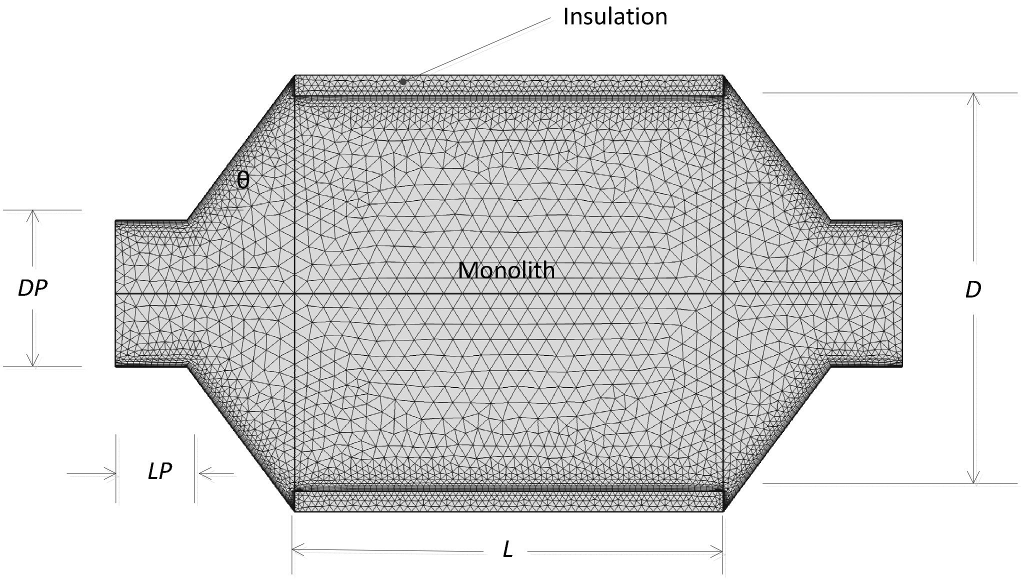

Figure 2.14 - Schematic showing the converter geometry used in the CFD tests on the full size converter.

Table 2.6 - The monolith properties used in the ECM simulations.

Porosity	0.620
Hydraulic diameter, D_H, mm	1.000
Geometric surface area, GSA m^2/m^3	2479
Bulk density monolith, kg/m^3	556.5
Axial permeability, m^2	1.94E-08
Axial thermal conductivity, solid, $W/(m \cdot K)$	0.611
Radial thermal conductivity, solid, $W/(m \cdot K)$	0.383
Monolith heat capacity (average) J/(kg K)	1100

The following tests were done: (1) Steady state simulations over the temperature range 600 to 900 K. This result represents an infinitely slow temperature ramp. (2) Transient simulation where the initial temperature is generated by a steady state solution for an inlet gas temperature of 700 K (which corresponds to an outlet temperature of about 677 K, owing to heat loss to the surroundings. Then, the inlet temperature was ramped from 700 K to 1000 K over a period of one second, using a smooth exponential function. This step represents an extremely fast temperature ramp.

Figure 2.15 shows the steady state ignition curves for the four models expressed in terms of fractional conversion of methane as a function of inlet temperature. It can be seen that the four models all predict a very similar ignition curve, which is an interesting result. Table 2.7 shows some selected points from the curves for the different models. The execution times are not very different, and interestingly, the pseudo-homogeneous model took the longest to run. For the steady state simulations at an inlet temperature of 900 K, the times are 229 s for the pseudo-homogeneous model, 199 seconds for the heterogeneous T3, 149 s for the heterogeneous T4(non-isothermal) and 157 s for the heterogeneous T4(isothermal).

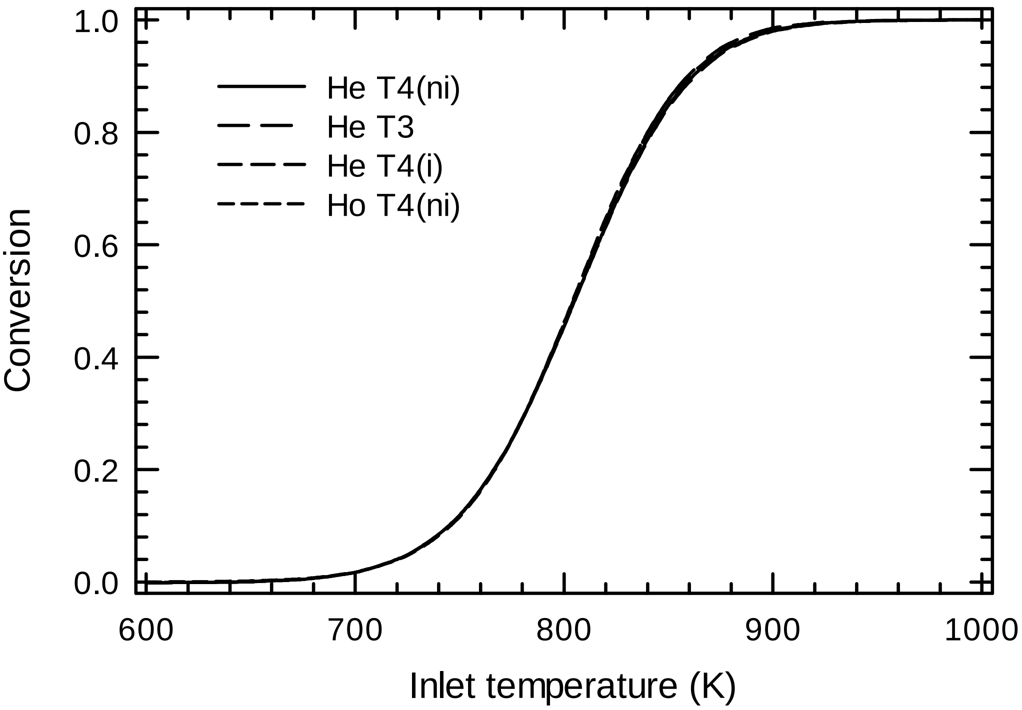

Figure 2.15 - Steady state ignition curves for the four models expressed in terms of fractional conversion of methane as a function of inlet temperature. See Table 2.7.

Table 2.7 - Selected points for the steady state ignition curve for the four ECM tested.

Temp., K	700	750	800	850	900
Homogeneous, T4 Ho T4(ni)	0.0172	0.1156	0.4617	0.8579	0.9816
Heterogeneous, T3 He T3	0.0170	0.1156	0.4617	0.8579	0.9816
Heterogeneous, T4, isothermal, He T4(i)	0.0170	0.1156	0.4617	0.8579	0.9816
Heterogeneous, T4, non-isothermal He T4(ni)	0.0170	0.1156	0.4617	0.8579	0.9816

Figure 2.16 shows the ignition curve for conversion as a function of time for the fast temperature ramp. It is interesting to note that the results are very similar

for all of the models tested. The average outlet gas temperature as a function of time is shown in Figure 2.17. We observe that it takes much longer for thermal steady state to be reached, compared to the time to reach 100 % conversion. The reason is that the front of the monolith achieves a high temperature before the back has started to warm, and most of the methane reacts in the first few cm of length. The temperature responses are similar, with some discrepancy at higher inlet temperatures. Figure 2.18 shows two perspective views of the converter, each being a snapshot of the temperature profile during the transient run for the slow temperature ramp. The pictures correspond to outlet conversions of 25 % and 75 % respectively. The temperature distribution is clearly seen. The radial profile is the result of heat losses through the walls, as well as the uneven heating pattern introduced by the variable velocity profile across the radius of the monolith.

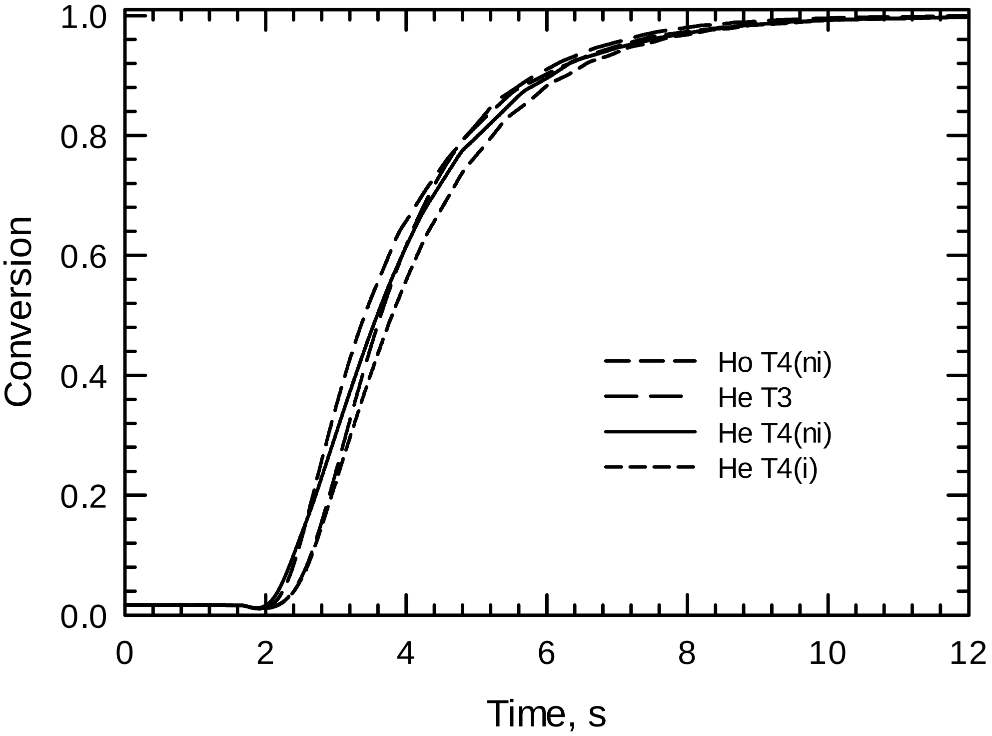

Figure 2.16 - Transient ignition curves for the four models expressed in terms of fractional conversion of methane as a function of time for a high speed temperature ramp.

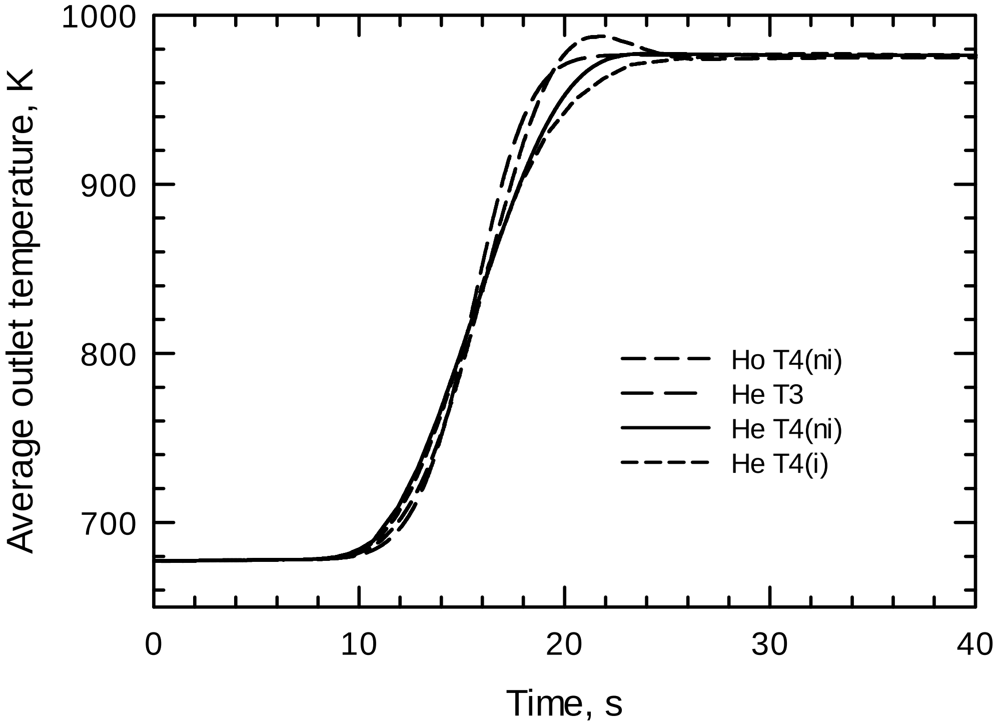

Figure 2.17 - Transient temperature response curves for the four models expressed in terms of average outlet gas temperature as a function of time for a high speed temperature ramp.

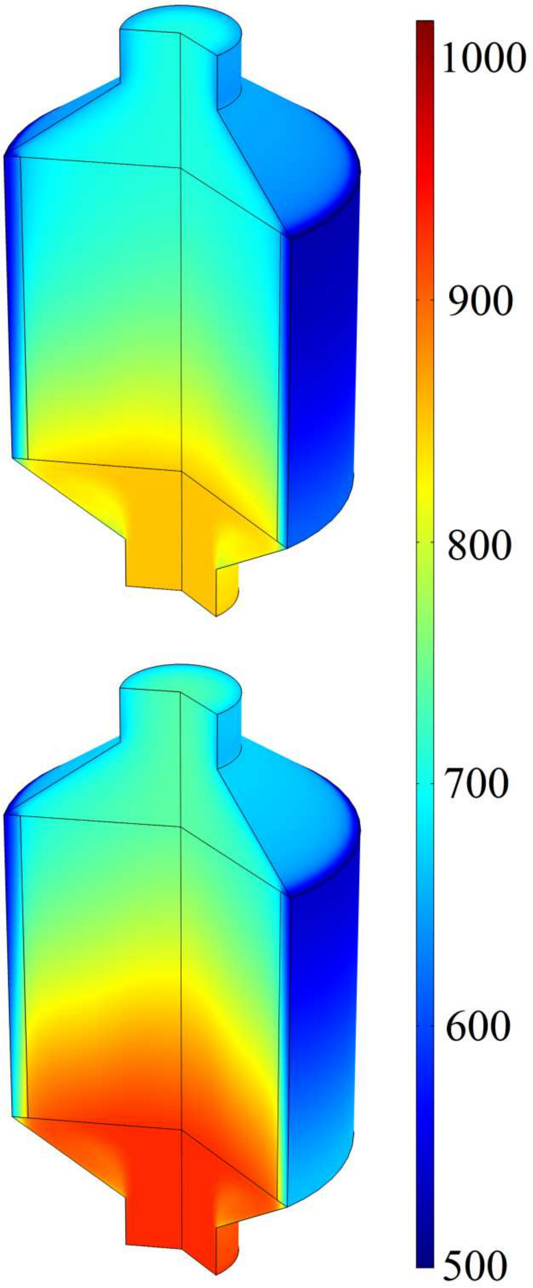

Figure 2-18 - Temperature profiles during the slow light-off run. The top picture corresponds to an outlet conversion of 25 %, whilst the bottom has an outlet conversion of 75 %.

There is some difference in execution times. For the first 25 seconds of reactor time, the CPU times are (1) pseudo-homogeneous T4, 705 s; (2) Heterogeneous T3, 65,559 s; (3) heterogeneous non-isothermal T4, 567 s; and (4) heterogeneous isothermal T4, 511 s. What is interesting is the very long time required for the heterogeneous T3 model, which is a result of having to solve the additional mass balance equation for the solid, which is very slow to converge to a solution. We point out that we did do some simulations with slower temperature ramps, and the there was less difference between the output curves. The difference in execution times between the heterogeneous T3 model and the others did decrease somewhat, but there was still a large difference.

2.14 Conclusions

In this work we have examined the use of pre-computed data stored in look-up tables to reduce the execution time required for the simulation of a monolith reactor. We have extended earlier work to show that the effects of both internal and external diffusion resistance can be easily incorporated into the pre-computed values, giving a much larger speed enhancement than that obtained by computing the rate alone. The effect of complex washcoat geometry can be easily incorporated in this way. Finally, the use of this type of look-up table allows for the modelling of full scale catalytic converters with the inclusion of the detailed washcoat diffusion effects in real fillet shapes at the micro level at a reasonable cost in terms of execution time. These improvements can readily be adapted to other reactor types, such as packed beds or other structured reactor types to give similar increases in execution speed.

Having demonstrated the effectiveness of the data reduction method, it is nonetheless pertinent to emphasize a number of points. The improvements of CPU time shown depend on the solvers used, the computing language, the mesh size, the underlying model assumptions, operating conditions, etc. Changes in any of these could all lead to very different execution times, which would in turn affect the speedup factors. We are not claiming to have achieved the best execution time in each case; however, the degree of speedup should be significant in all cases. Another point is that for the mechanistic model chosen, we have assumed a steady state at the catalyst surface (adsorbed species in equilibrium with the case phase). When this is not true, then the use of look-up tables would be more complicated.

NOMENCLATURE

A_C	cross sectional area of channel, $\mathrm{m^2}$
a_m	Surface area per unit volume, $\mathrm{m^2/m^3}$
C_P	Constant pressure heat capacity, $\mathrm{J/kg \cdot K}$
D	Diameter of monolith or channel, according to context, m
D_i	Molecular diffusion coefficient, $\mathrm{m^2/s}$
DP	Diameter of inlet pipe, m
D_H	Hydraulic diameter, m
h	Heat transfer coefficient, $\mathrm{W/m^2K}$
(ΔH_R)	Enthalpy change of reaction, $\mathrm{J/mol}$
k	Thermal conductivity, $\mathrm{W/m \cdot K}$
k_m	Mass transfer coefficient, m/s
K	Permeability, $\mathrm{m^2}$
L	Monolith length, m
LP	Length of inlet pipe, m
M	Molar mass of a substance, g/mol
$\left(N_i\right)$	flux at the washcoat channel interface, $\mathrm{kg/(m^2s)}$
p	Pressure, Pa
P	perimeter of channel, m
$\left(-R_i\right)$	reaction rate of species *i*, $\mathrm{kg/m^3s}$
$\left(-\bar{R}_i\right)$	average reaction rate of species *i*, $\mathrm{kg/m^3s}$
S_i	source term for species *i*, $\mathrm{kg/(m^3 \cdot s)}$
t	Time, s
T	Temperature, K
r	radial coordinate, m
v	Velocity, m/s
x	coordinate location, m

y	coordinate location, m
w	Mass fraction

Greek Symbols

ϕ	Monolith porosity (open frontal area)
ρ	Density, $\mathrm{kg/m^3}$
μ	Viscosity, $\mathrm{Pa \cdot s}$

Subscripts

eff	effective value
f	fluid
i	species
s	superficial
S	Solid, surface or superficial
z	Axial component

References

Bertrand, F., Devals, C., Vidal, D., Préval, C.S.D., Hayes, R.E. 2012. Towards the simulation of the catalytic monolith converter using discrete channel-scale models. Catalysis Today 188, 80–86.

De Boor, C. 1978. A practical guide to splines. Springer, New York.

Deutschmann, O., Schmidt, R., Behrendt, F., Warnat, J. 1996. Numerical modeling of catalytic ignition. Symposium (International) on Combustion 26, 1747–1754.

Goodwin, D.G., 2003. An open-source, extensible software suite for CVD process simulation. In: Chemical Vapor Deposition XVI and EUROCVD (eds. Allendorf, M., Maury, F. & Teyssandier, F.). Electrochemical Society, pp. 155–162.

Groppi, G., Belloli, A.,Tronconi, E., Forzatti, P., 1995. A comparison of lumped and distributed models of monolith catalytic combustors. Chemical Engineering Science 50, 2705–2715.

Groppi, G., Tronconi, E., 1996. Continuous vs. discrete models of nonadiabatic monolith catalysts. AIChE journal 42, 2382–2387.

Gupta, N., Balakotaiah, V., 2001. Heat and mass transfer coefficients in catalytic monoliths. Chemical Engineering Science 56, 4771–4786.

Hayes, R.E., Fadic, A., Mmbaga, J., Najafi, A., 2012. CFD modelling of the automotive catalytic converter. Catalysis Today 188, 94–105.

Hayes, R.E., Kolaczkowski, S.T., 1994. Mass and heat transfer effects in catalytic monolith reactors. Chemical Engineering Science 49, 3587–3599.

Hayes, R.E., Kolaczkowski, S.T. 1997. Introduction to Catalytic Combustion. Gordon and Breach, Reading, UK.

Hayes, R.E., Kolaczkowski, S.T., 1999. A study of Nusselt and Sherwood numbers in a monolith reactor. Catalysis Today 47, 295–303.

Hayes, R.E., Kolaczkowski, S.T., Thomas, W.J.,1992. Finite-element model for a catalytic monolith reactor. Computers & Chemical Engineering 16, 645–657.

Hayes, R.E., Kolaczkowski, S.T., Thomas, W.J., Titiloye, J., 1996. Transient experiments and modeling of the catalytic combustion of methane in a monolith reactor. Industrial & Engineering Chemistry Research 35, 406–414.

Hayes, R.E., Liu, B., Moxom, R., Votsmeier, M., 2004. The effect of washcoat geometry on mass transfer in monolith reactors. Chemical Engineering Science 59, 3169–3181.

Hayes, R.E., Mok, P.K., Mmbaga, J., Votsmeier, M.,2007. A fast approximation method for computing effectiveness factors with non-linear kinetics. Chemical Engineering Science 62, 2209–2215.

Hayes, R.E., Rojas, A., Mmbaga, J., 2009. The effective thermal conductivity of monolith honeycomb structures. Catalysis Today 147, S113–S119.

Hayes, R.E., Liu, B., Votsmeier, M., 2005. Calculating effectiveness factors in non-uniform washcoat shapes. Chemical engineering science 60, 2037–2050.

Karagiannidis, S., Mantzaras, J., 2010. Numerical investigation on the start-up of methane-fueled catalytic microreactors. Combustion and Flame 157, 1400-1413.

Kočí, P., Novák, V., Štěpánek, F., Marek, M. & Kubíček, M., 2010. Multi-scale modelling of reaction and transport in porous catalysts. Chemical Engineering Science 65, 412–419.

Kumar, A., Mazumder, S., 2010. Adaptation and application of the In Situ Adaptive Tabulation (ISAT) procedure to reacting flow calculations with complex surface chemistry. Computers & Chemical Engineering 35, 1317–1327.

Leung, D., Hayes, R., Kolaczkowski, S.T., 1996. Diffusion limitation effects in the washcoat of a catalytic monolith reactor. Canadian Journal of Chemical Engineering, 74, 94–103.

Liu, B., Hayes, R.E., Yi, Y., Mmbaga, J., Checkel, M.D., Zheng, M., 2007. Three dimensional modelling of methane ignition in a reverse flow catalytic converter. Computers & Chemical Engineering 31, 292–306.

Litto, R., Nien, T., Hayes, R.E., Mmbaga, J.P., Votsmeier, M., 2012. Parametric study of a recuperative catalytic converter. Catalysis Today 188, 106–112.

Meisel, W.S., Collins, D.C., 1973. Repro-modeling: An approach to efficient model utilization and interpretation. Systems, Man and Cybernetics, IEEE Transactions on 3, 349–358.

More, H., Hayes, R.E., Liu, B., Votsmeier, M., Checkel, M.D., 2006. The effect of catalytic washcoat geometry on light-off in monolith reactors. Topics in Catalysis 37, 155–159.

Mukadi, L.S., Hayes, R.E., 2002. Modelling the three-way catalytic converter with mechanistic kinetics using the Newton–Krylov method on a parallel computer. Computers & Chemical Engineering, 26, 439–455.

Pope, S.B., 1997. Computationally efficient implementation of combustion chemistry using in situ adaptive tabulation. Combustion Theory and Modelling 1 41-63.

Raja, L.L., Kee, R.J., Deutschmann, O., Warnatz, J., Schmidt, L.D., 2000. A critical evaluation of Navier–Stokes, boundary-layer, and plug-flow models of the flow and chemistry in a catalytic-combustion monolith. Catalysis Today 59, 47–60.

Salomons, S., Hayes, R.E., Votsmeier, M., Drochner, A., Vogel, H., Malmberg, S., Gieshoff, J., 2007. On the use of mechanistic CO oxidation models with a platinum monolith catalyst. Applied Catalysis B: Environmental 70, 305 - 313.

Santos, J.C., Cheng, Y., Dias, M.M., Rodrigues, A.E., 2010. Surface B-splines fitting for speeding up the simulation of adsorption processes with IAS model. Computers & Chemical Engineering 35, 1186–1191.

Scheuer, A., Hirsch, O., Hayes, R.E., Vogel, H., Votsmeier, M., 2011. Efficient simulation of an ammonia oxidation reactor using a solution mapping approach. Catalysis Today 175 141-146.

Scheuer, A., Drochner, A., Gieshoff, J., Vogel, H., Votsmeier, M., 2012. Runtime efficient simulation of monolith catalysts with a dual-layer washcoat. Catalysis Today 188 70-79.

Sinha, N., Bruno, C., Bracco, F.V., 1985. Two dimensional transient catalytic combustion of CO – air on platinum. Physicochem. Hydrodynamics, 6 373-391.

T'ien, J.S., 1981. Transient catalytic combustor model. Combustion Science and Technology 26 65-75.

Tischer, S., Correa, C., Deutschmann, O., 2001. Transient three-dimensional simulations of a catalytic combustion monolith using detailed models for heterogeneous and homogeneous reactions and transport phenomena. Catalysis Today 69, 57–62.

Turányi, T.,1994a. Application of repro-modeling for the reduction of combustion mechanisms. Symposium (International) on Combustion 25, 949–955.

Turányi, T.,1994b. Parameterization of reaction mechanisms using orthonormal polynomials. Computers & chemistry 18, 45–54.

Votsmeier, M., 2009. Efficient implementation of detailed surface chemistry into reactor models using mapped rate data. Chemical Engineering Science 64, 1384–1389.

Votsmeier, M., Scheuer, A., Drochner, A., Vogel, H., Gieshoff, J., 2010. Simulation of automotive NH3 oxidation catalysts based on pre-computed rate data from mechanistic surface kinetics. Catalysis Today 151, 271-277.

Chapter 3:

Applications of Multi-scale modelling to Catalytic Converters

Parametric Study of a Recuperative Catalytic Converter

Overview

This chapter describes a computational study of a proposed recuperative catalytic converter intended for the catalytic combustion of lean methane streams. The design is based on the principle of alternating layers of washcoated monolith channels through which the fluid passes in counter-current flow. Heat transfer occurs continuously across the boundary separating the layers, thus the exiting hot gas exchanges energy with the incoming cold gas. Monoliths composed of Cordierite and silicon carbide are compared, each of which had 12 % by volume washcoat applied. The effects of layer thickness, monolith length and space time are compared. It is found that the monolith comprised of higher thermal conductivity material is more effective in enhancing the temperature in the reactor. Conversion of methane entering the reactor at relatively low temperatures can be oxidised with some added thermal energy.

This chapter is a modified version of the paper --- R. Litto, T. Nien, R.E. Hayes, J.P. Mmbaga, M. Votsmeier, Parametric Study of a Recuperative Catalytic Converter, *Catalysis Today*, **188** 106-112 2012.

3.1 Introduction

The quest for lower levels of exhaust gas emissions from the automotive sector has resulted in the successful adoption of the catalytic converter for stoichiometric gasoline engines and for lean burn Diesel engines. In the former case the technology is well developed, whilst for the latter case the lean burn environment causes special problems for NO_X reduction. Diesel lean burn engines also have lower exhaust gas temperatures, making the oxidation reactions more difficult. Recent moves to use alternative fuels with a lower carbon footprint have led to increasing challenges. A key alternative fuel is compressed natural gas (CNG), which has the lowest CO_2 emissions per unit of produced energy of all of the hydrocarbons. CNG is usually used in a lean burn compression ignition (CI) engine. The key hydrocarbon in the exhaust is methane, and forthcoming legislation will require its control in such engines. Methane is the most stable hydrocarbon and the most difficult to activate, making its destruction in the catalytic converter problematic. Methane combustion requires a relatively high temperature compared to other hydrocarbons and to carbon monoxide. Furthermore, the effort on the part of the engine manufactures to produce lower in-cylinder combustion temperatures leads to low exhaust temperature, thus compounding the difficulty. The design of a catalytic converter for a natural gas engine thus remains a challenge. Maintaining a sufficiently high temperature for auto thermal operation is difficult with the relatively small amounts of methane in the exhaust. In the absence of a significantly more active catalyst than the ones currently known, it is therefore likely that some form of thermal management system needs to be adopted.

Typical thermal management systems, also known as heat integrated concepts, employ some form of combined reaction heat exchange, in which the thermal energy in the effluent gas is exchanged with the influent. In the literature, many designs of combined reactor heat exchanger have been proposed, and a summary of some of the options is provided in [1]. An interesting design, proposed in the early thirties and subsequently developed by many parties is the reverse flow reactor. This latter system was used in a system specifically intended for a natural gas vehicle [2]. The drawback of this system in an exhaust stream is that there are several moving parts. Other types of integrated reactor and heat exchanger concepts have been presented [3, 4]. We can, somewhat arbitrarily divide the concepts into two groups. In the first, the reactor and heat exchanger are not directly integrated, that is, the feed and effluent exchange heat in a separate heat exchanger. This design has an advantage in that one can independently control the heat transfer parameters such as the heat transfer area, and the construction may be easier. In the second group, the reaction and heat exchange occur in the same physical unit, that is, there is a continuous exchange of heat with the reactor. This type of system may offer the possibility of a smaller unit size, although the amount of heat transfer area available will now be a stronger function of the internal configuration, and one is constrained by the materials that must be used to construct the reactor. Thus careful consideration of the design is important. This work describes a computational study of a counter flow monolith reactor, in which alternating layers of monolith have opposite flow, and thus exchange heat. Each layer is of the order of ten to twenty channels in thickness. The objective is to determine if this type of design offers promise for a catalytic converter for a CNG engine.

Reducing exhaust emissions of natural gas internal combustion engines is critical and new technology is required. The technology that uses engine exhaust waste heat for auto-thermo reaction in recuperative manner has a potential for simultaneously reducing both exhaust waste heat rate and emissions.

3.2 Reactor concept

The fundamental concept of the proposed reactor/heat exchanger is to use the existing and successful monolith reactor design. To employ the counter-current flow with heat exchange, we have alternating layers of monolith cells with opposite flows. Heat transfer occurs in the transverse to flow direction by conduction, and is carried by convection in the flow direction. The three dimensional view of a section is shown in Figure 3.1 and the cross section view from the side that illustrates the flow patterns is shown in Figure 3.2.

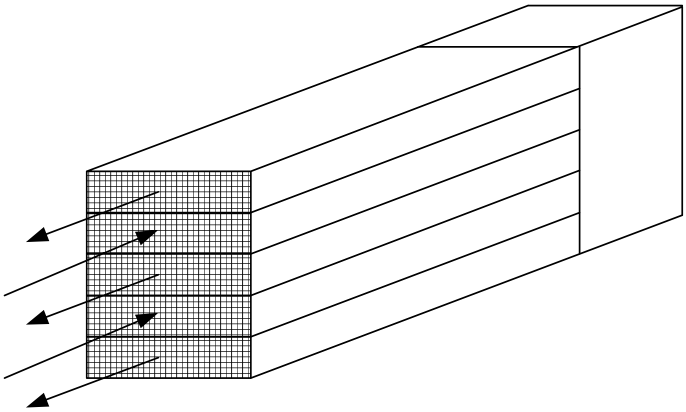

Figure 3.1 – Perspective view of a counter flow recuperator comprised of monolith section.

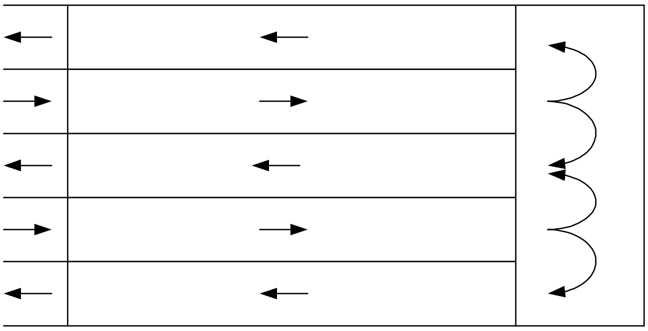

Figure 3.2 – Cross section of recuperator illustrating the flow patterns.

Fresh feed enters at a relatively low temperature from the front, travels along the monolith sections shown, exits the monolith and is mixed in the chamber at the end, and finally enters the alternate monolith layers to travel back to the front.

Heat transfer by conduction will occur across the monolith layers, so heat from reaction can pre-heat the feed. Some energy may be added in the mixing chamber at the end to ignite the reaction and to maintain auto-thermal operation if the inlet temperature or the methane concentration are low. The amount of such added energy is a critical design parameter of this concept.

To understand some of the performance issues with this design, a detailed parametric study can be performed using computer modelling. Although the reactor is three dimensional in nature, the performance can be analyzed with a good degree of accuracy using a two dimensional approximation. A representative reactor section can be represented by the half height of one forward and one reverse flow section. The resulting sub-domains are shown in Figure 3.3.

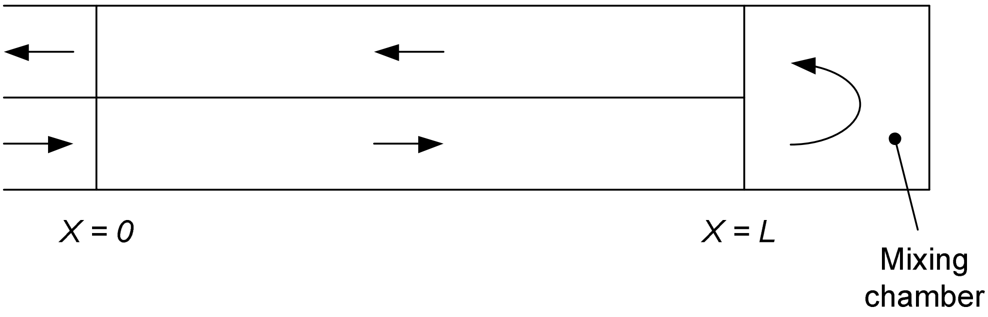

Figure 3.3 - Solution domain of the proposed recuperator monolith reactor.

The layout of the rest of the chapter is as follows. In Section 3.3 the model equations are developed for the case without and without chemical reaction. We then present, in Section 3.4, a detailed study of the recuperative performance of the unit. In the first instance, this study is performed without chemical reaction present, to allow us to focus on the heat transfer properties of the unit. Finally, the catalytic combustion of methane is studied using a detailed mechanistic reaction model that accounts for the non-uniform washcoat shape and the internal washcoat diffusion resistance.

3.3 Model Equations

The classical method to model the monolith sections is to treat them as a porous medium, thus using a continuum approach. Furthermore, it is generally considered necessary to use a heterogeneous model, in which separate mass and energy balance equations are written for the fluid and solid phases. The general background on the equations required for the heterogeneous modelling of a monolith reactor system are given in, for example, reference [5]. Because of the low Reynolds number in the monolith channels, Darcy's law is valid for this domain. For the case without chemical reaction, the simulation requires solution of the momentum, continuity and energy balance equations. For the monolith, the momentum conservation equation (also called Volume Average Navier-Stokes, or VANS), with the porous inertial term defined using Darcy's law is [5]:

$$\frac{\partial}{\partial t}\left(\rho_f v_S\right) + \nabla\cdot\left(\rho_f v_S v_S\right) = -\nabla P + \nabla\cdot\tau - \left(\frac{\mu}{K} v_S\right) \tag{3.40}$$

where K is the permeability. For a structured monolith the flow is permitted along the channel direction only. This uni-directional flow can be imposed by using the Darcy permeability in the flow direction, with a very low permeability imposed in the transverse directions. It is sufficient to impose a permeability value in these directions two orders of magnitude lower than in the flow direction for a monolith to ensure flow along the channels [6]. The velocity is the superficial velocity, that is, the velocity based on the total cross sectional area. In the open space, we use the standard $k-\varepsilon$ turbulence model with default parameters. The boundary conditions used for these equations are no slip condition on the walls, a uniform inlet velocity, and at the outlet a pressure condition with zero viscous stress.

The solid phase energy balance is:

$$(1-\phi)\rho_S C_{P,S} \frac{\partial T_S}{\partial t} = \nabla\cdot\left(k_{\mathrm{eff},S}\nabla T_S\right) + h a_v (T_f - T_S) + S \tag{3.41}$$

The subscripts S and f refer to solid and fluid phases respectively. For the solid, the effective thermal conductivity in the flow direction is the solid thermal conductivity multiplied by the solid fraction. Effective thermal conductivities were computed using the methods outlined in [7], using the electrical model with parallel resistances. The source term is zero in the absence of reaction, and with reaction present it is given by:

$$S = (\Delta H_R)\varphi\eta\left(-R_{\mathrm{CH}_4}\right) \tag{3.42}$$

The enthalpy of the reaction in kJ/mol is a function of temperature [5]:

$$(\Delta H_R^o)_{\mathrm{CH}_4} = -806.9 + 1.586\times10^{-2}T - 8.485\times10^{-6}T^2 - 3.963\times10^{-9}T^3 + 2.16\times10^{-12}T^4 \tag{3.43}$$

For the fluid phase, we invoke the pseudo-steady state assumption, where the gas temperature and composition is assumed to be at steady state with the evolving solid temperature [5]. The steady state fluid phase energy balance in the monolith sub-domain is:

$$\nabla\cdot\left(k_{\mathrm{eff},f}\nabla T_f\right) - \rho_f C_{P,f} v_S \cdot \nabla T_f - h a_v (T_f - T_S) = 0 \tag{3.44}$$

The effective axial thermal conductivity of the fluid in the monolith is calculated by analogy to Taylor-Aris dispersion [5],

$$k_{xf,\mathrm{eff}} = k_f + \frac{\left(\nu_S D_H \rho_f C_{P,f}\right)^2}{\phi^2 192\, k_f} \tag{3.45}$$

The thermal conductivity of the fluid is a function of temperature:

$$k_f = 0.01679 + 5.073\times10^{-5}\, T \quad \frac{\mathrm{W}}{\mathrm{m^2K}} \tag{3.46}$$

The transverse thermal conductivity of the fluid is set to zero. The heat capacity of each gas species was described by a third-order polynomial function of temperature using data from [5]. The mixture heat capacity was calculated using a weighted molar average.

$$C_P = a + bT + cT^2 + dT^3 \tag{3.47}$$

The mass balance equation is required when reaction is present. The equation contains terms for the bulk axial flow and axial dispersion. Transverse flow by advection and dispersion is zero. The steady state fluid phase mass balance equation is written in terms of the coordinate x:

$$\phi \frac{\partial}{\partial x}\left(D_{x,\text{eff}}\, \rho_f \frac{\partial w_{\text{CH}_4}}{\partial x} \right) - v_S\, \rho_f \frac{\partial w_{\text{CH}_4}}{\partial x} - k_m\, a_v\, \rho_f \left(w_{\text{CH}_4,f} - w_{\text{CH}_4,S} \right) = 0 \tag{3.48}$$

Note the inclusion of the porosity (fractional open frontal area) term, ϕ. The effective axial dispersion coefficient is calculated using Taylor-Aris dispersion [5], where the result for circular channels is used to approximate the square channels actually present, with the hydraulic diameter, D_H, replacing the diameter, thus.

$$D_{x,\text{eff}} = D_{\text{AB}} + \frac{\left(v_S\, D_H \right)^2}{\phi^2\, 192\, D_{\text{AB}}} \tag{3.49}$$

The molecular diffusion coefficient, D_{AB}, of methane in air is calculated using the Fuller method. With pressure in Pa and the temperature in Kelvin, the binary diffusion coefficient is [5]:

$$D_{\text{AB}} = 9.99\times10^{-5}\ \frac{T^{1.75}}{P}\ \frac{\text{m}^2}{\text{s}} \tag{3.50}$$

The fluid is treated as an ideal gas with mass density given by:

$$\rho_f = \frac{\bar{M}\, P}{R_g T} \tag{3.51}$$

The solid phase mole balance is:

$$0 = \eta\varphi\left(-R_{\mathrm{CH_4}}\right) + k_m a_v \rho_f \left(w_{\mathrm{CH_4},f} - w_{\mathrm{CH_4},S}\right) \tag{3.52}$$

Note that in this equation, the reaction rate is given in terms of the washcoat volume, and φ is the fraction of the monolith volume occupied by the washcoat.

The partial differential equations governing the reactor performance were solved using COMSOL Multiphysics version 4.1.

As mentioned in Section 3.2, many simulations were performed without the inclusion of chemical reaction, and in this case the mass balance equation is not needed, nor are the reaction source terms in the energy balance equation. Following this study (discussed in Section 3.4), the catalytic combustion of methane was included to investigate the effect on conversion of the recuperative operation. If one wishes to include the reaction in a rigorous way, then a detailed mechanistic model can be used. For the catalytic combustion of methane, the model proposed by Deutschmann et al. [8] is probably the best known, and that model was used in this investigation. This mechanism uses 24 surface reactions to model the combustion of methane. Because of the high temperatures that are used for methane combustion, it is possible that diffusion limitation occurs within the washcoat, and thus this effect has to be included. The magnitude of the diffusion effect depends in part on the shape of the washcoat, which tends to be non-uniform in thickness when square monolith channels are used. For this work, it was assumed that the washcoat forms fillets in the corner, as shown in Figure 3.4 (which shows one eighth of the washcoat in a channel, which is assumed to be symmetrical). It is necessary to calculate the average reaction rate in the washcoat using a reaction sub-model, which was done in the following manner.

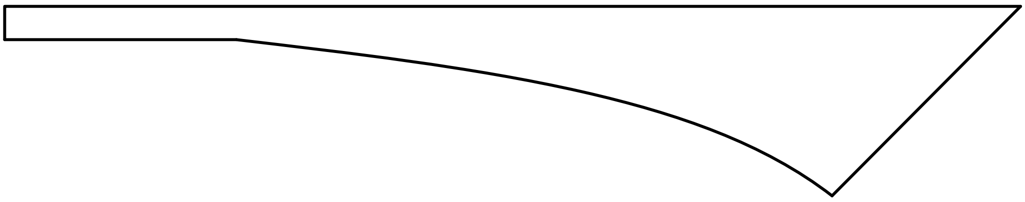

Figure 3.4 – Illustration of the fillet shape used to model the washcoat.

Consider the diffusion and reaction occurring in a washcoat. The mass balance equation for a fillet can be written in two dimensions as follows:

$$\nabla\left(D_{\text{eff}}\,\rho_f\,\nabla w_{\text{CH}_4}\right) - \left(-R_{\text{CH4}}\right) = 0 \tag{3.53}$$

This model is in essence a slice of monolith, and calculation of the mass fraction in the washcoat using this equation implies that the diffusion in the axial direction is not significant. This assumption has been reported to be acceptable. The reaction rate of methane can be calculated from the Deutschmann mechanism using methods they have described [8]. In this work, we assumed that the adsorbed species are in equilibrium with the gas phase. The reaction rates were then calculated using the open source software Cantera [9]. Dirichlet conditions of constant temperature and mass fraction were imposed at the boundary corresponding to the gas/solid interface. The washcoat fillet was assumed to be isothermal, which has also been shown to be a good assumption [10]. The solution for the concentration distribution in the fillet was performed using COMSOL, and the average reaction rate computed by the integration of the total flux along the boundary divided by the cross-sectional area of washcoat.

To use a complex mechanistic model in a non-uniform washcoat is computationally prohibitive unless special measures are taken. In this work, the average reaction rate occurring in the washcoat fillet was pre-computed and stored in a look-up table that was simply accessed during the execution of the recuperator simulation code. Although the construction of the look-up table takes some time, it is built once and for all beforehand, and therefore many recuperator simulations can be performed in a cost effective manner using this table. The use of pre-computed rate data for complicated reaction mixtures has long been used in homogeneous reaction [11 - 13], and more recently in surface reactions [14, 15]. In essence, the reaction rate is approximated using a set of multivariate spline functions on a regular multidimensional grid. It has been shown that multi-dimensional splines can be effectively used for this purpose by pre-computing the polynomial coefficients and storing them in a database [14]. In this work we used cubic splines, which have been shown to give the smoothest interpolation of a given dataset [16]. The spline functions were built using MATLAB. The method is equivalent to using the look-up table T3 described in Chapter 2.

Section 3.4 presents some results and discussion obtained in the presence and absence of reaction.

3.4 Results and discussion

One of the key design parameter for the recuperative converter concept, regardless of design, is the extent of accumulation of energy, which is quantified by the maximum temperature attained in the reactor. This temperature is obviously important in achieving the appropriate level of combustion. For systems with reaction, this effect is often quantified by the multiple of the adiabatic temperature rise corresponding to 100 % conversion that is observed. In this first section of the investigation, we do not consider a reaction, but rather input a known quantity of thermal energy in the mixing section at the end of the reactor (see Figure 3.3). This preliminary investigation was done to explore the reparative powers of the proposed design without considering the complexities of the reaction. The performance of the converter can be quantified by some parameters. For example, the maximum temperature achieved in the system is quantified by an enhancement factor, defined as:

$$F_E = \frac{T_{\mathrm{max}} - T_{\mathrm{in}}}{T_{\mathrm{out}} - T_{\mathrm{in}}} \tag{3.54}$$

This definition of the enhancement factor may give a misleading impression of the efficiency of the recuperator, because the maximum temperature might be very localized. In general, the highest temperatures occur along the inlet of the return section, and therefore, to give a more realistic picture of the enhancement factor, the maximum temperature in Equation (3.15) was replaced by the average temperature along the inlet of the return monolith section. The difference between the inlet and outlet temperatures at steady state is determined by the amount of thermal energy added to the system, either by exothermic chemical reaction or addition by heat transfer. For a non-reacting system at steady state, an energy balance gives the overall temperature rise for a given input level of energy:

$$q = \dot{m} C_P \left(T_{\mathrm{out}} - T_{\mathrm{in}} \right) \tag{3.55}$$

In this case, the mass flow rate is the value for the monolith slice. The equation can easily be re-arranged to give an explicit equation for the added energy required to give a specified maximum temperature in the system by incorporating the enhancement factor, viz:

$$q = \frac{\dot{m} C_P}{F_E} \left(T_{\mathrm{max}} - T_{\mathrm{in}} \right) \tag{3.56}$$

The maximum temperature in the reactor in operation will be limited by the twin requirements of methane conversion and reactor/catalyst longevity.

To quantify the influence of geometry and velocity, results are presented in terms of space time, which is here defined as twice the length of monolith (total monolith flow path) divided by the inlet velocity referenced at 400 K. Typical operating conditions for a catalytic converter are a GHSV from 25 000 to 100 000 h^{-1}, which corresponds to a space time of between 0.04 and 0.14 s. If we assume that the recuperative converter will have some additional volume, then the upper limit of realistic space times could be taken as about 0.5 s.

To gain some physical insight into the competitive heat transfer processes occurring, and as an aid in interpreting the results obtained, we can write a simple energy balance for the recuperator using a simple pseudo-homogeneous model without reaction. It should be emphasized here that this simple model is only being discussed to illustrate some underlying parametric groups that will govern performance. The heterogeneous model presented earlier was used in all simulations reported in the paper. We let x represent the flow direction and y represent the orthogonal to flow direction. Noting that the fluid only flows in the x direction, and assuming constant physical properties, we can write:

$$k_{x,\mathrm{eff}} \frac{\partial^2 T}{\partial x^2} + k_{y,\mathrm{eff}} \frac{\partial^2 T}{\partial y^2} - v_S \left(\rho C_P\right) \frac{\partial T}{\partial x} = 0 \tag{3.57}$$

Define dimensionless distances based on the reactor length, L, and the section thickness, H:

$$x* = \frac{x}{L}; \qquad y* = \frac{y}{H} \tag{3.58}$$

The energy balance can then be rearranged to give:

$$\left(\frac{k_{x,\mathrm{eff}}}{(\rho C_P) v_z L}\right) \frac{\partial^2 T}{\partial x*^2} + \left(\frac{k_{y,\mathrm{eff}}}{(\rho C_P) v_z H}\right)\left(\frac{L}{H}\right) \frac{\partial^2 T}{\partial y*^2} - \frac{\partial T}{\partial x*} = 0 \tag{3.59}$$

The temperature distribution thus depends on transverse and axial Peclet numbers, and the aspect ratio of the reactor.

$$\left(\frac{1}{\mathrm{Pe}_a}\right) \frac{\partial^2 T}{\partial x*^2} + \left(\frac{1}{\mathrm{Pe}_T}\right)\left(\frac{L}{H}\right) \frac{\partial^2 T}{\partial y*^2} - \frac{\partial T}{\partial x*} = 0 \tag{3.60}$$

We can thus see that the critical variables will be the length, section height, and the effective thermal conductivities in the transverse and flow directions. It should also be noted that increasing the section thickness, everything else being equal, reduces the area available for heat transfer for a given reactor volume. It can be shown that the total heat transfer per unit reactor volume is equal to the inverse of the total section thickness.

To illustrate the recuperator performance, the study in this case considered total monolith lengths of 15, 20 and 25 cm. The section thickness for each flow pass was varied from 10 mm to 40 mm. Two monoliths were used, representing Cordierite silicon carbide. The substrate thermal conductivities were taken as 1.5 and 15 W/(m·K) respectively. Both monoliths were assumed to contain 12 % by volume washcoat with a thermal conductivity of 0.5 W/(m·K). The effective radial thermal conductivities are thus 0.292 W/(m·K) for Cordierite and 4.0 W/(m·K) for silicon carbide respectively. For these simulations, the inlet temperature was chosen to be 400 K in all cases. A desired outlet temperature was specified and then the necessary added energy was calculated to give this outlet temperature for the appropriate space time.

We consider first the Cordierite monolith. The variation of the enhancement factor with space time for three monolith lengths is shown in Figure 3.5. It is seen that the length makes a contribution to the enhancement factor at longer (unrealistic) space times. (The mean residence time is likely more representative, however, it is more complex to deal with as a result of the variable density). The simulations were repeated for three different outlet temperatures (420, 450 and 500 K) and there was negligible difference between the curves. As the specified outlet temperature increased further, it was found that the enhancement factor had a tendency to fall, however, the reduction was only significant at larger space times, and at these space times the maximum temperature was excessive. It can be seen from Figure 3.5 that for a realistic space time an enhancement factor up to 5 is achieved for the Cordierite monolith with a 10 mm total layer thickness.

Figure 3.6 shows the effect of increasing the layer total thickness from 10 mm to 40 mm, again for the Cordierite monolith with a length of 15 cm. It is seen that the enhancement factor decreases with increasing layer thickness. The trend in this result is as expected, however, from the magnitude of the drop it can be concluded that the use of Cordierite monoliths would likely only be practicable with relatively thin flow sections.

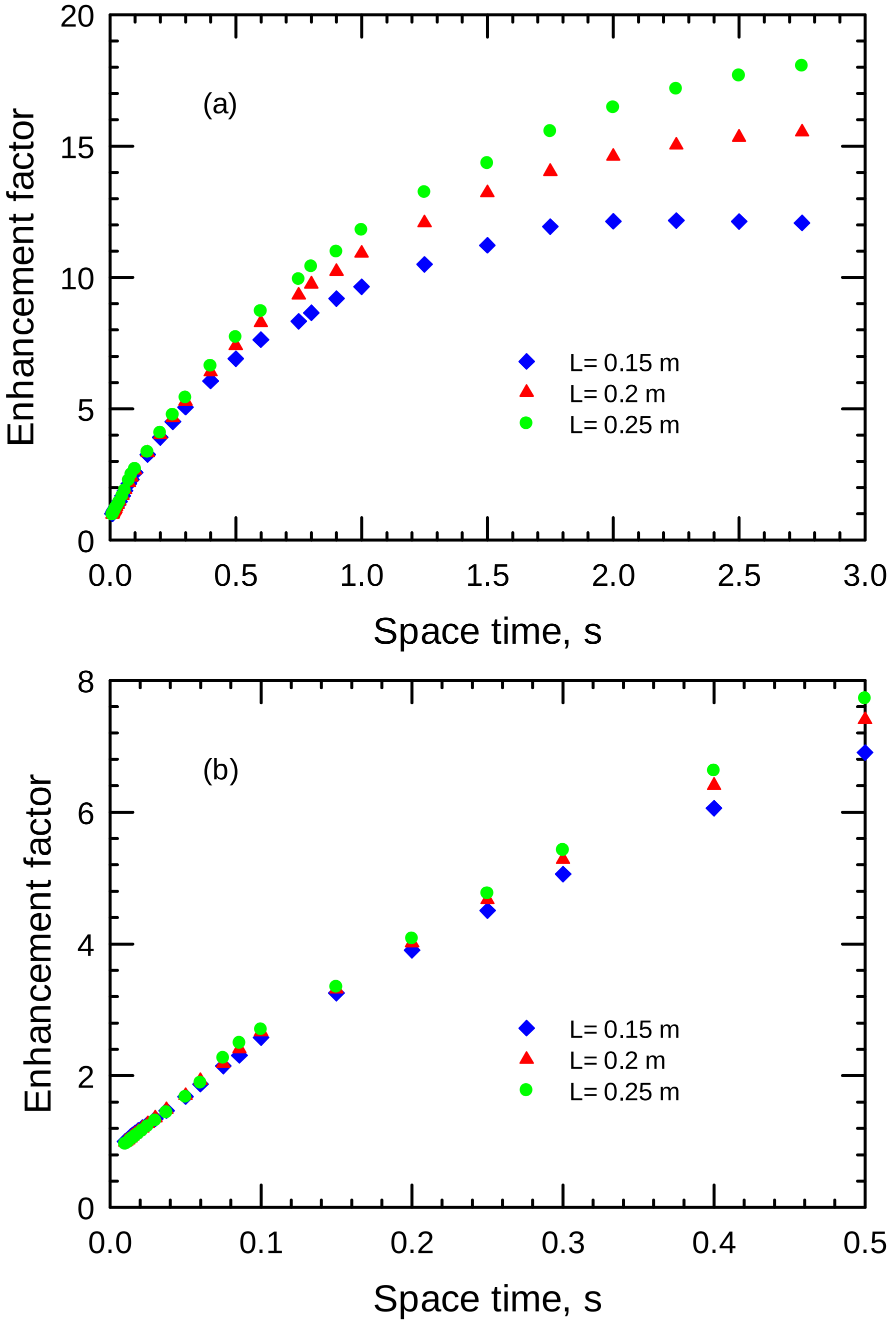

Figure 3.5 - Variation of enhancement factor as function of space time for a system composed of a 400 CPSI Cordierite monolith with a layer thickness of 10 mm and different total length. (a) range of space time up to 3 s and (b) range of space time up to 0.5 s.

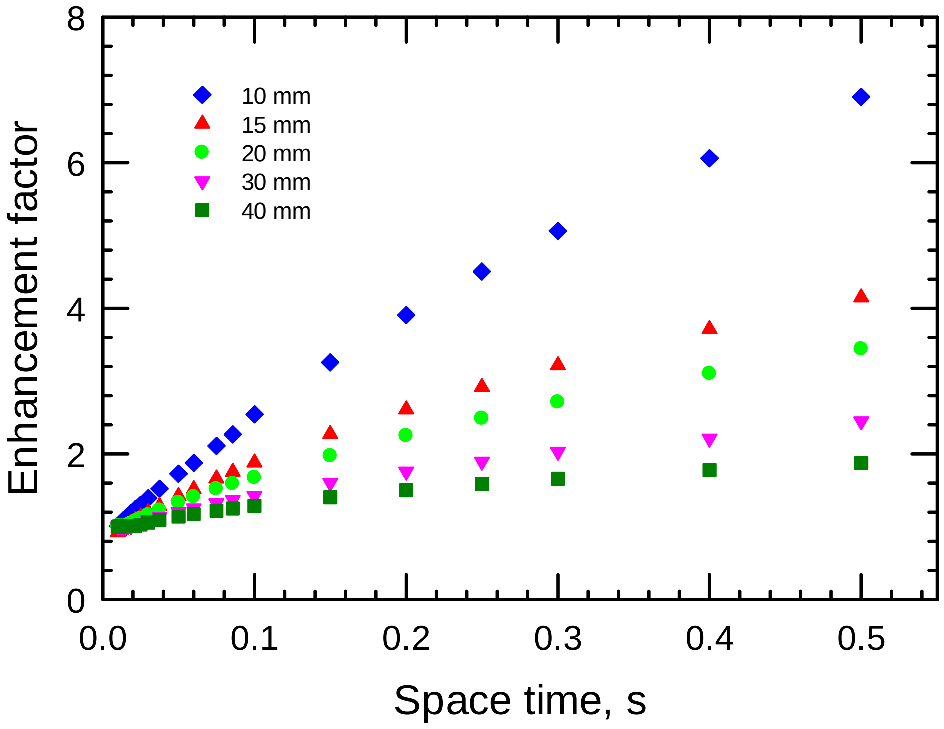

Figure 3.6 - Variation of enhancement factor in the reactor as function of space time and thickness of each flow section. The Cordierite monolith was 15 cm long.

The radial effective thermal conductivity is a key parameter in making the proposed design a success. The increased use of silicon carbide in auto exhaust gas after treatment devices has meant that it is practical to consider its use in the recuperator design. As noted, the thermal conductivity of the substrate is about an order of magnitude higher than Cordierite.

Figure 3.7 shows the results obtained for a substrate with higher value of thermal conductivity. Comparing the result to those shown in Figure 3.6, it is seen that the enhancement factor rises more quickly at much lower space time and then more rapidly than the case for Cordierite. Figure 3.8 then shows the effect of section thickness for the silicon carbide. The same trend is observed as with the Cordierite, but the overall enhancement factors are higher. A direct comparison between the enhancement factors for Cordierite and silicon carbide for the 10 mm thick sections is shown in Figure 3.9. The superiority of the silicon carbide is evident.

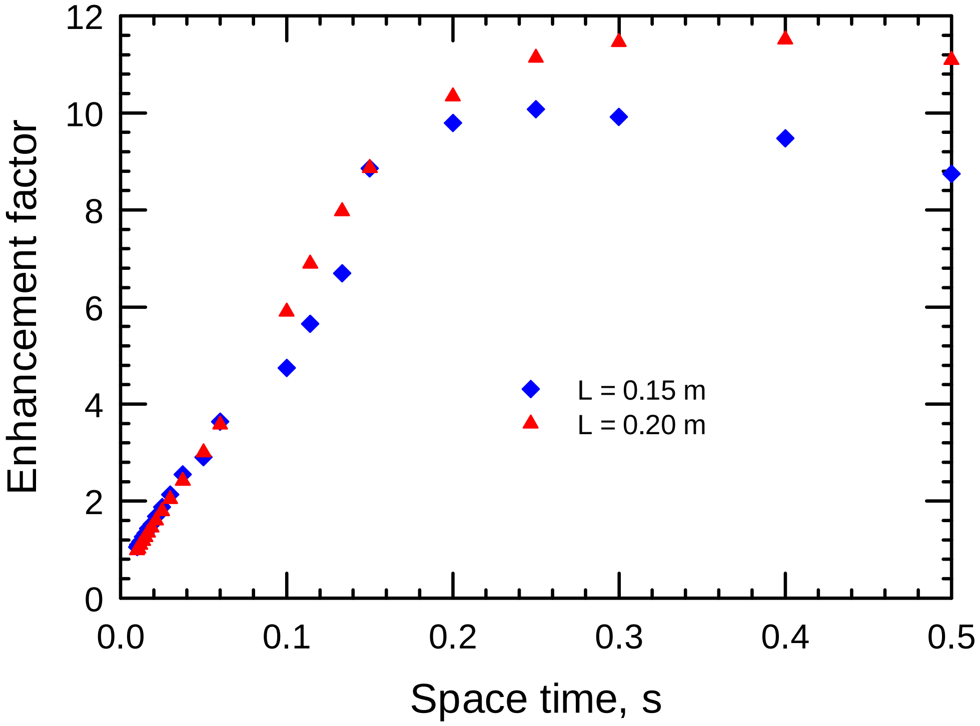

Figure 3.7 - Variation of enhancement factor as function of space time for a system composed of a 400 CPSI silicon carbide monolith with a layer thickness of 10 mm and different total length.

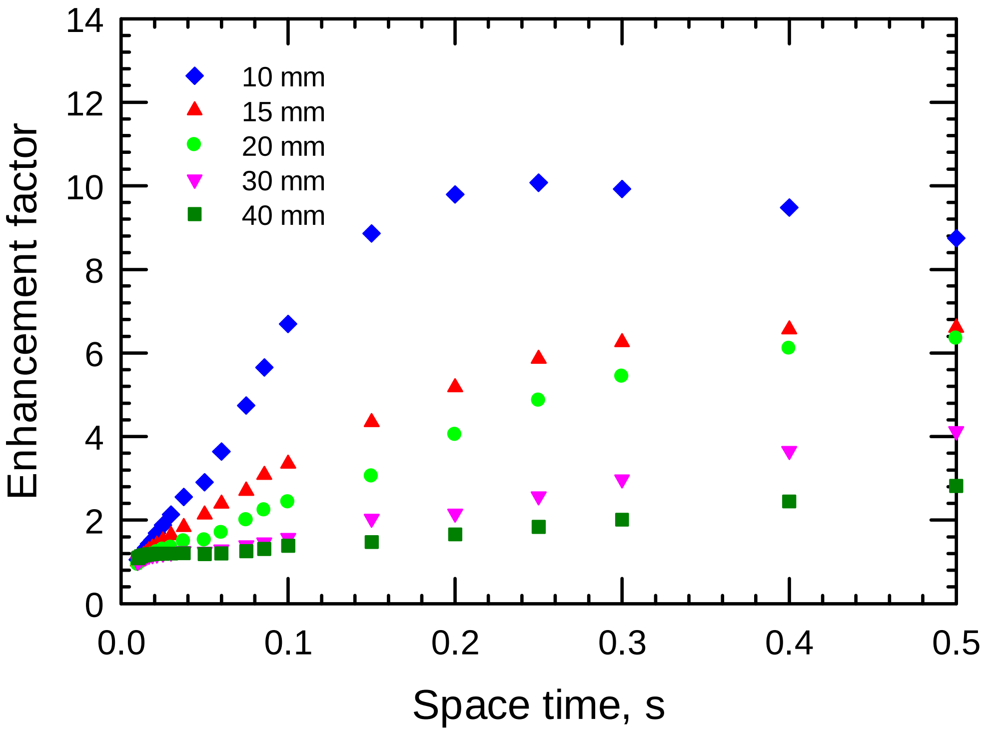

Figure 3.8 - Variation of enhancement factor in the reactor as function of space time and thickness of each flow section. The silicon carbide monolith was 15 cm long.

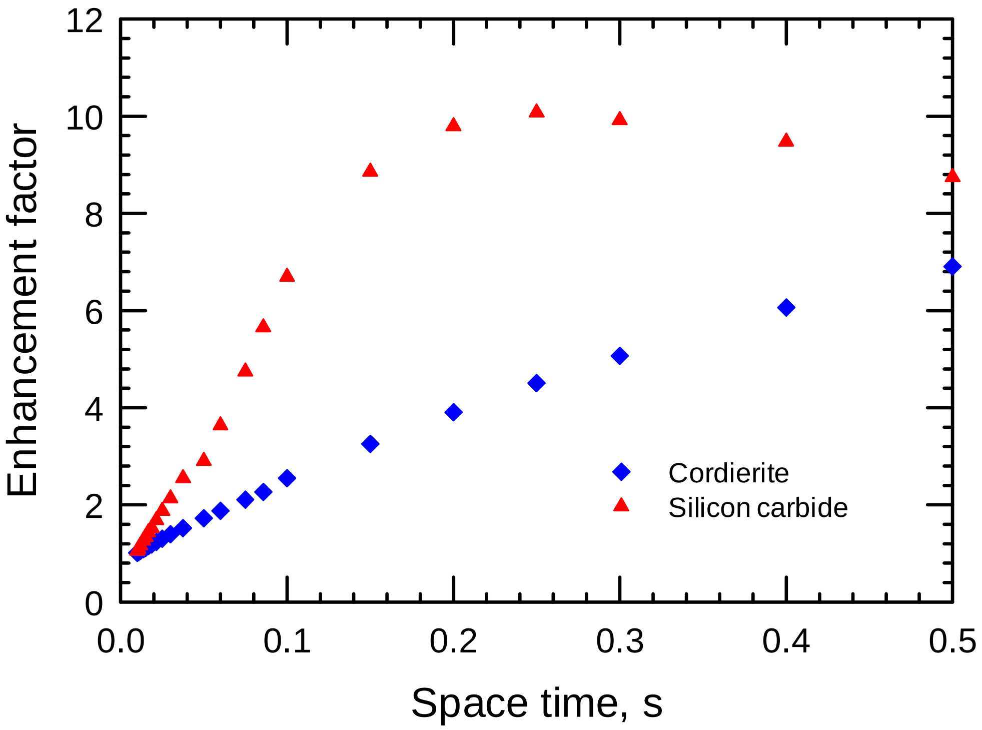

Figure 3.9 – Comparison of enhancement factors for the cordierite and silicon carbide monoliths with a length of 15 cm and a section thickness of 10 mm.

The second set of simulations shows the conversion of methane using the kinetics presented earlier. The feed to the reactor contained 500 ppm by volume methane in air, and the inlet temperature was 400 K to simulate a low exhaust gas temperature. It is evident that at these conditions some energy would have to be added to maintain combustion. We consider the case of a 15 cm long converter with a section thickness of 10 mm, with an inlet velocity of 1.5 m/s. The resulting space time is therefore 0.2 s. Figure 3.10 shows the conversion as a function of thermal energy added in the mixing section. It is seen that the conversion increases as a function of energy added, which is to be expected. Furthermore, it is evident that the higher thermal conductivity silicon carbide requires about one half of the added energy for the case of the Cordierite substrate.

It is worthwhile to point out that the combustion of methane produces of the order of 50 kJ/g. To achieve complete combustion of the input methane stream requires about 100 kJ/kg of feed for the silicon carbide monolith, which corresponds to about 3800 ppm of methane being added to aid the combustion process. In an automotive exhaust, some CO would be present, which would reduce the requirement for added methane. It should also be pointed out that this value of 3800 ppm is based on an inlet gas temperature of 400 K. A higher inlet gas temperature would require less additional methane to be added.

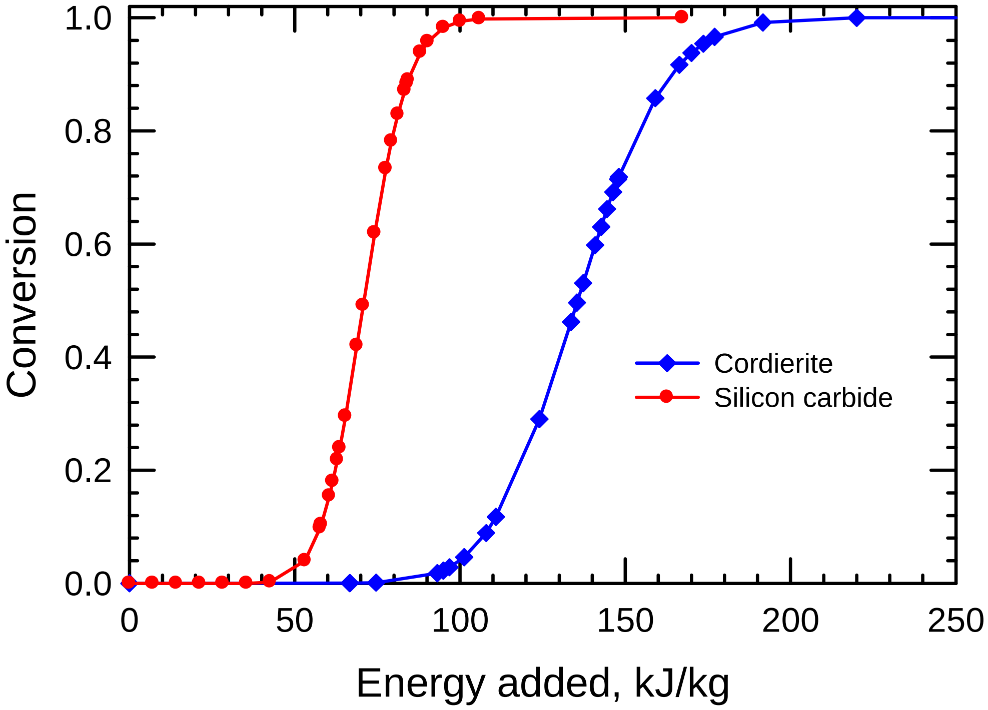

Figure 3.10 – Conversion of methane as a function of heat added to the system for Cordierite and silicon carbide monoliths. The sections are 10 mm thick and the monoliths were 15 cm in length.

3.5 Concluding remarks

This study has demonstrated the heat trapping effect of the recuperative catalytic converter. For a given space velocity that is typical for the operation of a natural gas powered vehicle, it has been seen that the combustion of added methane is able to elevate the reactor temperature to a level sufficiently high to achieve catalytic combustion of methane. The actual performance will depend on factors such as the real catalyst activity and the size of the unit. To explore further the feasibility of using such a device, a more detailed parameteric study should be conducted based on a specific catalyst. The results should be compared for efficiency with the design where a separate reactor and heat exchanger are used, to determine which design offers the most promise.

NOMENCLATURE

a_v	Surface area per unit volume, $\mathrm{m^2/m^3}$
C_P	Constant pressure heat capacity, $\mathrm{J/kg \cdot K}$
D_H	Hydraulic diameter, m
G	radial conduction factor for a monolith, dimensionless
h	Heat transfer coefficient, $\mathrm{W/m^2K}$
H	Thickness of a monolith section, m
(ΔH_R)	Enthalpy change of reaction, J/mol
k	Thermal conductivity, $\mathrm{W/m \cdot K}$
$k_{xf,\mathrm{eff}}$	effective thermal conductivity of fluid, flow direction, $\mathrm{W/(m \cdot K)}$
$k_{x,\mathrm{eff}}$	effective thermal conductivity of monolith, flow direction, $\mathrm{W/(m \cdot K)}$
$k_{y,\mathrm{eff}}$	effective transverse thermal conductivity of monolith, $\mathrm{W/(m \cdot K)}$
k_m	Mass transfer coefficient, m/s
K	Permeability, $\mathrm{m^2}$
L	length of reactor, m
$\dot{m}$	mass flow rate, kg/s
M	Molar mass of a substance, g/mol
P	Pressure, Pa
q	Energy added to reactor, J
R_g	Gas constant, $\mathrm{J/(mol \cdot K)}$
$\left(-R_{\mathrm{CH_4}}\right)$	rate of disappearance of methane, $\mathrm{mol/(m^3 s)}$
$\left(-\bar{R}_{\mathrm{CH_4}}\right)$	Average rate of disappearance of methane, $\mathrm{mol/(m^3 s)}$
S	Source term in energy equation
t	Time, s
T	Temperature, K
v	Velocity, m/s
w	Mass fraction

x	coordinate in the flow direction, m
y	coordinate orthogonal to the flow direction, m

Greek Symbols

ρ	Density, kg/m^3
η	Effectiveness factor
ε	Turbulent kinetic energy dissipation rate
ε_W	Fraction of monolith occupied by washcoat
τ	Stress tensor
μ	Viscosity, Pa·s
ϕ	Monolith porosity
φ	fraction of reactor occupied by washcoat

Subscripts

f	Fluid
i	Species
S	Solid, surface or superficial

References

[1] S.W. Churchill, Int. J. Chemical Reactor Engineering, 5 A55 (2007).

[2] B. Liu, M.D. Checkel and R.E. Hayes., Cdn. Journal of Chemical Engineering, 79 (2001) 491-506.

[3] G. Kolios, A. Gritsch, A. Morillo, U. Tuttlies, J. Bernnat, F. Opferkuch and G. Eigenberger, Applied Catalysis B: Environmental, 70 (2007) 16-30.

[4] J. Bernnat, M. Rink, U.Tuttlies, T. Danner, U. Nieken and G. Eigenberger, Topics in Catalysis 52 (2009) 2052-2057.

[5] R.E. Hayes, S.T. Kolaczkowski, Introduction to catalytic combustion, Gordon and Breach Science Publishers, Reading, UK. (1997)

[6] B. Liu, R. E. Hayes, Y. Yi, J. Mmbaga, M. D. Checkel and M. Zheng, Computers and Chemical Engineering, 31 (2007) 292-306.

[7] R.E. Hayes, A. Roijas, and J.P. Mmbaga, Catalysis Today, 147S (2009) S113-S119.

[8] O. Deutschmann, R. Schmidt, F. Behrendt, J. Warnatz, in: Proceedings of the 26th International Symposium on Combustion, The Combustion Institute, Pittsburgh, PA, (1996) 1747–1754.

[9] D. Goodwin,. In M. Allendorf, F. Maury, & F. Teyssandier (Eds.), Chemical Vapor Deposition XVI and EUROCVD 18,(2003) 155-162

[10] D. Leung, .R.E. Hayes, S.T. Kolaczkowski, Can. J. .Chem. Eng., 74 (1996) 94-103.

[11] W.S. Meisel, D.C. Collins, IEEE Transactions on, 3 (1973) 349–358.

[12] T. Turanyi, Computers & Chemistry 18 (1994) 45-54.

[13] T. Turanyi, Proceedings of the Combustion Institute, 25 (1995) 949-955.

[14] M. Votsmeier, Chemical Engineering Science, 64 (2009) 1384-1389.

[15] A. Scheuer, O. Hirsch, R.E. Hayes, H. Vogel, M. Votsmeier, Catalysis Today, 175 (2011) 141-146.

[16] C. De Boor, A Practical Guide to Splines, Springer, New York, (1978)

Chapter 4:

Applications of Multi-scale modelling to Catalytic Converters: Effect of cell density on methane ignition in a monolith reactor

Overview

This chapter describes a parametric study of a monolith reactor for the combustion of lean methane mixtures. The effect of the monolith substrate cell density on the light-off curve is examined. Six monolith substrates are examined, with different cell densities or wall thickness. The monoliths are treated in a consistent manner, with a constant catalyst and washcoat loading in each case. A complex mechanistic kinetic model for the combustion of methane is used. All of the internal and external heat and mass transfer resistance are treated consistently at the appropriate scale. The sub-models for the reaction rate, internal and external mass transfer are pre-computed and stored in look-up tables.

This chapter is a modified version of the paper --- A. Fadic, T. Nien, J.P. Mmbaga, R.E. Hayes and M. Votsmeier, A Case Study in Multiscale Model Reduction: Effect of Cell Density on Methane Ignition in Monolith Reactors, to be submitted to the *Canadian Journal of Chemical Engineering*

4.1 Introduction

Automotive catalytic converters are used in most vehicles to meet government mandated emission limits. The standards are getting tighter since their implementation as the number of cars in circulation increases and hence, the total level of emissions due to these sources. The role that these reactors play in the car is to perform a chemical reaction that is able to destroy these compounds in order to meet the requirements. However, usually these reactions would not take place under the exhaust gases conditions unless a catalyst is used. To be able to use this solid catalyst efficiently, monolith substrate type are built, whose surface is coated with a thin catalytic washcoat. The coated monolith is encased in a can, which is placed appropriately in the exhaust system. There are many spatial configurations possible, which exhibit different flow and temperature patterns. One of these configurations is the cell density measured by Cells per Square Inch (CPSI). Another parameter that can be modified in a monolith is the wall thickness, usually measured in thousands of an inch (mil). The main objective of this work is to study the influence of these parameters in a full scale reactor, taking into account all of the physics involved.

Detailed optimization of converter design is a time consuming process, and furthermore, configurations are often restricted by the automobile design. To evaluate the performances of different configurations, physical models could be built, but doing this has the downside of being a time consuming process and very expensive. Another approach to evaluate the performance is to use computational methods, such as Computational Fluid Dynamics (CFD). CFD is very demanding in terms of computing capabilities, however, computing power has increased over the years allowing faster and more accurate CFD calculations with low cost desktop computers, by using commercially available or open source CFD packages such as COMSOL Multiphysics, FLUENT, CFX, FLOW3d, PHEONICS, STAR-CD or OPEN FOAM, which solve the conservation equations for momentum, mass or energy by using either the Finite Elements Method (FEM) or the Finite Volume Method (FVM).

There are two approaches used to model monolith reactors with CFD tools. One approach is based on the single channel model [1], in which only one channel is considered, and it is assumed that all channels will have the same behaviour, so the full model can be computed from that result. However, flow mal-distribution and energy transfer in a full scale reactor means that this assumption is not usually valid [2]. It would therefore seem inevitable that the full spatial model for the converter must be solved in either two or three dimensions, however, to model the real physical space of a full size monolith converter, which even for small units contain thousands of channels, is very costly in terms of computer time. See, for example, the fully discrete model developed by [3], who used the Lattice Boltzmann method to solve a converter problem for a monolith with about 7500 channels. They did not include heat transfer effects or reactions, and a simulation took a few weeks on several hundred processors working in parallel. Although new hardware and software will likely make this approach more feasible in the not too distant future, most converter models use a volume averaging process and treat the model as a continuous porous medium [4, 5]. Volume averaging causes a loss of information at the micro-level, but elucidates the macroscopic flow patterns, which are needed to understand the converter operation. Another technique is the representative channel method, in which a few channels are modelled in detail, and then combined with a macro-model for the whole converter [6, 7].

As noted above, the use of continuum model leads to a loss of spatial resolution at the channel scale. As shown in Figure 4.1 (from [14]), and discussed in Chapter 2, to consider the effects of mass and heat transfer correctly, it is important to take into consideration the shape of the washcoat in the channel. To allow the inclusion of both complex kinetics and small scale heat and mass transfer effects, Nien et al. [8] (Chapter 2) implemented a lookup table technology, which reduces the computing power required to run a full scale model by using pre-computed data, and which retains all of the small scale information in the full scale model One of the most remarkable results is the reduction of time required to compute a solution to a full scale reactor model using the lookup tables compared to the computation using a chemistry module such as Cantera. The speed-up factor could be up tp five orders of magnitude when modelling a complete converter with complex kinetics.

The purpose of this paper is to report a full scale approach of the modelling of the catalytic converter, placing an emphasis on the versatility of the lookup table approach, which allows the solution of a very complex problem that includes a complex kinetics mechanism and internal and external diffusion in a simple manner. We investigate the effect of cell density on the ignition of methane on a monolith with platinum catalyst. The experiment was set up as the transient simulation of the catalytic converter, comparing their performances in terms of the light-off curves and in terms of the backpressure. It is reiterated that all internal and external mass and heat transfer effects are handled in a consistent manner.

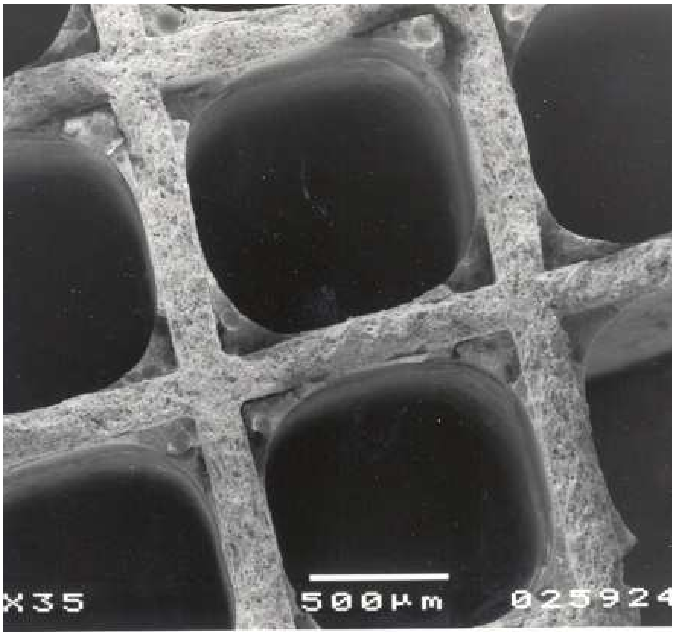

Figure 4.1 - Scanning electron micrograph of a monolith with square cells and a catalytic washcoat. From [14].

4.2 Shape optimization of a catalytic converter

As noted earlier, CFD can be employed as a computational design tool to aid in the optimisation of a converter system. Interest in shape optimisation to maximise conversion whilst minimizing such variables as precious metal loading and pressure drop have been the subject of much interest over the past decade [9], and some of the more significant CFD studies are discussed in [2]. The design and optimisation of a converter can be divided into two parts, although they are coupled. The first part could be considered to be aspects external to the monolith structure, such as monolith size and shape, can sizing, diffuser angle, flow altering devices, etc., whilst the second part is the monolith structure itself. In this second part we can include such things as cell size and shape.

In recent years there has been considerable interest in high cell density monolith, as well as thin and ultrathin wall substrates, see, for example [10 - 13]. When changing the cell density, several factors are important. Considering square cells in a ceramic monolith, for example, the washcoat forms fillets in the corner, as shown in Figure 4.1 (from [14]). Let us assume that we use the same volume of catalytic washcoat, with the same catalyst loading, in monolith substrates with different cell densities. The following physical changes are present: the channel size (hydraulic diameter) changes, the amount of washcoat in each channel will be different, thus so will its size. An increase in cell density will give a reduction in the channel hydraulic diameter, which in turn will reduce the external mass transfer resistance in the channel. With less washcoat per channel, a higher density substrate will have a thinner washcoat. This gives a lower internal diffusion resistance [15].

In addition to changing the cell density, it is also possible simply to make the substrate wall thinner. A reduction in the wall thickness will increase the channel diameter, thus giving an increase in the external diffusion resistance. However, the washcoat will become thinner, thus reducing the internal diffusion resistance. For a constant mass flow rate, the mean residence time will also increase as the velocity is reduced owing to an increase in monolith porosity. The reduction in velocity will also give lower back pressure. A change in channel diameter also affects the monolith permeability. Generally, a decrease in permeability will increase the back pressure, which will give a more uniform flow distribution. Finally, changing the cell density and wall thickness affects the thermal mass of the system. The thermal mass is the product of the bulk density and the heat capacity. A reduction in thermal mass results in a faster thermal response. A summary of the properties of six typical monolith ceramic substrates with square channels and a 12 volume % washcoat loading is given in Table 4.1. The geometric data are based on information from Corning Inc. and from [16]. We emphasize that it is important to maintain consistency if the comparison is to be valid. For example, Lun et al. [17] performed CFD simulations using the CFD package AVL on monoliths of constant cell density with varying wall thickness. They compared their CFD results with the experimental velocity profile of Holmgren et al. [18]. They used Voltz [19] kinetics and ignored washcoat diffusion. It appears that the comparisons for different wall thickness did not use the same mass of washcoat in each case.

In the remainder of this paper, we present computational results that compare these six substrate configurations with one converter geometry. Catalyst loading is maintained at the same level on each substrate, so as to ensure a fair comparison.

Table 4.1 – Data for six monolith substrate designs with 12 % by volume catalyst loading.

	A	B	C	D	E	F
Property	Standard	Thin wall	Thin wall	Ultrathin wall	Ultrathin wall	Ultrathin wall
Cells per square inch, CPSI	400	400	600	400	600	900
Cells per square metre, CPSM	620000	620000	930000	620000	930000	1395000
Wall thickness, mil	6.5	4.3	4.3	2.5	3.5	2.5
Wall thickness, mm	0.1651	0.1092	0.1092	0.0635	0.0889	0.0635
Substrate channel size, mm	1.105	1.161	0.928	1.207	0.948	0.783
Substrate volume fraction	0.243	0.165	0.200	0.097	0.164	0.144
Washcoat volume fraction	0.12	0.12	0.12	0.12	0.12	0.12
Fluid volume fraction (OFA)	0.637	0.715	0.680	0.783	0.716	0.736
Average washcoat thickness, micrometres	45.68	43.30	36.18	41.54	35.34	28.50
Hydraulic diameter, D_h, mm	1.014	1.074	0.855	1.123	0.877	0.726
Geometric surface area, GSA m^2/m^3	2514	2664	3182	2786	3264	4052
Bulk density substrate, kg/m^3	396.3	268.3	325.3	158.9	267.5	235.3
Bulk density final, kg/m^3	528.3	400.3	457.3	290.9	399.5	367.3
Axial permeability, m^2	2.04E-08	2.6E-08	1.6E-08	3.1E-08	1.7E-08	1.2E-08
Axial thermal conductivity, solid	0.750	0.419	0.489	0.285	0.418	0.379
Radial thermal conductivity, solid	0.362	0.269	0.310	0.194	0.269	0.246

4.3 Mathematical model

4.3.1 General

The geometric domain of the model consists of the monolith, its enclosure and the inlet and outlet diffusers, as shown in Figure 4.2. It is a 2D axisymmetric model. It consists of an inlet pipe of diameter DP, a diffuser cone of angle θ, a porous zone where the solid monolith resides of length L and diameter D. Downstream, the outlet diffuser cone is located and at the end the outlet pipe is located. The parameter values are given in Table 4.1.

A summary of the equations required for the heterogeneous modelling of a monolith reactor system are given in reference [28]. Equations are needed for the conservation of momentum, mass and energy. The form of these equations depends on which part of the system is being considered, either the monolith or the associated pipe work. The model equations are essentially the same as those described in Chapter 2, but are repeated here for completeness.

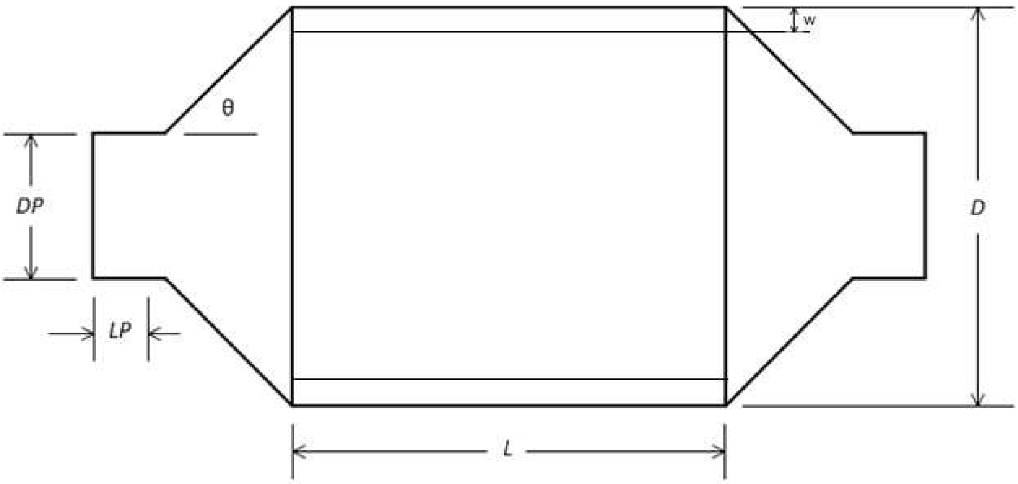

Figure 4.2 – Schematic of the typical catalytic converter studied with key lengths identified.

Table 4.2 – Geometric parameters for Figure 4.2.

Name	value	Comment
DP	0.0254 [m]	Pipe diameter
D	0.0675 [m]	Reactor diameter
LP	0.0254 [m]	Inlet pipe length
L	0.163 [m]	Porous zone length
θ	40°	Diffuser angle
w	0.005 [m]	Insulation width

4.3.2 *Modelling the open sections*

The open sections of a monolith reactor consist of the inlet pipe and diffuser. Here the flow is turbulent, and the Reynolds averaged Navier-Stokes (RANS) equations can be used to model the flow. The continuity equation is:

$$\frac{\partial \rho_f}{\partial t} + \nabla \cdot \left(\rho_f v \right) = 0 \qquad (4.61)$$

The Reynolds averaged momentum transport equation is:

$$\frac{\partial \rho_f v}{\partial t} + \nabla \cdot \left(\rho_f v v \right) = -\nabla p + \nabla \cdot \tau - \nabla \cdot \left(\rho_f \overline{v'v'} \right) \qquad (4.62)$$

To provide closure for the equation set, the additional turbulence term must be quantified. The most common relation is the eddy (or turbulent) viscosity model based on the Boussinesq assumption, where the turbulent stress is given by:

$$\rho_f \overline{v'v'} = -\tau_t = \frac{2}{3} k I - \mu_t \left(\nabla v + \nabla v^T \right) \qquad (4.63)$$

This relationship forms the basis for the RANS turbulence models, which are distinguished by the way in which the eddy viscosity is calculated. The two equation $k-\omega$ model was chosen for this work. It is one of the most widely used turbulence model in engineering practice, along with the $k-\varepsilon$ model. We used the $k-\varepsilon$ model in earlier work (reference [2] and in Chapter 3). The two models give essentially the same results, however it was found that the $k-\omega$ model was more numerically stable. The $k-\omega$ model is a semi-empirical model based on model transport equations for the turbulent kinetic energy (*k*) and its turbulence frequency (ω). They are obtained from the following transport equations:

$$\frac{\partial(\rho k)}{\partial x}+\frac{\partial(\rho u_j k)}{\partial x_j}=\frac{\partial}{\partial x_j}\left[\left(\mu+\frac{\mu_t}{\sigma_\omega}\right)\frac{\partial k}{\partial x_j}\right]+P_k-\beta'\rho k\omega+P_{kb} \tag{4.64}$$

$$\frac{\partial(\rho\omega)}{\partial x}+\frac{\partial(\rho u_j \omega)}{\partial x_j}=\frac{\partial}{\partial x_j}\left[\left(\mu+\frac{\mu_t}{\sigma_\omega}\right)\frac{\partial \omega}{\partial x_j}\right]+\alpha\frac{\omega}{k}P_k-\beta\rho\omega^2+P_{\omega b} \tag{4.65}$$

The eddy or turbulent viscosity, μ_t, is assumed to be as follows:

$$\mu_t=\rho\frac{k}{\omega} \tag{4.66}$$

The following constant values, which have been found to work in a wide range of flows, were used in this work.

$$\beta^{'}=0.09 \quad \alpha=\frac{5}{9} \quad \beta=0.075 \quad \sigma_k=2 \quad \sigma_\omega=2 \tag{4.67}$$

The Reynolds stress is computed as follows:

$$-\rho\overline{u_i u_j}=\mu_t\left(\frac{\partial u_i}{\partial x_j}+\frac{\partial u_j}{\partial x_i}\right)-\frac{2}{3}\delta_{ij}\left(\rho k+\mu_t\frac{\partial u_k}{\partial x_k}\right) \tag{8}$$

The effects of buoyancy, quantified by the terms P_{kb} and P_{wb}, were neglected. The production of turbulent kinetic energy, P_k, is defined as:

$$P_k = \mu_t \left(\frac{\partial u_i}{\partial x_j} + \frac{\partial u_j}{\partial x_i} \right) \frac{\partial u_i}{\partial x_j} - \frac{2}{3} \frac{\partial u_k}{\partial x_k} \left(3\mu_t \frac{\partial u_k}{\partial x_k} + \rho k \right) \tag{9}$$

Turbulent species mass and energy transfer in the open sections can be modelled by analogy to turbulent momentum transfer. The turbulent species mass balance equations are:

$$\rho_f \frac{\partial w_i}{\partial t} + \rho_f v \cdot \nabla w_i = \nabla \cdot \left(\rho D_t \nabla w_i \right) \tag{10}$$

The turbulent energy balance is:

$$\rho_f C_P \frac{\partial T}{\partial t} + \rho_f C_P v \cdot \nabla T = \nabla \cdot \left(k_t \nabla T \right) \tag{11}$$

The effective dispersion coefficient and apparent thermal conductivity are:

$$D_t = D_{i,m} + \frac{\mu_t}{\mathrm{Sc}_t} \tag{12}$$

$$k_t = k_f + \frac{C_p \mu_t}{\mathrm{Pr}_t} \tag{13}$$

4.3.3 Modelling the monolith

The laminar flow in the channels is modelled using the continuum approach, which uses the volume averaged Navier-Stokes equation expressed in terms of the superficial velocity. The steady state equation is:

$$\frac{\partial}{\partial t}\left(\rho_f v_S \right) + \nabla \cdot \left(\rho_f v_S v_S \right) = -\nabla p + \nabla \cdot \tau - \left(\frac{\mu}{\mathbf{K}} v_S \right) \tag{4.68}$$

The continuity equation is:

$$\frac{\partial \rho_f}{\partial t} + \nabla \cdot \left(\rho_f v_S \right) = 0 \tag{4.69}$$

$\mathbf{K}$ is the permeability tensor. For a structured monolith the flow is permitted along the channel direction only. This uni-directional flow can be imposed by using the Darcy permeability in the flow direction, with a very low permeability imposed in the transverse directions [2].

As discussed in [8] (see Chapter 2) there are several options for the type of reactor model, depending on the number of phases used. In this work we use a heterogeneous model in which the temperatures of the fluid and solid are both solved for. The energy balance for the fluid can be expressed as [2, 8]:

$$\nabla\left(k_{\mathrm{eff}}\nabla T_f\right) - \left(\rho C_P\right)_f v_s \nabla T_f - h a_m\left(T_f - T_S\right) = \left(\rho C_P\right)_f \frac{dT_f}{dt} \tag{4.70}$$

The transient solid phase energy balance is:

$$\nabla\left(k_{\mathrm{eff}}\nabla T_S\right) - h a_m\left(T_f - T_S\right) + a_m\left(-\Delta H_R\right)\left(N_{\mathrm{CH_4}}\right)_4 = \left(\rho C_P\right)_S \frac{dT_S}{dt} \tag{4.71}$$

The effective thermal conductivities are selected according to direction and phase, with values computed using the methods of Hayes et al. [21]. In Equation (4.71), $\left(N_{\mathrm{CH_4}}\right)_4$ represents the mass flux at the gas solid interface. This value is extracted from the look-up table, discussed shortly. The heat transfer coefficient is calculated from the Nusselt number:

$$\mathrm{Nu} = \frac{h D_H}{k_f} \tag{4.72}$$

The Nusselt numbers was assigned a value of 4.0, as used in Chapter 2. Note that we have ignored surface to surface radiation in the monolith channels.

Following the methods developed in Chapter 2 (reference [8]) the effect of external mass transfer was included in the look-up table, and thus a single mass balance equation is used for each species in the fluid phase. The Sherwood number was set equal to the Nusselt number at 4.0

$$\phi \nabla \left(D_I \, \rho \nabla w_i \right) - \rho v_s \nabla w_i - a_m \left(N_i \right)_4 = \rho \frac{\partial w_i}{\partial t} \tag{4.73}$$

Diffusion is not allowed in the radial direction. In the axial direction, the diffusion can be approximated by the Taylor-Aris model for laminar flow [22], where:

$$D_I = D_{i,m} + \frac{\left(v_s \, D_H \right)^2}{\phi^2 \, 192 \, D_{i,m}} \tag{4.74}$$

The area to volume ratio for a monolith is calculated using the fractional open frontal area, or porosity, of the monolith structure and the hydraulic diameter of the channels.

$$a_m = \frac{4\phi}{D_H} \tag{17}$$

The chosen reaction was oxidation of methane with a Pt/ γAl_2O_3 catalyst, represented by the following overall reaction:

$$CH_4 + 2O_2 \rightarrow CO_2 + 2H_2O \tag{21}$$

The enthalpy change of reaction in J/mol is [16]:

$$\begin{aligned} \Delta H_R = {} & -8.025\times10^5 + 1.587T - 8.48\times10^{-3}T^2 \\ & - 4.087\times10^{-6}T^3 + 2.163\times10^{-9}T^4 \end{aligned} \tag{22}$$

Note that other physical properties had the same values as given in Chapter 3.

4.3.4 Boundary Conditions

For the flow boundary conditions, the velocity is specified at the inlet to the system. The inlet velocity was adjusted with changing temperature to maintain a constant mass flow rate. Dirichlet boundary conditions of specified temperature and species concentration were also imposed at the inlet. At the reactor outlet, pressure outlet boundary conditions were used for the flow.

The temperature boundary conditions imposed were convection conditions at the outside surface of the reactor. An imposed value of the heat transfer coefficient and surrounding temperature was used. For all surfaces a value of 10 W/(m^2K) was used, which is typical for natural convection, and the external temperature was 293 K. Zero flux conditions were imposed for the mass conservation equations at the external surfaces.

4.3.5 Development of the look-up tables

As mentioned, the reactor model was heterogeneous for the temperature and homogeneous for the concentration. To use this reactor model and retain all of the heat and mass transfer resistance terms, required the use of the look-up table referred to as T4 non-isothermal in Chapter 2. For each change in channel configuration, either cell density or wall thickness, the channel hydraulic diameter of the channel changes, as does the washcoat size and shape. Therefore it is necessary to build a look-up table for each monolith configuration. This was done using the procedure outlined in Chapter 2, with the same Deutschmann kinetic model for the oxidation of methane.

All monolith substrates were assumed to include 12 % by volume of washcoat. From this value of 12 %, the amount of washcoat in each channel can be computed for a given cell density, which can be expressed in terms of a washcoat frontal area (normal to the flow direction). For each washcoat geometry, a fillet shape washcoat was constructed that contained the appropriate surface area. The diffusion reaction equations were then solved for a one eighth section of the channel with the Deutschmann kinetics, and the average reaction rate in each case expressed as an average flux at the surface. These values were then used to construct the six look-up tables required. The complete procedure is given in Chapter 2.

4.3.6 Domain discretization

The unstructured finite element mesh used for the problem is shown in Figure 4.3. The total number of triangular elements was 3508. A fine grid was used near the wall to capture accurately the flow in that region.

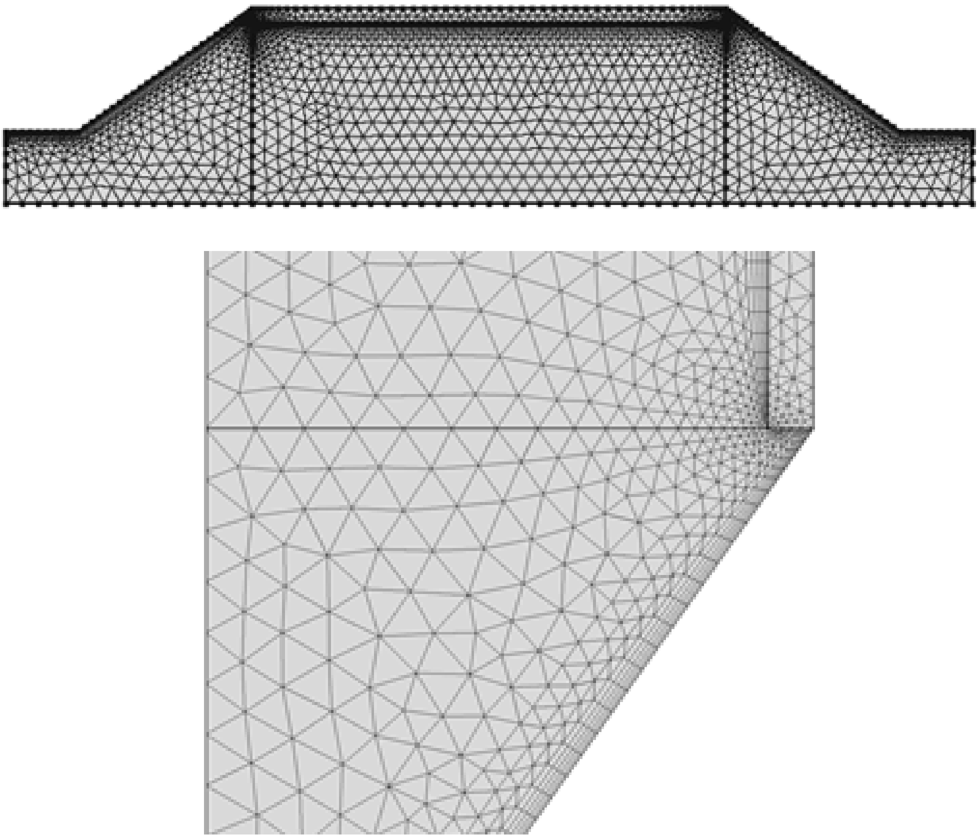

Figure 4.3 – Computational domain used for the simulation. Top: full domain and bottom: zoomed view of inlet region.

4.4 Equipment

The simulations were performed using COMSOL Multiphysics Version 4.3 on an Intel i7 3820 3.6 GHz with 10 MB L3 cache. This processor contains four cores, which can be efficiently used by COMSOL, effectively meaning parallel operation.

4.5 Results and discussion

Transient light-off simulations were performed for the six monolith configurations. The simulations started from an initial temperature of 300 K, and was then ramped linearly to 950 K at either 5 K/s or 20 K/s. The fluid velocity corresponded to a GHSV of 25,000 h^{-1} referenced at 300 K. The outlet temperature and fractional conversion of methane were monitored as a function of time.

Prior to presenting the light-off curves, we show a few illustrations of the temperature and velocity patterns. Figure 4.4 shows a zoomed picture of the velocity streamlines in the inlet diffuser for the 400 CPSI monolith with 6.5 mil walls at the inlet temperature. This flow pattern is typical [2, 7] and, although not evident from the picture, there is a recirculation zone present.

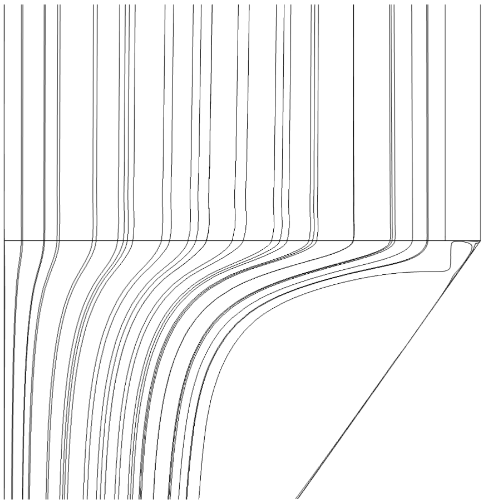

Figure 4.4 – Velocity streamlines of 400 CPSI/6.5 at 300 K.

Figure 4.5 shows the corresponding pressure distribution in the monolith, again at the initial temperature of 300 K.

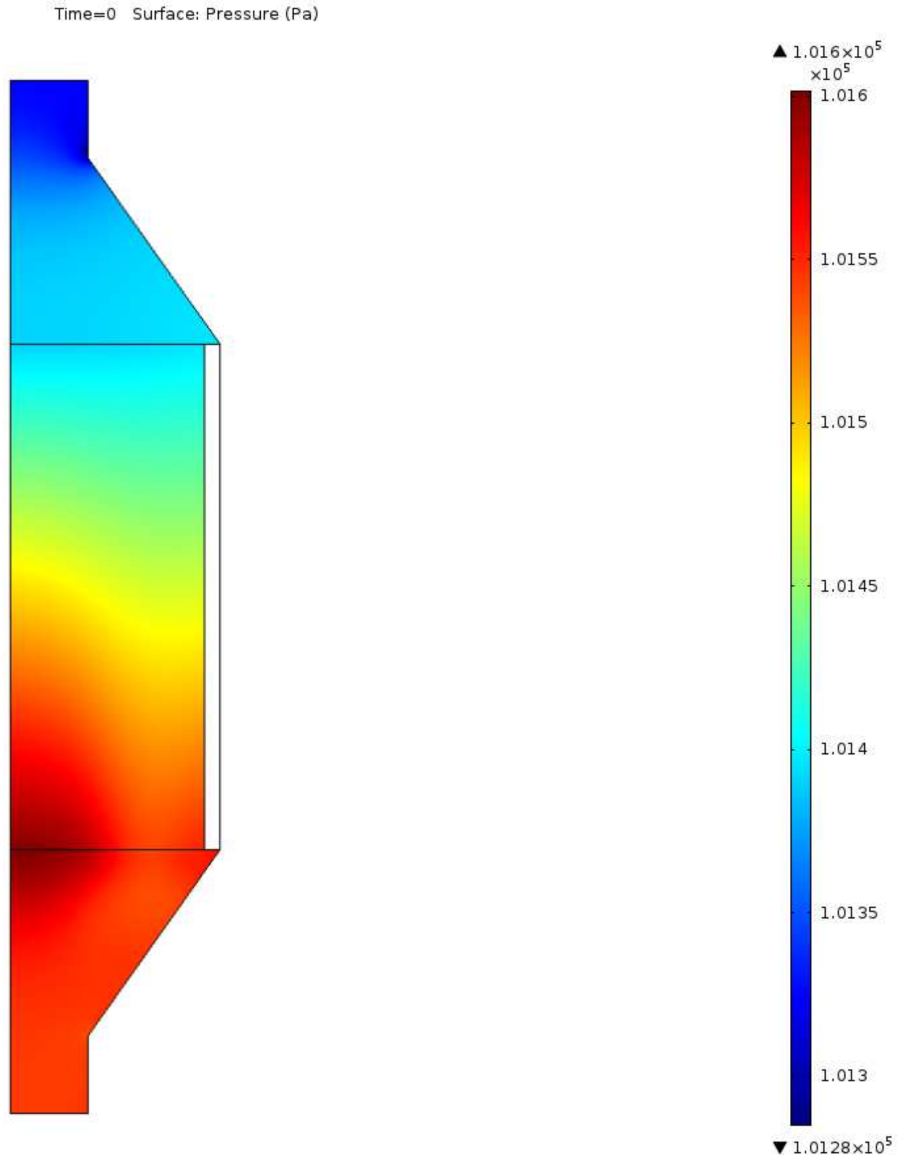

Figure 4.5 - Pressure distribution 400 CPSI/6.5 at 300 K.

Figure 4.6 shows the fluid temperature distribution after 8 s of heating at 20 K/s. It is seen that there is a higher temperature in the core of the reactor compared to the outer walls, due to the effect of the heat losses.

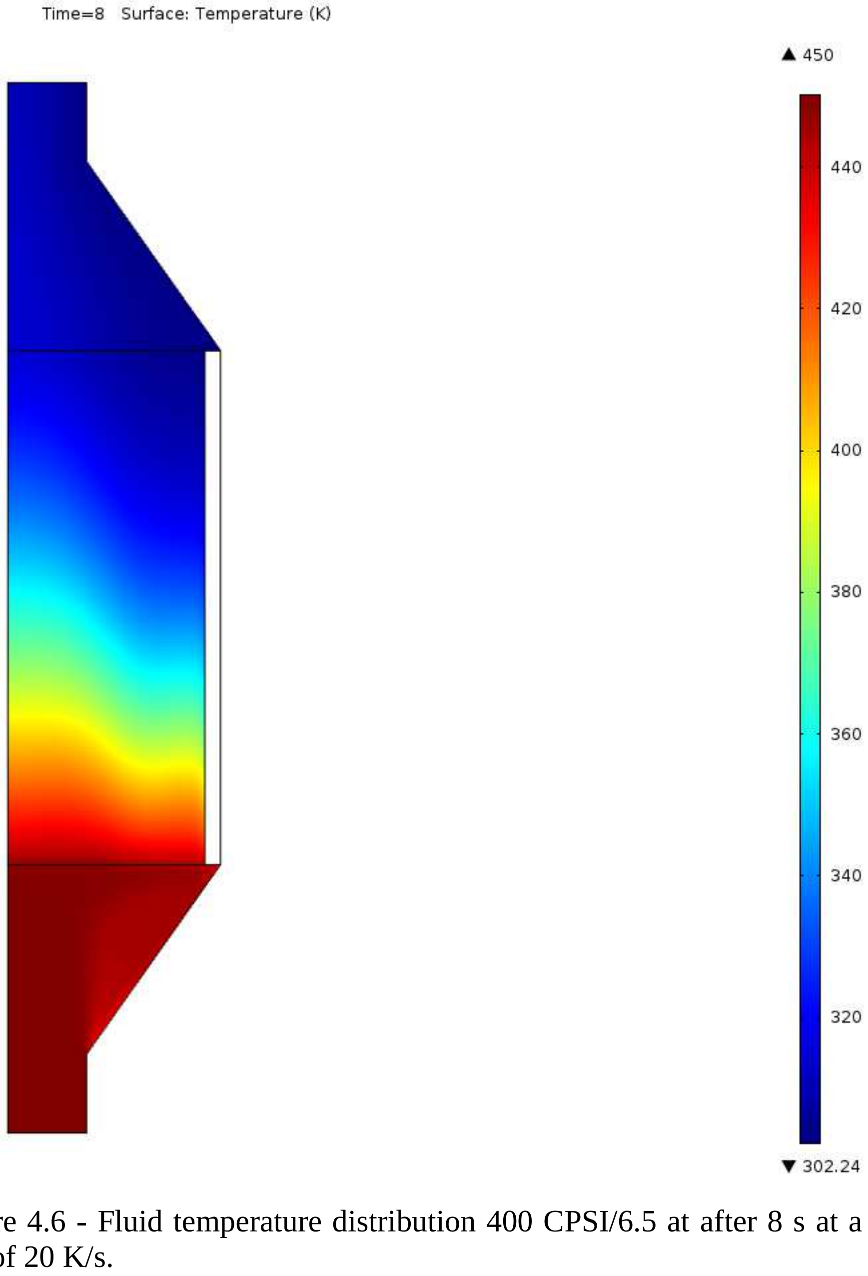

Figure 4.6 - Fluid temperature distribution 400 CPSI/6.5 at after 8 s at a heating rate of 20 K/s.

The light-off curves for the six different monolith configurations are shown in Figure 4.7 for the two ramp rates. For ramp rates it is found that the 900 CPSI/2.5 performs the best and that the 400 CPSI/6.5 performs the worst if the time taken to reach essentially complete conversion is used as the criterion. Note that the latter monolith is the standard format used in most catalytic converters today. The higher the temperature ramp rate, the larger the difference observed between the two monoliths.

Table 4.3 shows the inlet gas temperature that corresponds to 25, 50 and 75 % conversion at the outlet. These numbers make the comparisons clearer. The interesting point is that for the 25 and 50 % conversion levels, the 400/2.5 is the best performer.

Table 4.3 - Inlet temperature (°C) corresponding to three outlet conversion levels.

	A 400/6.5	B 400/4.3	C 600/4.3	D 400/2.5	E 600/3.5	F 900/2.5
25% Conversion						
5 K/s	541.6	537.8	538.3	533.4	536.3	534.7
20 K/s	171.2	169.0	169.0	166.1	168.0	166.6
50% Conversion						
5 K/s	574.9	570.6	570.2	565.8	568.4	565.9
20 K/s	181.2	178.5	178.3	175.2	177.1	175.4
75% Conversion						
5 K/s	607.2	601.9	599.8	596.3	598.3	594.4
20 K/s	190.8	187.5	186.9	183.7	185.5	183.6

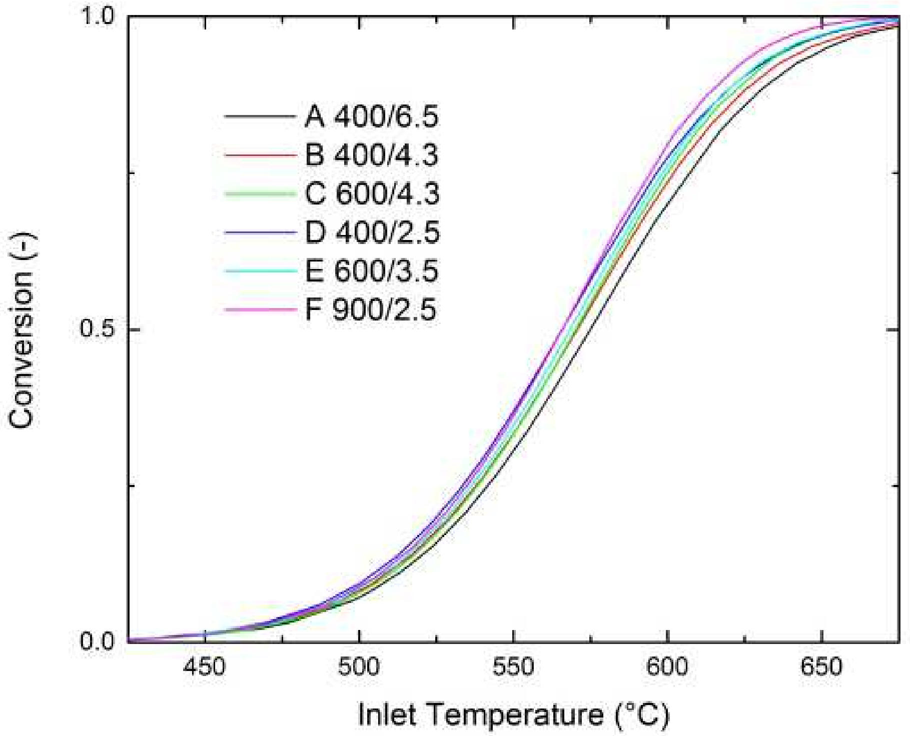

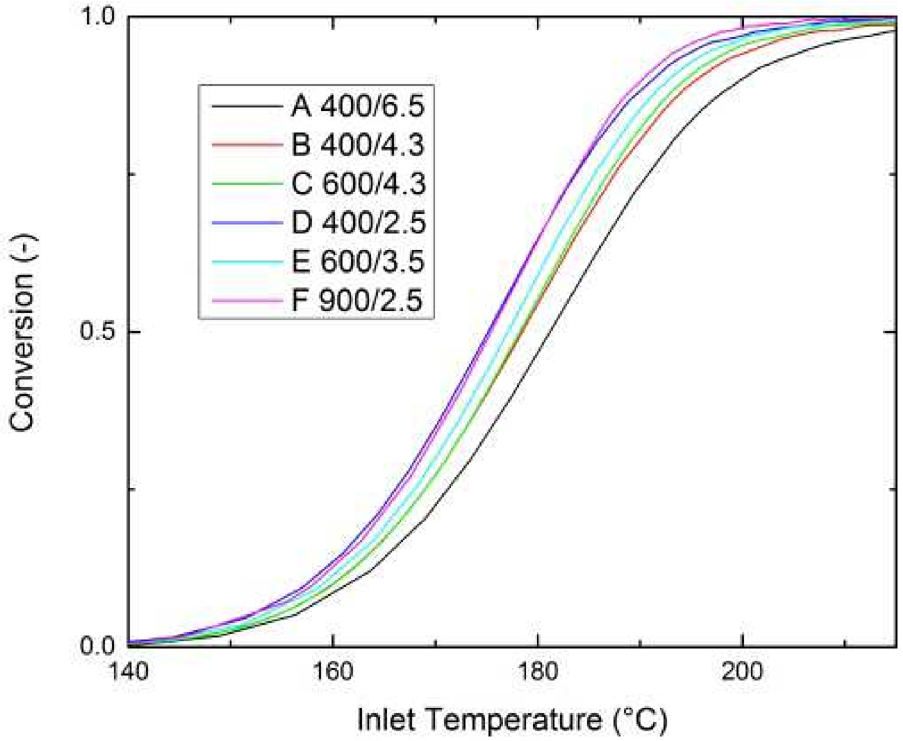

Figure 4.7 – Light-off curves for the six monolith configurations for 5 K/s (top) and 20 K/s (bottom).

Another useful performance measure is the total amount of methane released during the entire warm-up period. This amount can be computed by integrating the effluent concentration over time, using the following formula:

$$m_{CH_4} = \dot{m}_{tot} \int_{t_0}^{t_f} \left(1 - w_{CH_4}\right) dt \tag{4.75}$$

The results for this calculation can be found in Table 4.4. It is seen that the lowest emission is achieved with the 900/2.5, emitting 0.562 g and 2.032 g of methane for 20 K/s and 5 K/s ramp respectively. However, at the same time, it is the one that produces the highest pressure drop. The performance in terms of conversion of the 400/2.5 does not differ considerably from the 900/2.5, although it produces the lowest pressure drop.

Table 4.4 Total emissions and pressure drops for different cell densities.

	A 400/6.5	B 400/4.3	C 600/4.3	D 400/2.5	E 600/3.5	F 900/2.5
	Methane emissions (g)					
20 K/s	0.595	0.584	0.576	0.569	0.571	0.562
5 K/s	2.074	2.058	2.051	2.039	2.044	2.032
	Pressure drop (Pa)					
	1359	1113	1726	960	1576	2164

4.6 Conclusions

In this chapter we have seen that the use of a hierarchical multi-scale model reduction can be applied to a catalytic converter, which allows a consistent comparison of various substrate configurations. Complex kinetics and small scale heat and mass transfer phenomena can be incorporated using an appropriate look-up table. The case study presented here demonstrates the versatility and usefulness of this approach.

For the comparisons of cell density and wall thickness presented here for this reaction, it is seen that although the 900/2.5 performs the best from an overall emissions perspective, the 400/2.5 is nearly as good, while offering a much lower back pressure. Considering the huge price that is paid in fuel economy as a result of even small increases in back pressure, this is a worthwhile result.

The differences in overall emissions observed for this test case are small, although even small differences can be important. It is know that the light-off is especially important in current gasoline engines using three way catalysts, and the extension of this work to that case should prove worthwhile, especially now that the tools are available to do the job.

Nomenclature

a_m	Surface area per unit volume, m^2/m^3
C_P	Constant pressure heat capacity, $J/kg \cdot K$
D	Diameter of monolith, m
DP	Diameter of inlet pipe, m
D_H	Hydraulic diameter, m
D_I	Effective axial diffusivity in fluid, m^2/s
$D_{i,m}$	Diffusivity of species *i* in the mixture, m^2/s
D_t	Effective dispersion coefficient, m^2/s
h	Heat transfer coefficient, W/m^2K
(ΔH_R°)	Standard heat of reaction, species *i*, J/mol
k	Turbulent kinetic energy
k	Thermal conductivity, $W/m \cdot K$
k	Turbulent kinetic energy, J
k_{eff}	Effective thermal conductivity of monolith and fluid, $W/m \cdot K$
k_t	Effective turbulent thermal conductivity of fluid, $W/m \cdot K$
$\mathbf{K}$	Permeability, m^2
L	Monolith length, m
LP	Length of inlet pipe, m
L_C	Characteristic length, m
M	Molar mass of a substance, g/mol
Nu	Nusselt number
p	Pressure, Pa
Pr	Prandtl number
R_g	Gas constant, $J/(mol \cdot K)$
Sc	Schmidt number
t	Time, s

T	Temperature, K
v	Velocity, m/s
v_S	Superficial velocity, m/s
w	Mass fraction
w	Insulation thickness, m

Greek Symbols

ρ	Density, $\mathrm{kg/m^3}$
ε	Turbulent kinetic energy dissipation rate
τ	Stress tensor
μ	Viscosity, Pa·s
ω	Turbulence frequency
μ_t	Turbulent viscosity, Pa·s
ϕ	Monolith porosity
θ	Angle, degrees

Subscripts

f	Fluid
i	Species
S	Solid, surface or superficial
t	Turbulent

References

[1] R.E. Hayes, S.T. Kolaczkowski, W.J. Thomas, Computers & Chemical Engineering. 16 (1992) 645–657.

[2] R.E. Hayes, A. Fadic, J. Mmbaga, A. Najafi, Catalysis Today. 188 (2012) 94–105.

[3] F. Bertrand, C. Devals, D. Vidal, C.S. de Préval, R.E. Hayes, Catalysis Today. 188 (2012) 80–86.

[4] K. Zygourakis, Chemical Engineering Science, 44 (1989) 2075.

[5] M. Luoma, A. G. Smith, PHOENICS Journal of CFD and its applications, 9 (1996) 76.

[6] S. Tischer and O. Deutschmann, Catalysis Today 105 (2005) 407.

[7] J. Braun, T. Hauber, H. Tobben, J. Windmann, P. Zacke, D. Chatterjee, C. Correa, O. Deutschmann, L. Maier, S. Tischer and J. Warnatz, SAE Paper 2002-01-0065 (2002)

[8] T. Nien, J.P. Mmbaga, R.E. Hayes, M. Votsmeier, Chemical Engineering Science. 93 (2013) 362–375.

[9] K. Eads and K. Haghighi, SAE paper 2001-01-0636.

[10] K. Oouchi, K. Shibata, K. Nishizawa and H. Tanabe, SAE Paper 2002-01-0358.

[11] K.W. Hughes, D. Gian and J. Calleja, SAE Paper 2006-01-1065

[12] S.T. Gulati, SAE Paper 1999-01-0269.

[13] Y. Aoki, Y. Miyairi, Y. Ichikawa and F. Abe, SAE Paper 2002-01-0350.

[14] R.E. Hayes and S.T. Kolaczkowski, Chemical Engineering Science, 49 (1994) 3587.

[15] D. Leung, R.E. Hayes and S.T. Kolaczkowski, Canadian Journal of Chemical Engineering, 74 (1996) 94-103.

[16] R.E. Hayes, S.T. Kolaczkowski, Introduction to catalytic combustion, Gordon and Breach Science Publishers, Reading, UK. (1997)

[17] H. Lun, N. Xiaowei, Z. Liang, L. Yongping, Z. He, H. Wei, International Journal of Chemical Reactor Engineering, 8 (2010) Article A37.

[18] S.E. Voltz, C. R. Morgan, D. Liederman, S. M. Jacob, Ind. Eng. Chem. Prod. Res. Dev., 12 (1973) 294.

[19] A. Holmgren, T. Gronstedt, B. Andersson, React. Kinet. Catal. Lett., 60 (1997) 363.

[20] B. Liu, R.E Hayes, J. Mmbaga, Y. Yi, M.D. Checkel and M. Zheng, Computers and Chemical Engineering, 31 (2007) 292–306.

[21] R.E. Hayes, A. Rojas, J.P. Mmbaga, . The effective thermal conductivity of monolith honeycomb structures. Catalysis Today 147 (2009) S113–S119.

[22] R. Aris, Proceedings of the Royal Society A: Mathematical, Physical and Engineering Sciences. 235 (1956) 67–77.

Chapter 5:
Modelling of a Gauze Reactor for Ammonia Oxidation

Overview

This chapter describes the development of a computational model for a gauze type structured reactor as used for the partial oxidation of ammonia to produce NO. Complete parametric studies are reported for both two and three dimensional cases of single and multiple wires. Particular emphasis is placed on an investigation of the selectivity of the reaction for NO (desired) and N_2O (undesired). A mechanistic model is used to describe the kinetics, with both the model and parameter values for the rate constants taken from the literature. A look-up table was used to enable the parametric studies to be performed in reasonable amounts of time.

It is seen that the selectivity depends not only on the temperature, but also strongly on the geometry. The selectivity varies around the perimeter of each wire and, in the case of multiple wire simulations, from wire to wire.

This chapter is a modified version of the paper --- A. Donoso-Bravo, T. Nien, J.P. Mmbaga, R.E. Hayes and M. Votsmeier, CFD Modelling of a Gauze Reactor for Ammonia Oxidation, to be submitted

5.1 Introduction

It has become increasingly recognized over the past few decades that reactor technology offers solutions to many environmental problems relating to undesired emissions from various sources, including automobiles and chemical process plants. In emission reduction applications, stringent government regulations are usually the primary driver, and very good control of the effluent composition must be maintained.

Renewed interest on *process intensification* has led to an increase in use of structured reactors. A structured reactor contains a structured internal inside of it. One key advantage of this type is that the internal may be designed in detail, including the hydrodynamic environment surrounding the catalyst, and the final configuration is achieved by design, rather than happenstance. A good knowledge of the hydrodynamic and transport parameters is the key to a good structured reactor design, as is an understanding of the reaction kinetics. Examples of structured reactors include monoliths, extensively used in automotive exhaust applications (Heck and Farrauto, 2009) and gauze reactors, used in such key industrial applications as the synthesis of HCN (Andrussow process) and the oxidation of ammonia (Ostwald process).

The catalytic oxidation of ammonia over platinum or platinum-rhodium catalysts is a crucial reaction for both the manufacture of nitric acid, and in the catalytic exhaust gas after treatment systems for lean burn engines (e.g. with Diesel and natural gas fuels). Focusing on the first application, the oxidation of NH_3 to NO is typically carried out industrially using a gauze type catalyst, which is composed of an alloy of platinum and rhodium. The reason for this design is the desire to have relatively short contact times between the reactant stream and the catalyst. The reactor feed is typically of the order of 10 % ammonia in air, which is passed over multiple gauze layers (between 10 and 50) that form a bed a few millimetres in thickness (Hickman and Schmidt, 1991). The reactor diameter is usually quite large, with sizes up to several metres being used. The reaction is highly exothermic. The feed enters at approximately 400 K, and the catalyst surface temperature is maintained around 1200 K as a result of the extreme exothermicity of the reaction. This process has been used for a relatively long time. In recent years, more sophisticated woven gauze designs have been proposed by, for example, Katator and Microlith. These designs have been studied by various researchers (Ahlstrom-Silversand and Odenbrand, 1999; Lyubvsky, et al., 2003). Knitted gauzes have also been reported (Hills et al., 2005).

Nitrous oxide is a byproduct of the ammonia oxidation process. N_2O has historically been considered harmless, and emission regulations for it have been low to non-existent. However, recent attention to global warming and ozone depletion has led to an interest in this gas. N_2O has a global warming potential 310 times that of CO_2, and contributes about 6% of the planet’s greenhouse gas emissions (Pérez-Raḿırez, et al., 2003). It also leads to formation of NO in the upper atmosphere. Currently, to minimize emissions of N_2O from ammonia oxidation reactors, an auxiliary catalyst may be added after the gauze layers (Kopperud, 2006). This catalyst is often in the form of pellets or Rashig rings. There is currently great interest in this process, because significant greenhouse gas emission credits can be claimed for N_2O abatement.

Because the reaction is extremely exothermic, heat and mass transfer limitation plays a significant role at higher temperatures and pressures. As a result, most mechanistic studies have been conducted under ultrahigh vacuum (UHV) conditions and primarily on single crystals. These model catalysts provide much needed insight, although it has to be appreciated that a complex restructuring of the catalyst surface occurs under industrial operating conditions. The reaction has been studied by research groups with expertise covering a wide range of fields, including chemical engineering, surface physics and quantum chemistry. In addition to the aforementioned model catalysts, studies have been performed on wires, foils and supported catalysts. Imbihl et al. (2007) provided an in-depth comprehensive investigation of this reaction over a variety of catalysts, and have presented one of the more detailed works over a variety of temperature and pressure ranges. They used a UHV system, a TAP reactor, as well as a small micro-structured reactor for the higher pressures. They have noted that the mechanism does not change significantly over the pressure range of UHV to high pressure. The exception is the formation of N_2O, which is relatively insignificant at low pressure. Thus N_2O is formed in very small quantities in ultrahigh vacuum conditions, where many mechanistic studies are performed. It has been suggested that N_2O formation results from secondary NO reactions, that is, NO is the primary oxidation product, which is then further reacted to N_2O. Isotopic labelling studies have indicated that two different reaction pathways exist for N_2O formation. The first is the reaction between two NO molecules, whilst the second is the reaction between an NO molecule and an NHx fragment. The reaction between adsorbed N atoms and adsorbed NO was concluded not to be very significant (Kondratenko and Baerns, 2007).

Knowledge of mechanisms usually enhances the ability to build representative kinetic models. At the most fundamental level, the mechanism is used to develop the micro-kinetic models. Micro-kinetic modelling is a technique that represents the reaction mechanism as a function of elementary steps (Dumesic, et al., 1993; Broadbelt and Snurr, 2000). Generally, one would expect micro-kinetic models to be more generally applicable than the common lumped kinetic models, although care should still be exercised in extrapolation. Recent modelling studies using mechanistic micro-kinetic models for the ammonia oxidation reaction can be found (Votsmeier et al., 2010; Scheuer et al., 2011).

For the most part, modelling studies on gauze type reactors have relied on plug flow type continuum models (Hickman and Schmidt, 1991; Waletzko and Schmidt, 1988). There have recently been a number of publications that have reported on pressure drop studies for different gauze types. Usually they result in an equation similar in form to the classical Ergun equation for packed beds (Kolodziej et al., 2009; Kolodziej and Lojeswka, 2008, 2009). Kolodziej et al. (2012) also studied flow and heat transfer around wire gauzes. However, studies of the flow patterns around gauzes with surface reaction are lacking in the literature.

Computational fluid dynamics (CFD) as an area of research and as an investigative tool has been around for many years. Originally it applied to fluid flow modelling, but now encompasses all transport processes, including momentum, energy and mass balances. With each passing year, techniques and computer power improve, giving this tool more power to reveal and understand fundamental processes. The modelling of chemical reactors has also been done using this method in recent years, and indeed there are now reference books on the topic (e.g. Ranade, 2001). There are many approaches used in CFD modelling, which reflect the multi-scale nature of the reactor problem. The use of a fully spatially discretized CFD model allows the computation of flow, temperature and concentration in boundary layers near the fluid solid interface without resorting to the use of mass and heat transfer coefficients. This level of discretization is not always practicable, and sometimes, lumped models based on volume averaging or continuum approaches are used. Regardless, formal CFD approaches allow for the more realistic inclusion of fundamental information, which in turn should give a more realistic understanding of the reactor (Dixon et al., 2006; Dixon et al., 2010; Behnam et al., 2010). In one study of note, CFD was used to investigate flow patterns and temperature profiles around a wire gauze for the catalytic partial oxidation (CPO) of methane (Quiceno et al., 2007).

There are many spatial scales present in the reactor, ranging from the molecular to the full size reactor scale, which may be of the order of microns to metres. Larger scale issues, such as hydrodynamics, can be modelled using computational fluid dynamics (CFD), as mentioned above. The integration of micro-kinetic analysis with computational fluid dynamics in a computationally efficient way requires new computing paradigms. The proposed solution to the computing conundrum is to use the solution mapping technique recently reported in the simulation of automotive catalytic converters (Nien et al., 2013). In this method, we pre-compute the reaction rates over some defined solution space, and store the result in an efficient manner in a look-up table. The defined space covers all expected combinations of temperature and concentrations encountered in the reactor simulation. During the execution, the look-up table is simply accessed for the solution. Although the look-up table can be expensive to build, once built it can be used for many applications, provided that a sufficiently broad range of parameters is selected. We use multivariate spline functions to represent the rate data on a regular multi-dimensional grid (Votsmeier, 2009). Multi-dimensional splines can be efficiently evaluated if the coefficients of the individual polynomials are pre-computed and stored in a database. The use of these look-up tables for ammonia oxidation has been reported in the context of the ammonia slip catalyst following a selective catalytic reduction (SCR) reactor for automotive applications (Votsmeier et al., 2010; Scheuer et al., 2011).

5.2 Mathematical Model

The mathematical model must consider the relevant transport (conservation) equations, which include source terms to account for the appropriate chemical reactions. We show the simplest solution domain for reference purposes, a single wire immersed in fluid in two dimensions, see Figure 5.1.

To build this geometry we use symmetry to consider one half of the wire, represented by the semi-circle. The area within the semi-circle represents the solid wire, and the remainder is the flow domain. The fluid enters from the left and exits from the right. The top and bottom boundaries (except for the wire surface) represent symmetry boundaries. The chemical reaction occurs on the surface of the wire. We now consider the relevant mathematical formulation required to solve the problem.

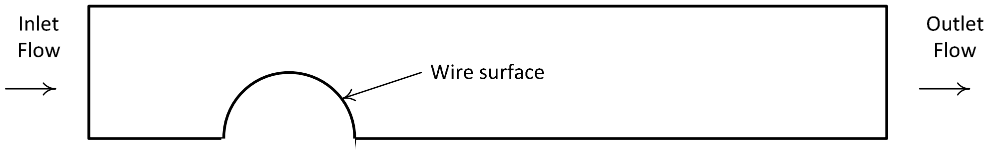

Figure 5.1 – Representative domain for a single wire in a flow, 2D representation.

5.2.1 Transport equations

The transport model must deal with the momentum balance in the fluid phase, the energy balance in both the fluid and the solid wire, and the mass transport in the fluid. The momentum balance equation used was the Navier-Stokes equation, which is appropriate for the laminar flow regime present (Kolodziej et al., 2012). The steady state equations are:

$$\rho(u \cdot \nabla)u = \nabla \cdot \left[-\rho I + \mu\left(\nabla u + (\nabla u)^T\right) - \frac{2}{3}\mu(\nabla \cdot u) I \right] \tag{5.76}$$

$$\nabla \cdot (\rho u) = 0 \tag{5.77}$$

For the boundary conditions, at the inlet, a flat velocity profile was imposed, and the outlet used standard outlet boundary conditions. The top and the bottom used symmetry conditions, whilst a zero velocity (no-slip) was imposed at the wire surface.

The viscosity of each gas was computed using a temperature dependent polynomial based on data from Perry and Green (1984):

$$\mu = a_\mu + b_\mu T + c_\mu T^2 \tag{5.78}$$

The coefficients used are given in Table 5.1. The mixture viscosity was then calculated using a weighted average based on the mole fraction of each component. Although this is an approximation, it was felt sufficient, as most of the mixture is nitrogen. The fluid density is given by the ideal gas law.

The energy balance must be completed for both the fluid and the wire. The conservation of energy for the fluid phase is represented by the advection-diffusion equation, viz:

$$\nabla \cdot (k \nabla T) - \rho\, C_P\, u \cdot \nabla T = 0 \tag{5.79}$$

The heat capacity of each species was computed using a fifth order polynomial. The mixture heat capacity was computed as a weighted molar average of the components present.

$$C_P = a_c + b_c T + c_c T^2 + d_c T^3 + e_c T^4 \tag{5.80}$$

The coefficients for the species are given in Table 5.2 (Hayes and Mmbaga, 2012):

The thermal conductivity of the gases were expressed as temperature dependent polynomials using data from Perry and Green (1984):

$$k_i = a_k + b_k T + c_k T^2 + d_k T^3 \tag{5.81}$$

The coefficients in the polynomial are given in Table 5.3 . The thermal conductivity of the mixture was computed using a weighted average of the components based on the mole fractions of each component.

In the wire, heat is transferred by conduction alone, according to:

$$\nabla \cdot (k \nabla T) = 0 \tag{5.82}$$

The thermal conductivity of platinum used was a constant value of 71.6 W/(m·K). The temperature gradients in the platinum were found to be very small, and the wire has a nearly uniform temperature, therefore it is not necessary to use a more complicated expression.

The interface between the fluid and the solid formed by the surface of the wire is an internal boundary within the system. In essence the domain is continuous, and thus we do not impose boundary conditions as such on it. Therefore, to incorporate the thermal energy generated by the reaction, and the heat transferred from the surface by radiation, we impose a source term along the boundary.

Table 5.1 – Coefficients used in the viscosity polynomial.

Species	$a_\mu \times 10^6$	$b_\mu \times 10^8$	$c_\mu \times 10^{12}$
NH_3	-0.7874	3.67	-0.447
NO	3.9921	5.37	-12.4
O_2	4.4224	5.62	-11.3
N_2	4.2606	4.75	-9.88
H_2O	-3.682	4.29	-1.62
N_2O	3.228	4.454	-7.708

Table 5.2 – Coefficients used in the heat capacity polynomial.

Species	a_c	$b_c \times 100$	$c_c \times 10^5$	$d_c \times 10^8$	$e_c \times 10^{12}$
NH_3	33.573	-1.2581	8.8906	-7.1783	18.569
NO	33.227	-2.3626	5.3156	-3.7858	9.1197
O_2	29.526	-0.88999	3.8083	-3.26259	8.8607
N_2	29.342	-0.35395	1.0076	-0.43116	0.25935
H_2O	33.933	-00.84186	2.9906	-1.7825	3.6934
N_2O	51.05957	-5.121764	11.5374	-8.874911	23.46661

Table 5.3 – Coefficients used in the thermal conductivity polynomial

Species	$a_k \times 10^3$	$b_k \times 10^5$	$c_k \times 10^7$	$d_k \times 10^{12}$
NH_3	4.57	2.3239	1.481	0
NO	1.76	8.2369	-0.12527	0
O_2	1.21	8.6157	-0.13346	0
N_2	3.09	7.593	-0.11014	0
H_2O	0.53	4.7093	0.49551	0
N_2O	-7.835	8.903	-0.0897	-2.668

Table 5.4 – Coefficients used in the enthalpy of reaction polynomial.

Reaction	A	B	$C \times 10^2$	$D \times 10^6$	$E \times 10^9$
NO	-230 598	18.251	-2.13	2.2403	-1.1303
N_2	-398 441	16.106	-0.174	5.13	-0.28
N_2O	-274 309	7.356	-4.315	-1.572	1.317

The first part of the source term arises from the enthalpy change of reaction. The general global reactions that take place on the wire surface given in the following. Nitric acid (NO) is the target product, however, undesired products, N_2 and N_2O, are also produced.

$$4\,NH_3 + 5O_2 \longrightarrow 4\,NO + 6\,H_2O \tag{5.83}$$

$$4\,NH_3 + 3O_2 \longrightarrow 2\,N_2 + 6\,H_2O \tag{5.84}$$

$$4\,NH_3 + 4O_2 \longrightarrow 2\,N_2O + 6\,H_2O \tag{5.85}$$

The enthalpy of reaction for each of the reactions was expressed as a temperature dependent equation, calculated from the enthalpy of formation and the heat capacity data, and was based on a reference of one mole of NH_3 reacted, with the result expressed in J (Hayes and Mmbaga, 2012). The general expression is:

$$\left(\Delta H^{0}{}_{R}\right)_{i} = A + BT + CT^{2} + DT^{3} + ET^{4} \tag{5.86}$$

The coefficients are given in Table 5.4.

Radiation from the surface to the surroundings was modelled, while gases were assumed to be transparent to radiation, i.e. no gas absorption. Radiation between the convex surfaces (for the case of multiple wires, discussed shortly) was also captured by this model. The methodology for the radiation calculation is the same as used by Amiri et al. (2013). It was found that the effect of radiation was to lower the surface wire temperature by about 50 to 60 Kelvin, and thus it is important to include it.

At the inlet to the system a Dirichlet boundary condition of constant temperature was used, whilst at the outlet a zero temperature gradient was imposed, standard Neumann outlet condition.

For the mass conservation, we only need to consider the fluid phase. The species transport equations are given by:

$$\nabla \cdot \left(\rho D_i^m \nabla w_i \right) + \rho (u \cdot \nabla) w_i = 0 \tag{5.87}$$

The diffusion coefficient of the species in the mixture is then computed from the binary diffusion coefficients (Taylor and Krishna, 1993):

$$D_i^m = \frac{1 - w_i}{\sum_{k \neq i} \frac{x_k}{D_{ik}}} \tag{5.88}$$

The binary diffusion coefficients were computed using the equation of Fuller et al. (1966):

$$D_{ij} = \frac{1.013 \cdot 10^{-2} \cdot T^{1.75} \sqrt{{}^{1}\!/\!{}_{M_i} + {}^{1}\!/\!{}_{M_j}}}{P(\sum \nu_i^{1/3} + \sum \nu_j^{1/3})^2} \tag{5.89}$$

Where T is the temperature in K, P is the pressure in Pascal, M is the molar mass of the species i and j and ν is the diffusion volume of each species.

The boundary conditions for the mass balance equation are as follows. For the lines of symmetry, a zero normal flux was imposed. A zero concentration gradient was imposed at the outlet (outflow condition). At the inlet a constant inlet concentration was imposed (Dirichlet condition). At the wire surface, the rate of diffusion is set equal to the rate of reaction. For species i,

$$\rho D_i^m \frac{\partial w_i}{\partial n} = (-R_i) \tag{5.90}$$

The rate in this equation has units of kg/(m^{2}s).

5.2.2 Kinetic model

The kinetic model used was a multi-step mechanism reported earlier (Votsmeier, et al., 2010; Scheuer, et al., 2011). This reaction mechanism used was based on the work of Krahnert and Baerns (2008), and a complete description can be found in Scheuer et al. (2009). It is summarized in Table 5.5 and the parameter values used can be found in Table 5.6. These values are also taken from Scheuer et al. (2009). These parameters represent a reference activity level, which was adjusted to illustrate the effect of catalyst activity on the conversion and reactor selectivity. It is well known that the activity of the catalyst changes with operating time on stream. For example, "cauliflower" type nodules have been found to appear in the Pt wire reconstruction process, which may increase the reaction rate through an increase in apparent surface area. (Nilsen et al., 2001; Hannevold et al., 2005)).

Table 5.5 - The reaction mechanism for ammonia oxidation reaction. This mechanism uses two different adsorption sites, a and b (from Scheuer et al. (2009).

Reaction number	Reaction description	Reaction
R1	NH_3 adsorption	$NH_3 + b \rightarrow NH_3\text{-}b$
R2	NH_3 desorption	$NH_3\text{-}b \rightarrow NH_3 + b$
R3	O_2 adsorption	$O_2 + 2a \rightarrow 2O\text{-}a$
R4	O_2 desorption	$2O\text{-}a \rightarrow O_2 + 2a$
R5	NH_3 activation	$NH_3\text{-}b + 1.5O\text{-}a \rightarrow N\text{-}a + 1.5H_2O + 0.5a + b$
R6	NO desorption	$NO\text{-}a \rightarrow NO + a$
R7	NO adsorption	$NO + a \rightarrow NO\text{-}a$
R8	N_2 formation	$2N\text{-}a \rightarrow N_2 + 2a$
R9	NO formation	$N\text{-}a + O\text{-}a \rightarrow NO\text{-}a + a$
R10	N_2O formation	$NO\text{-}a + N\text{-}a \rightarrow N_2O + 2a$

Table 5.6 – Parameters used in the rate expressions comprising the mechanism. (from Scheuer et al. (2009).

Reaction number	Reaction description	k_0, $m^3/(s \cdot mol)$ for R1, R2 and R7, s^{-1} otherwise	*E*, kJ/mol
R1	NH_3 adsorption	3.3×10^2	0
R2	NH_3 desorption	1×10^{10}	70.9
R3	O_2 adsorption	3.1×10^4	0
R4	O_2 desorption	8.8×10^6	199.4
R5	NH_3 activation	1.7×10^{16}	122.9
R6	NO desorption	1.6×10^{17}	105.3
R7	NO adsorption	2.9×10^4	0
R8	N_2 formation	8×10^{19}	164.9
R9	NO formation	5.2×10^{14}	118.5
R10	N_2O formation	1.5×10^{22}	145.9

5.2.3 Selectivity

To evaluate the system performance in terms of ammonia conversion and product generation, the selectivity on the surface wire is calculated. The local selectivity at any point on the wire surface is calculated using the reaction rates:

$$S = 2 \cdot \frac{r_{N_2O}}{\left(-r_{NH_3}\right)} \tag{5.91}$$

The overall selectivity at the system outlet is based on the concentration of the desired component relative to the total amount of NH_3 consumed. Thus the selectivity for nitrous oxide is:

$$S = 2 \cdot \frac{\left(w_{\mathrm{N_2O}}\right)_{\mathrm{outlet}}}{\left(w_{\mathrm{NH_3}}\right)_{\mathrm{inlet}} - \left(w_{\mathrm{NH_3}}\right)_{\mathrm{outlet}}} \tag{5.92}$$

5.2.4 Operating conditions

The operating conditions selected are summarized here. The inlet fluid velocity was imposed as flat profile with a value of 1.5 m/s. The inlet temperature was 423 K. The inlet gas was composed of 10 mole percent ammonia and 20 mole percent oxygen, with the remainder nitrogen. The operating pressure was maintained at five atmospheres at the inlet. To start a simulation, the initial temperature of the solution domain was set at 900 K.

5.2.5 Model methodology and software

Simulations were performed using COMSOL Multiphysics 4.3a. The computer used had an Intel quadcore i7 processor and 64 GB of RAM. The reaction source terms for the three reactions, based on the mechanism, were computed using the Umicore chemistry module, a proprietary software package that performs the same function as the Cantera package used in Chapters 2-4 for the methane oxidation. The interface between the chemistry module and COMSOL was built using Matlab. The calls to the chemistry module were replaced by calls to the look-up table when the latter was used. The look-up table development is described in the following section.

5.2.6 Development of the look-up tables

The inclusion of detailed multi-step microkinetic models in CFD simulations results in a model that is computationally expensive to solve. To alleviate this issue, a solution mapping procedure was used. This approach consists of the pre-computation of the reaction rates over the desired solution space, and the consequent storage of the result in a so-called look-up table. Multivariate spline functions to represent the rate data on a regular multi-dimensional grid were used, using a similar methodology as developed in Chapter 2 for methane oxidation

(Votsmeier, 2009; Nien et al,, 2013; Scheuer, et al., 2011). Look-up tables were built with the help of Matlab and the Umicore chemistry module. The look-up table has four dimensions, for temperature and the concentrations of NH_3, NO and O_2. As done in Chapter 2, linear, quadratic and cubic splines were tested and compared. Figure 5.2 shows the error propagation as the size of the look-up table increases. For a final size of (33,33,33,9) the error was deemed acceptable (about 0.3 % for both quadratic and cubic splines) this table was used in all subsequent simulations. Quadratic spines were used in all cases. The size of the look-up table was 517 MB for quadratic splines and 1275 MB for the cubic splines.

The speedup given by the use of the look-up table can be measured in several ways, and depends on many factors. These include the method of passing information among the modules comprising the simulator, as well as the actual execution time to extract data from either the chemistry module or the look-up table. The comparison of the chemistry module to the look-up table shows the best speed up factor. To execute 100 sets of conditions using the look-up table requires 0.022 milliseconds, whilst it required about 934 milliseconds for the chemistry module. The chemistry module was stored on a Ramdisc to minimize execution time. For 10,000 sets of conditions, the respective times were 0.73 milliseconds and 51 seconds. This huge difference in execution time is not reflected in the speedup of the simulation, however. The observed speedup factor depends on the amount of time spent in the rest of the calculations. For 2D simulations the observed speedup factor was in the range 60 to 100. For the 3D simulations, the speedup factor was larger, but no reliable numbers are available owing to the length of time required to perform a 3D simulation with the chemistry module.

A comparison of solutions with the look-up table and the chemistry module will be shown shortly.

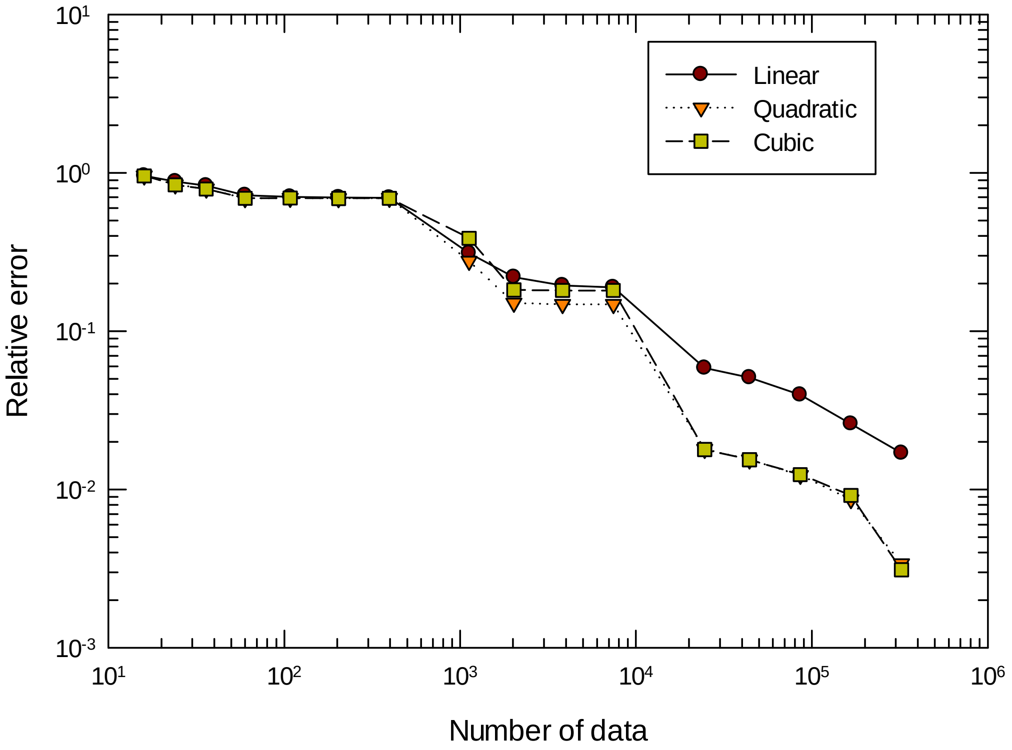

Figure 5.2 - The relative error vs. the number of pre-computed data for the lookup table of the ammonia reaction rate.

5.3 Results and Discussion

The investigation of the system was performed in a stepwise fashion. In the first instance, a single wire in two dimensions was studied, with the geometry shown in Figure 5.1. The next step was to investigate two sets of five wires in two dimensions, with a comparison of staggered and inline geometries being compared. In the final investigation, a three dimensional geometry was used, with both a single gauze and then multiple gauzes being investigated. The results are presented here for these cases.

5.3.1 2D single wire parametric study

The first set of simulations was performed using a single wire. This geometry was selected as being the simplest, and was therefore used in the model development process. The model was first developed in COMSOL using simple first order arbitrary kinetics to establish such things as convergence criteria, numerical stability etc. These results are not presented here. Once a methodology had been developed that was numerically stable, the mechanistic ammonia oxidation kinetic model was implemented. Initial tests were performed using the Umicore chemistry model and the look-up table to compare the results, thus demonstrating that the look-up table was able to give the same results as the chemistry module. The mesh used for the single wire simulations is shown in Figure 5.3. The mesh was unstructured, and used a finer discretization near the wire surface to capture the sharp gradients present in the boundary layer.

A detailed parametric study was performed for the 2D single wire problem to gain some insight into the effects of wire diameter, wire spacing and catalyst activity on the conversion and selectivity. The wire size and separation distance were based on typical values from the literature. Referring to Figure 5.1, the wire diameter was varied from 0.05 to 0.10 mm, in steps of 0.01 mm, whilst the height of the inlet domain was varied from 1.0, 1.5 and 2.0 wire diameters.

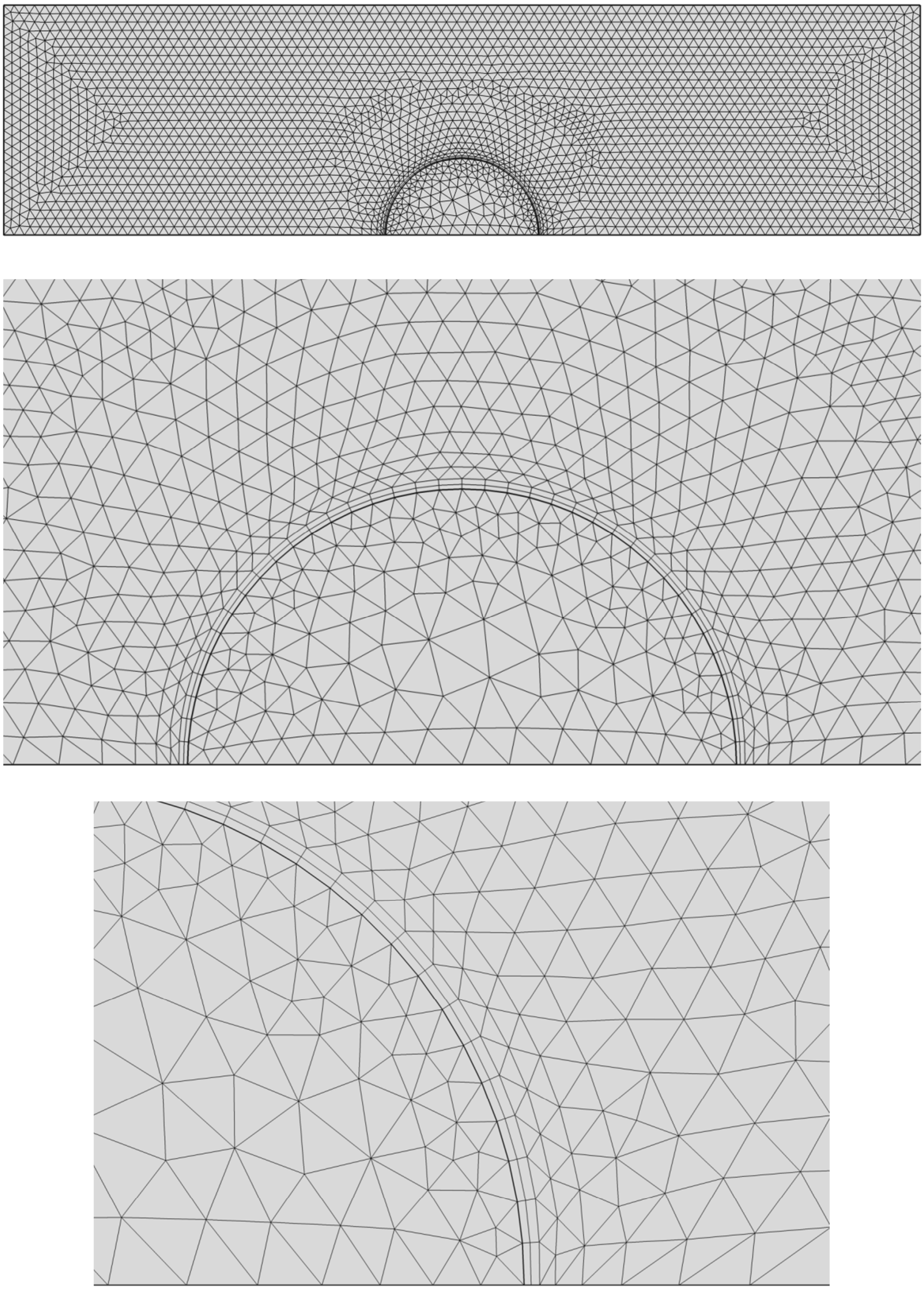

Figure 5.3 – Finite element mesh used for the single wire problem. The top view shows the full domain, the centre picture is a zoomed view of the elements around the wire surface, whilst the bottom shows a higher zoom of the boundary layer.

The first few figures shown simply illustrate the typical velocity, temperature and concentration profiles obtained around the wire for a variety of configurations. We show first some colour contour plots of the velocity profile around the wire. Figure 5.4 shows these plots for wire diameters of 0.05 and 0.10 mm, with a domain height of 1.0, 1.5 and 2.0 wire diameters. Note that these domain heights correspond respectively to centre to centre wire spacing of 2, 3 and 4 wire diameters.

It is evident and intuitive that for a lower domain height that the fluid is accelerated more as it passes over the wire. Furthermore, we see the formation of vorticies behind the wire. We see a stable vortex, which is normally expected for the Reynolds number present in these simulations, which is about 60. A zoomed view of the fluid vortex is shown in Figure 5.5 using velocity vectors.

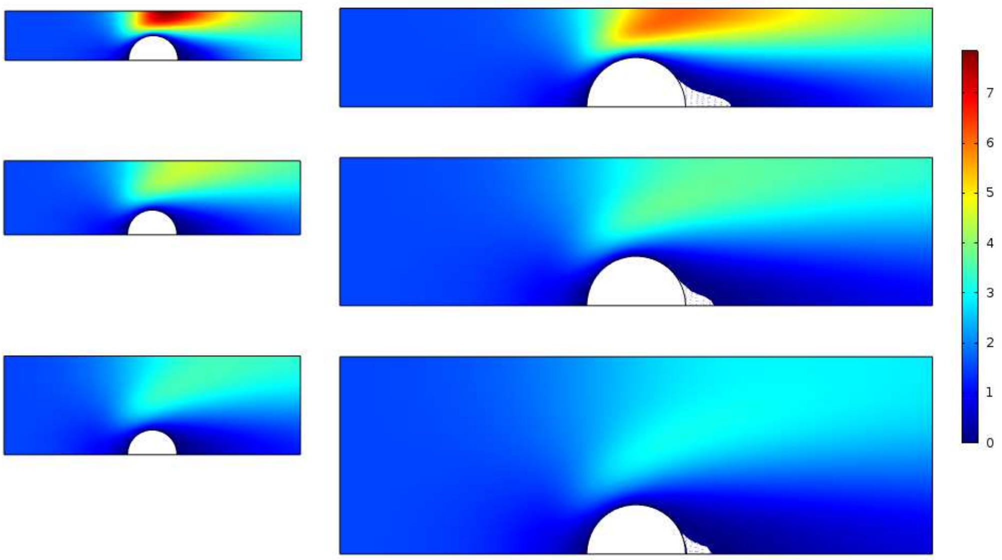

Figure 5.4 – Velocity contours for wire diameters of 0.05 mm (left) and 0.10 mm (right). From top to bottom, the domain height is equal to 1.0, 1.5 and 2.0 wire diameters.

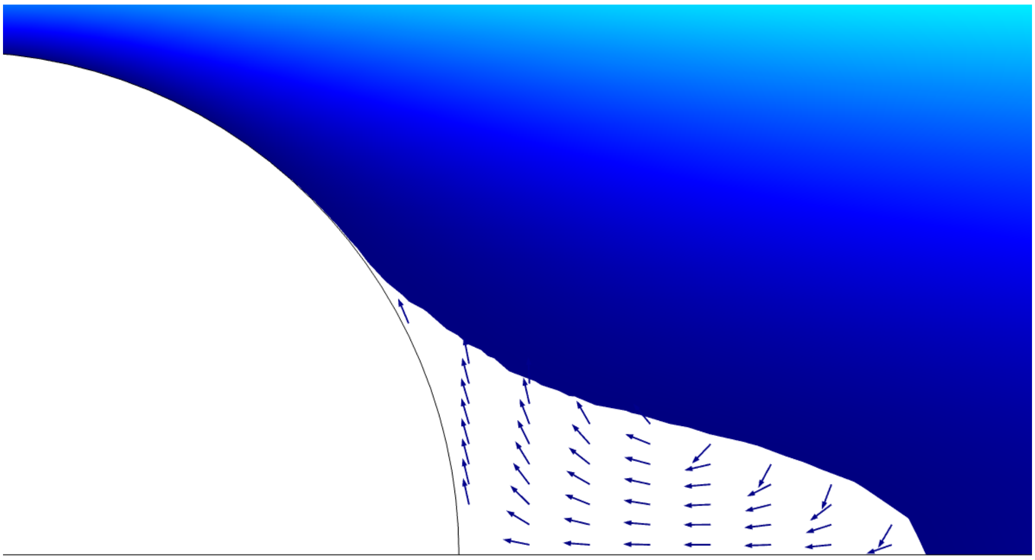

Figure 5.5 – Velocity contours for wire diameters of 0.05 mm (left) and 0.10 mm (right). From top to bottom, the domain height is 1.0, 1.5 and 2.0 wire diameters.

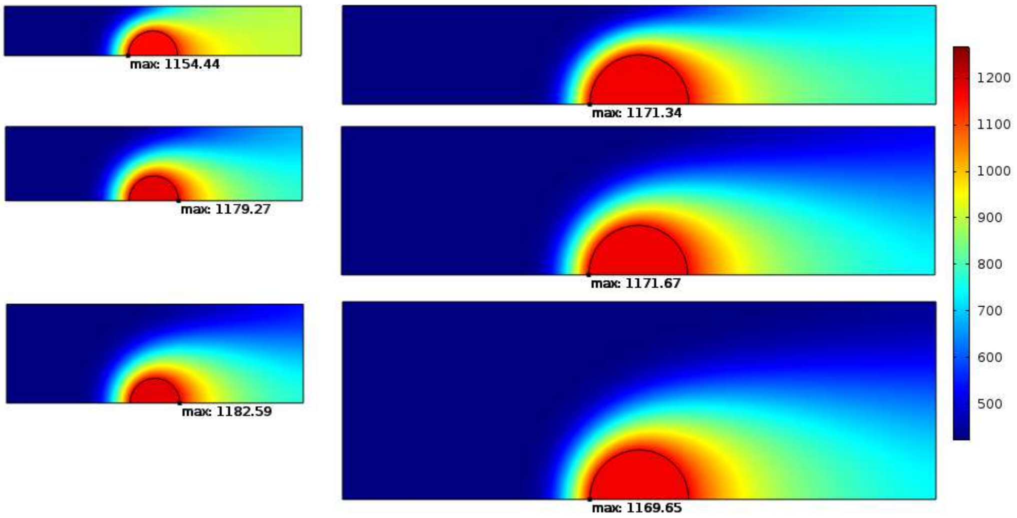

Figure 5.6 – Temperature contours for wire diameters of 0.05 mm (left) and 0.10 mm (right). From top to bottom, the domain height is equal to 1.0, 1.5 and 2.0 wire diameters.

Figure 5.6 shows the temperature pattern in the domain, again for the same wire and domain sizes used in Figure 5.4. Not surprisingly, the temperature is the highest on the wire surface. The outlet gas temperature profile is more uniform as the domain height decreases, which again is expected. The temperature of the wire is very uniform, which is a result of the small diameter and the relatively high thermal conductivity of platinum.

(NOTE: Although it is not physically meaningful, simulations were performed when the thermal conductivity of the wire was zero, and a strong temperature variation around the perimeter was observed.)

One of the main motivations of this work was to determine the selectivity of the reaction towards N_2O production, and see if this selectivity was a function of geometry and if it varied around the perimeter of the wire. Figure 5.7 shows the concentration (mass fraction) contours for ammonia, whilst Figure 5.8 shows the same for N_2O. The geometries are the same shown in Figures 5.4 and 5.6.

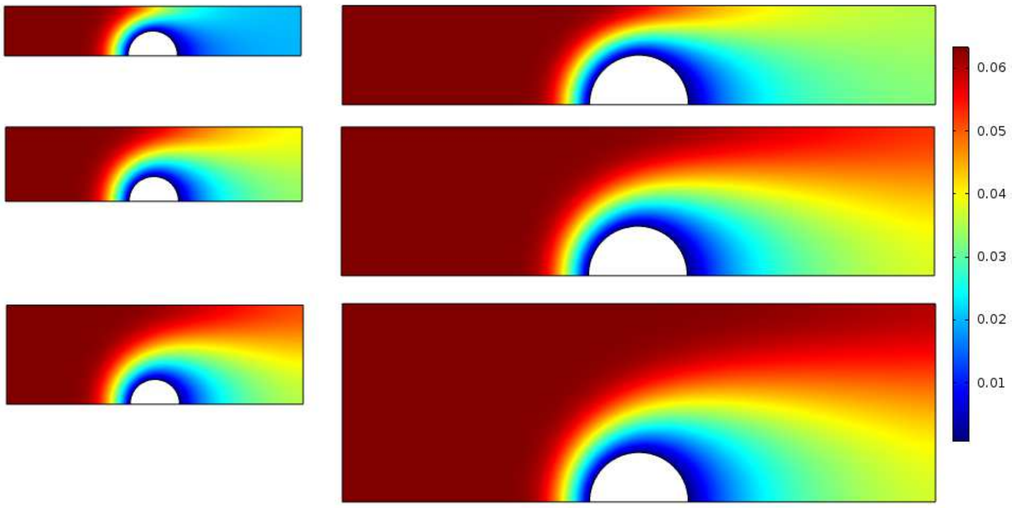

Figure 5.7 – Mass fraction contours of ammonia in the solution domain for the same system geometries mentioned in Figure 5.4 and 5.6.

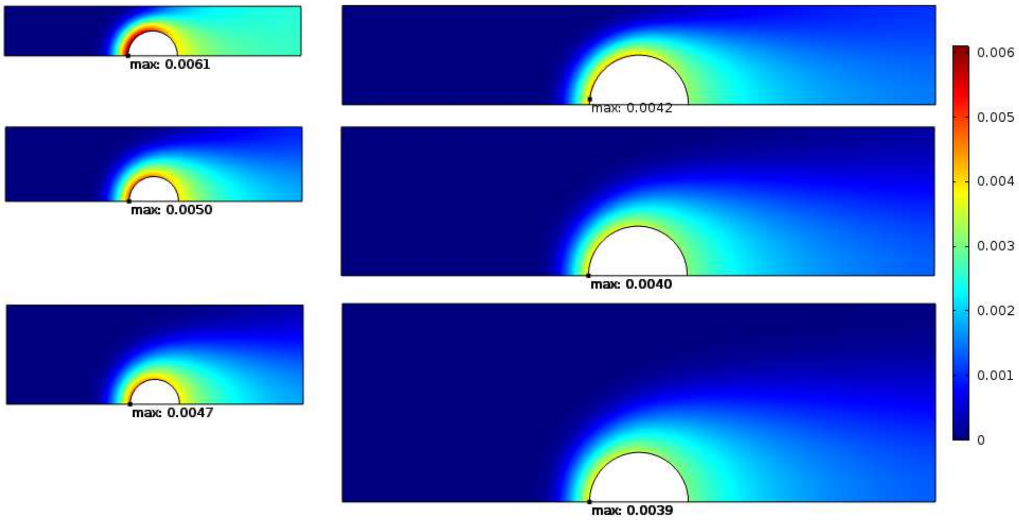

Figure 5.8 – Mass fraction contours of ammonia in the solution domain for the same system geometries mentioned in Figure 5.4 and 5.6.

Both figures show strong concentration gradients near the wire surface, showing the strong mass transfer limitation of the reaction. We also observe that as the spacing between the wires is reducing (decreasing domain height) the total conversion of ammonia increases. However, in this case, there is also an increase in N_2O concentration at the surface.

As mentioned, we are very interested in knowing how the selectivity to NO and N_2O changes as we move around the wire perimeter. It has already been shown that the flow patterns around the wire are not uniform, with a stagnation point at the front and flow recirculation behind the wire.

Figure 5.9 shows the selectivity around the perimeter for wires of 0.05 mm and 0.10 mm in diameter, with the same three wire spacing used previously. We observe: (a) more N_2O is produced at the front of the wire than at the back, relative to the NO production. Furthermore, as the wire spacing is reduced, then the selectivity becomes worse.

Following Figure 5.9, we present the results of the complete parametric sensitivity study, showing the total system selectivity to N_2O production as a function of wire diameter, wire spacing and catalyst activity.

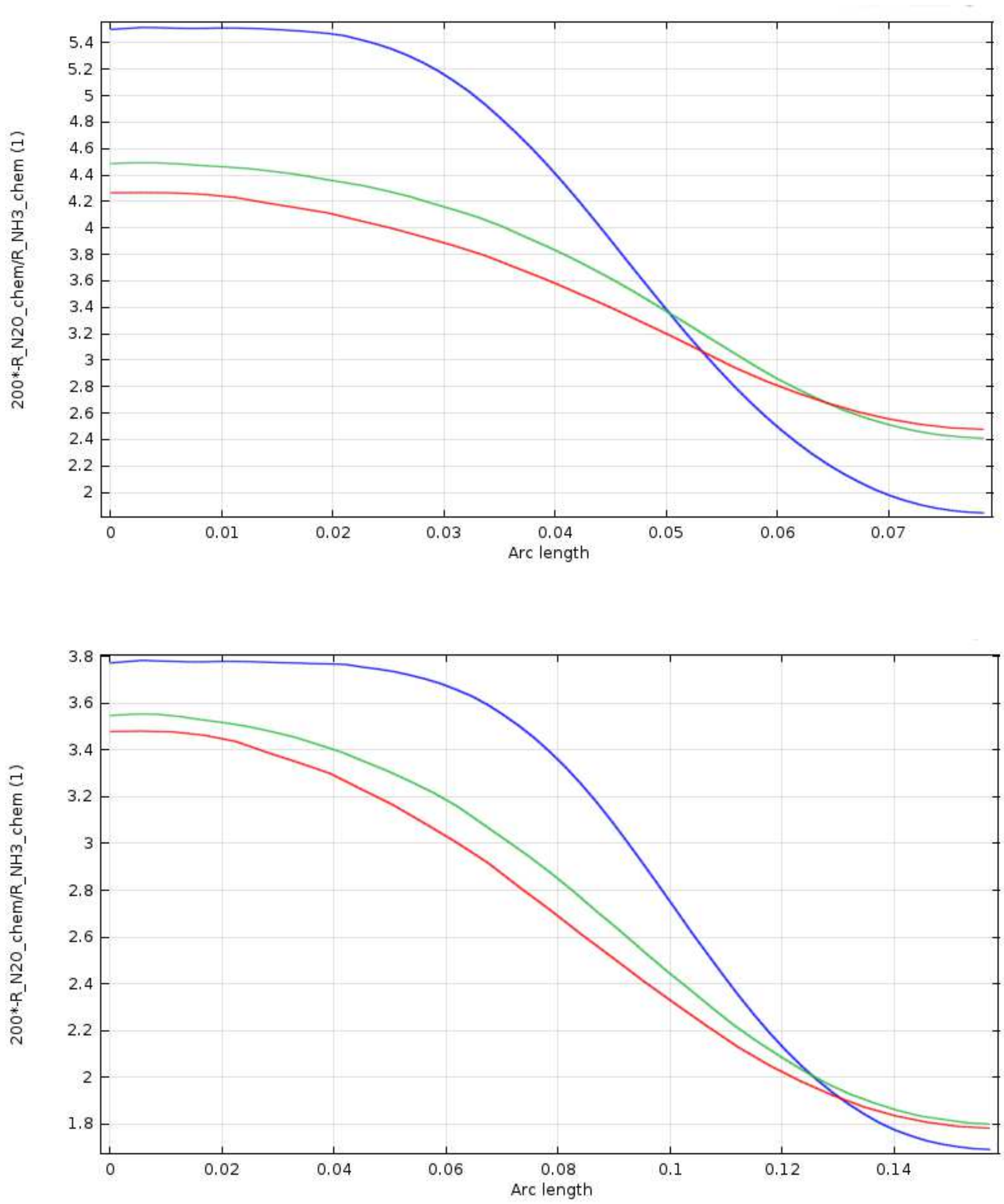

Figure 5.9 – Selectivity towards N_2O production for wire diameters of 0.05 and 0.10 mm. The three domain heights of 1.0 (blue), 1.5 (green) and 2.0 (red) were used. It is clear that there is a strong effect of the geometry on the selectivity.

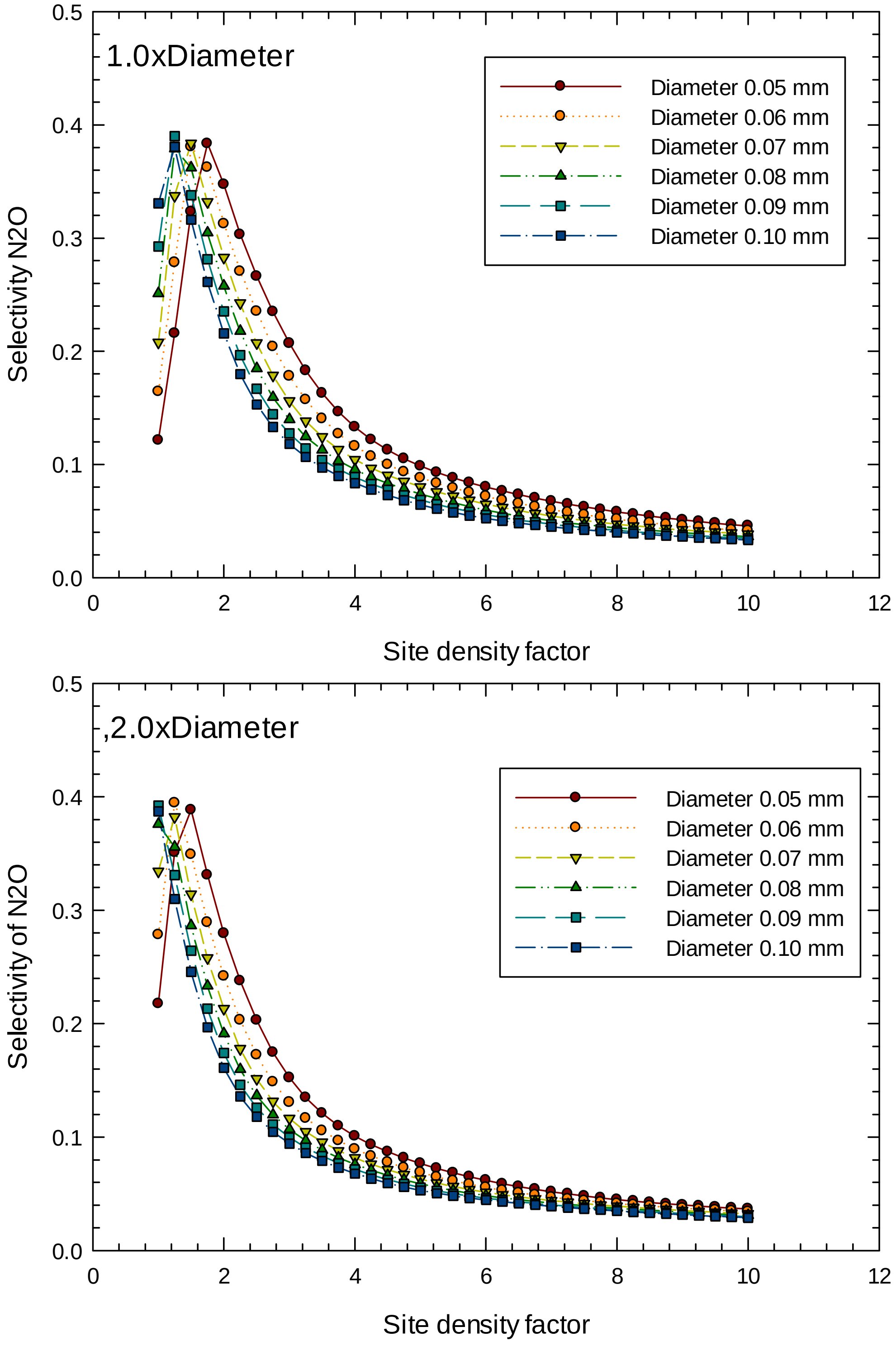

Figure 5.10 – Selectivity towards the production of N_2O at the system outlet as a function of wire diameter, wire spacing and catalyst activity. Top, domain height equals one wire diameter, bottom, two wire diameters.

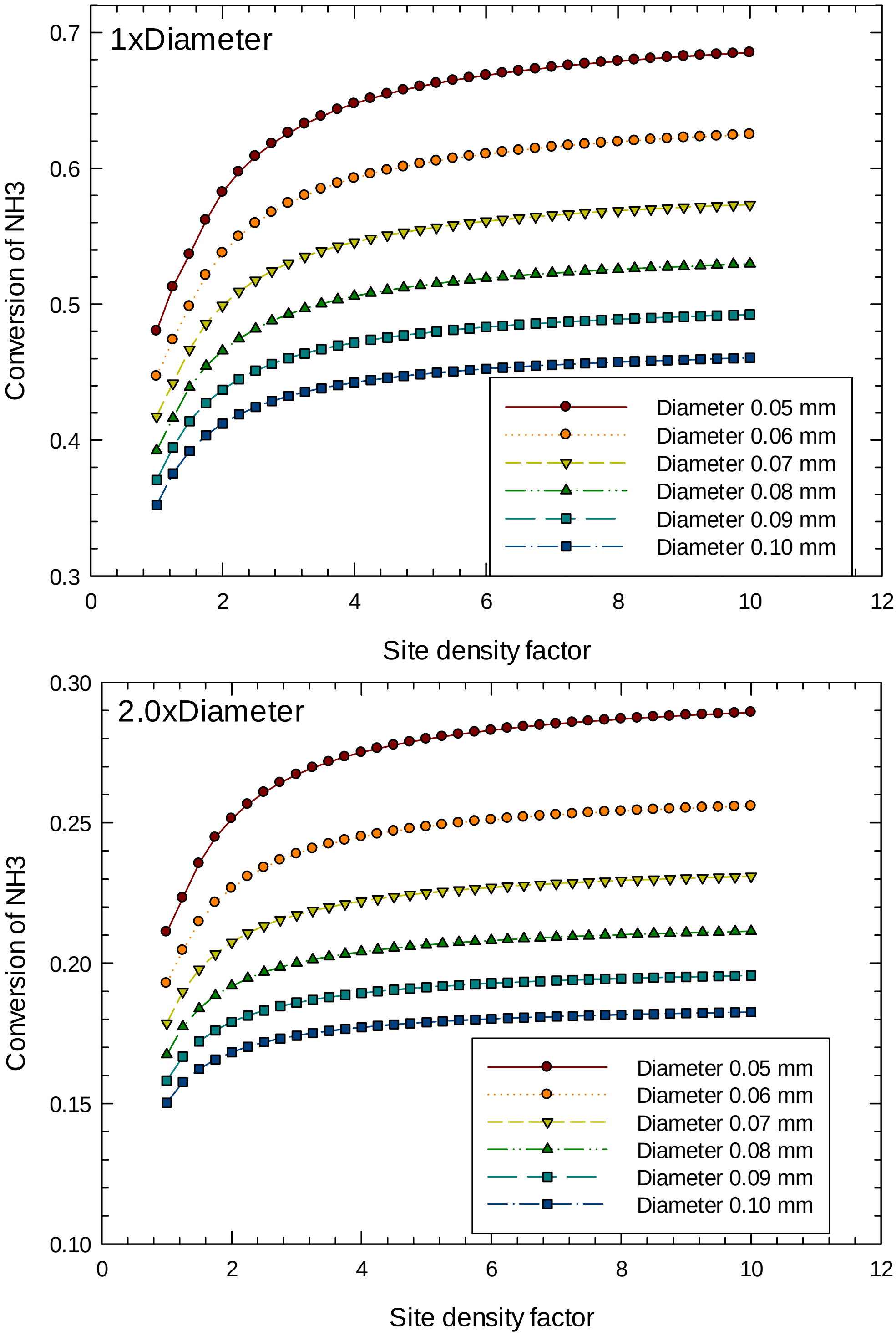

Figure 5.11 – Conversion at the system outlet as a function of wire diameter, wire spacing and catalyst activity. Top, domain height equals one wire diameter, bottom, two wire diameters.

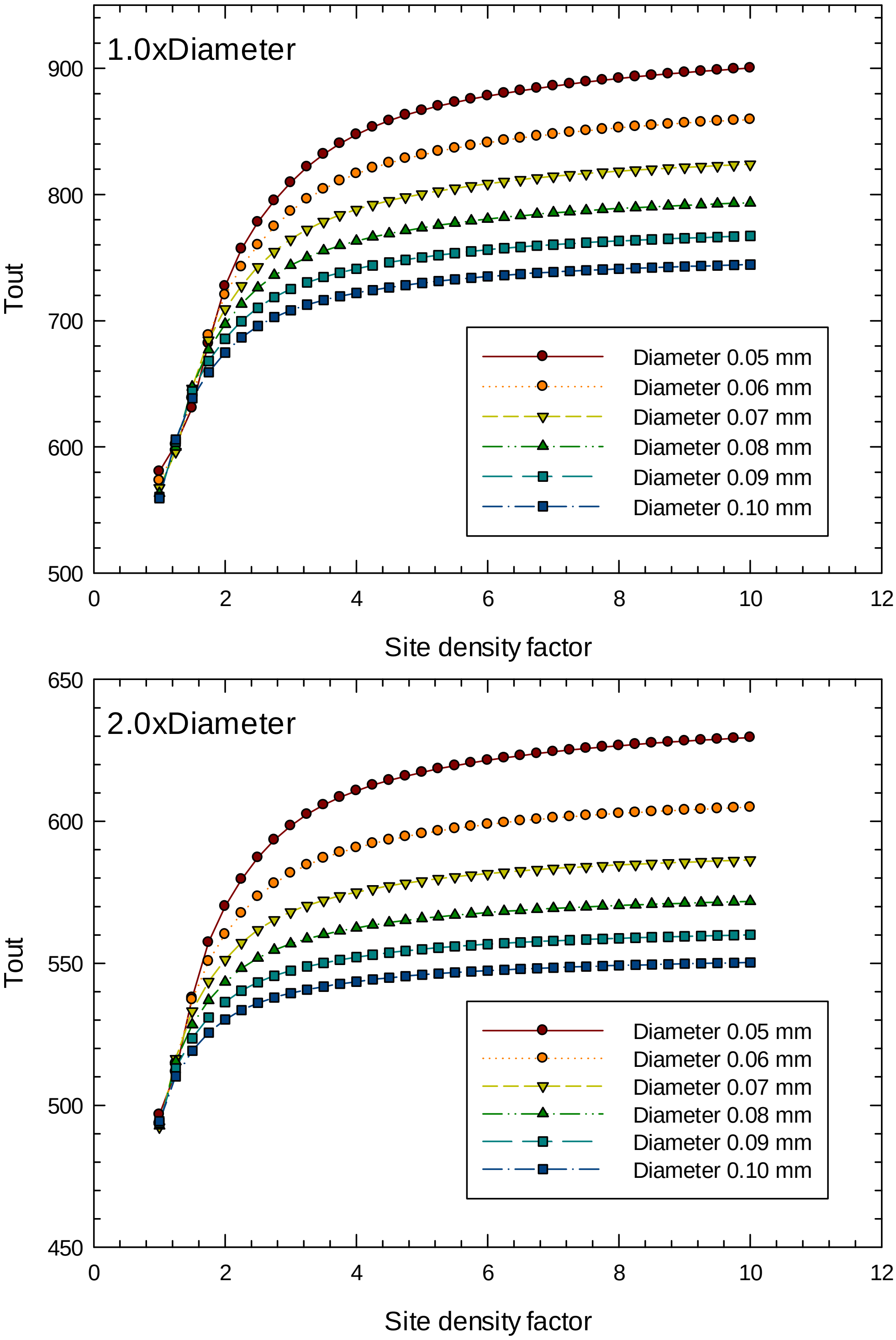

Figure 5.12 – Outlet temperature as a function of wire diameter, wire spacing and catalyst activity. Top, domain height equals one wire diameter, bottom, two wire diameters.

It is seen that conversion increases as the wire diameter is decreased, and the outlet temperature is corresponding higher. The same is true for an increase in catalyst activity. Initially, at relatively low catalyst activity, the selectivity to N_2O decreases as the catalyst activity increases. However, once it reaches a critical point the selectivity to NO improves rapidly. The selectivity is the highest for larger wire diameters. Overall, it can be concluded that the system geometry can play a key role in the N_2O production. Conversion is also favoured by a lower wire spacing.

5.3.2 2D parametric study for multiple wires

Having gained an appreciation of the rate and selectivity effects for a single wire, we turn now to the case of multiple wires. Two arrangements were selected, inline and staggered, as shown in Figure 5.13. A number of studies were performed for these two geometries. The wire diameter was varied from 0.05 to 0.10 mm as with the single wire study. The spacing of wires in the direction orthogonal to the flow was three wire diameters measured centre to centre. The effective catalyst activity was varied from an activity factor of 1 to 10. The effects of these parameters on the conversion and selectivity are shown in the following figures. The mesh used for each simulation is given in Figure 5.14.

The two arrangements obviously have different flow patterns. These are shown in the vector plot of Figure 5.15. Colour contour plots of the velocities are then shown in Figure 5.16 for the two shapes.

Figures 5.17 and 5.18 show the selectivity towards NO and N_2O production as a function of wire diameter and catalyst activity. Figure 5.17 relates to the inline arrangement and Figure 5.18 to the staggered one. These values are based on the production of each species evaluated at the exit. It is evident from the figures that the selectivity towards NO improves significantly as the catalyst activity increases. Furthermore the selectivity to NO also increases as the wire diameter increases.

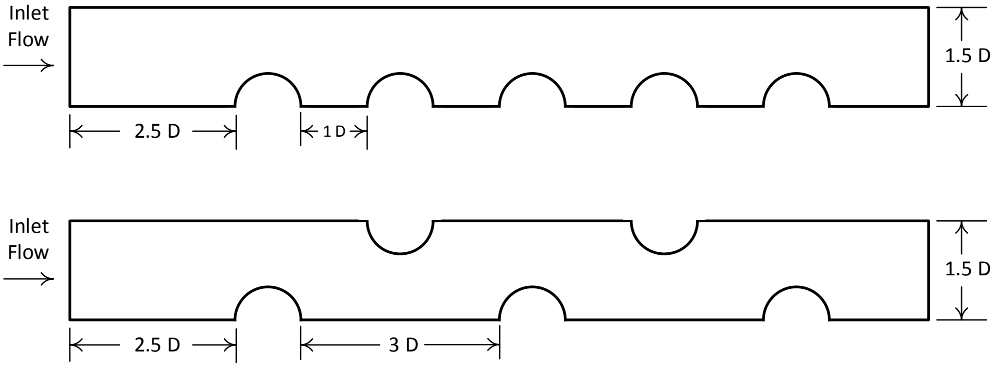

Figure 5.13 – Two arrangements for the five wires studied, inline and staggered.

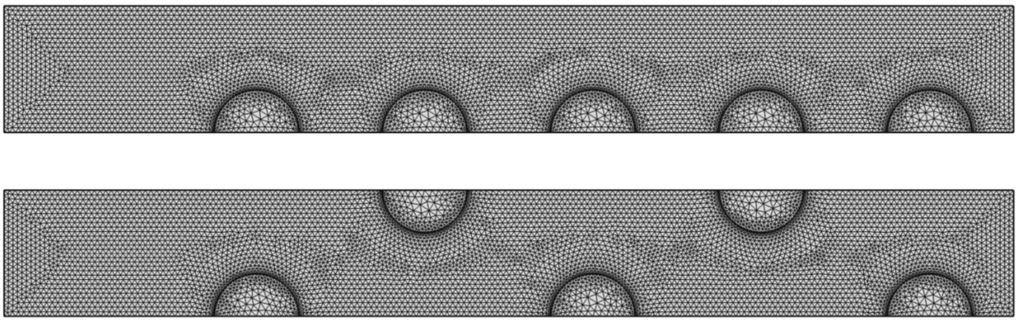

Figure 5.14 – Finite element meshes for the two multiple wire arrangements. The meshes had 12058 and 11961 elements for the inline and staggered respectively.

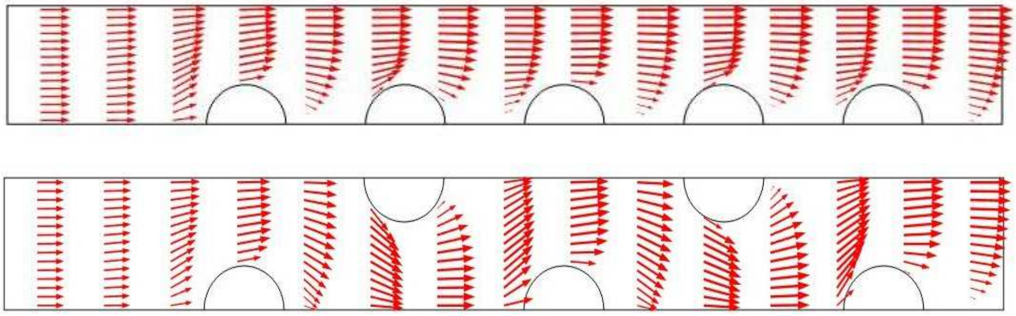

Figure 5.15 – Velocity patterns for the inline and staggered arrangement.

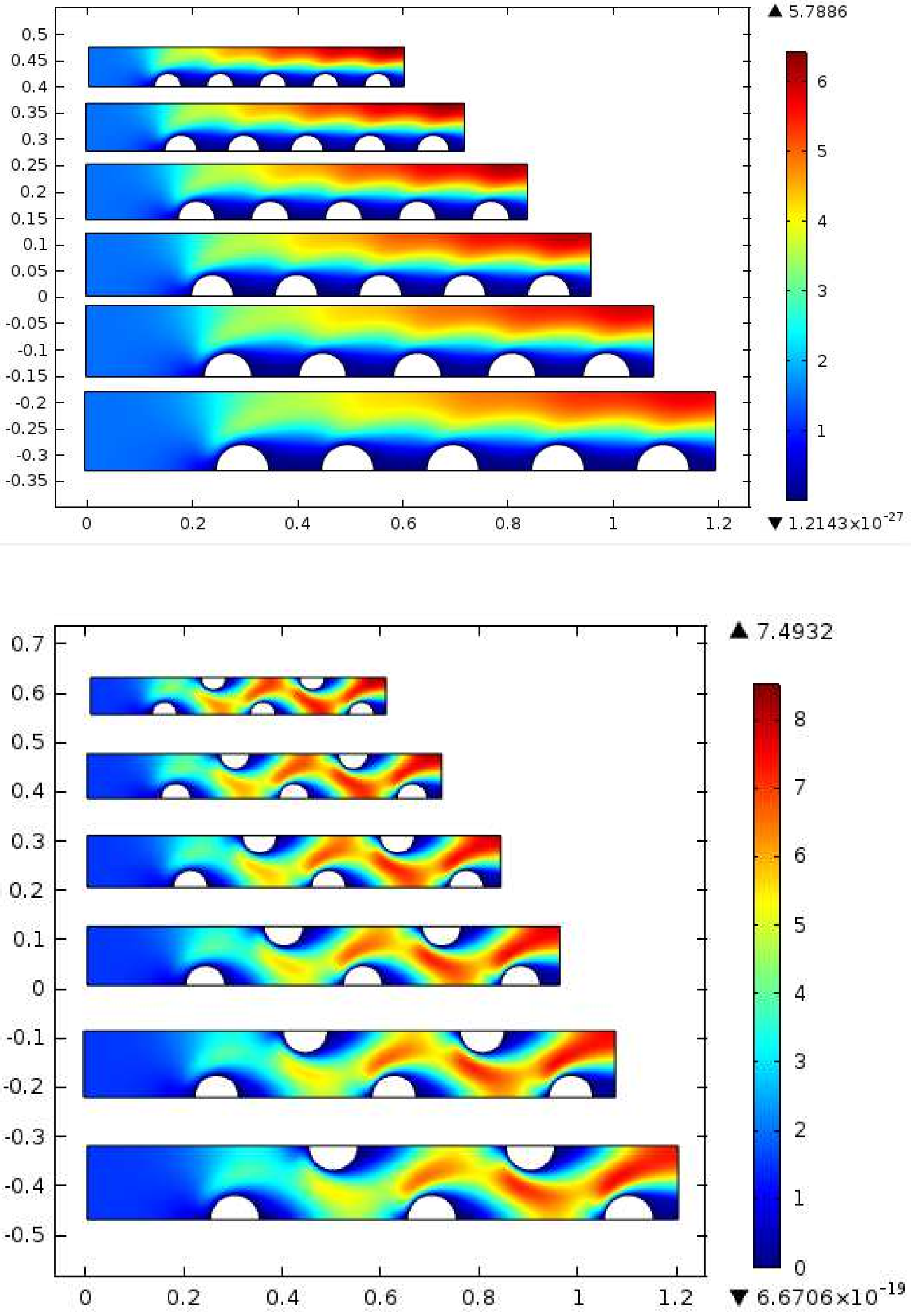

Figure 5.16 – Velocity contours for the two arrangements of wires.

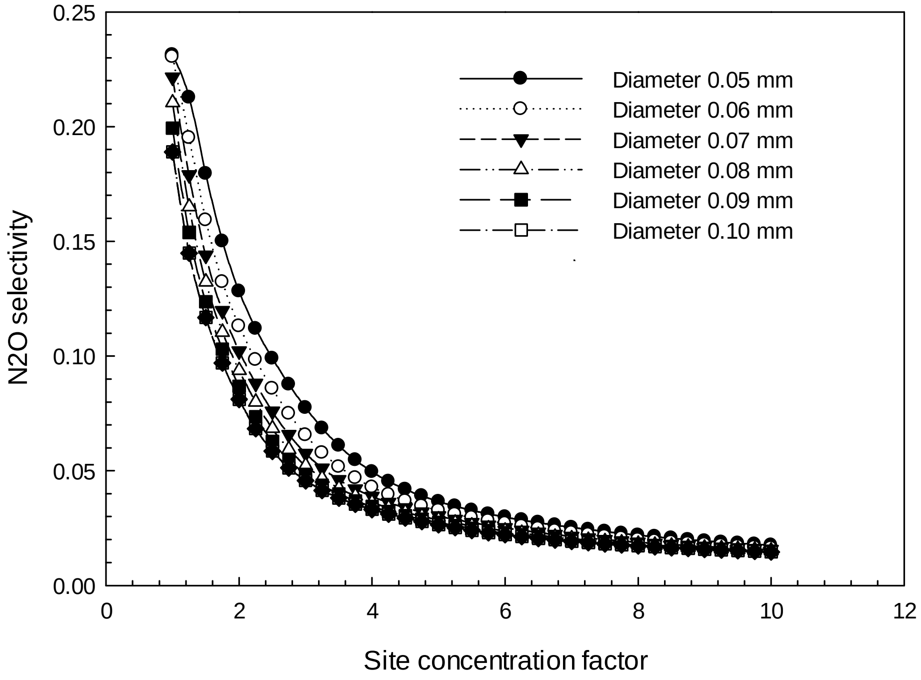

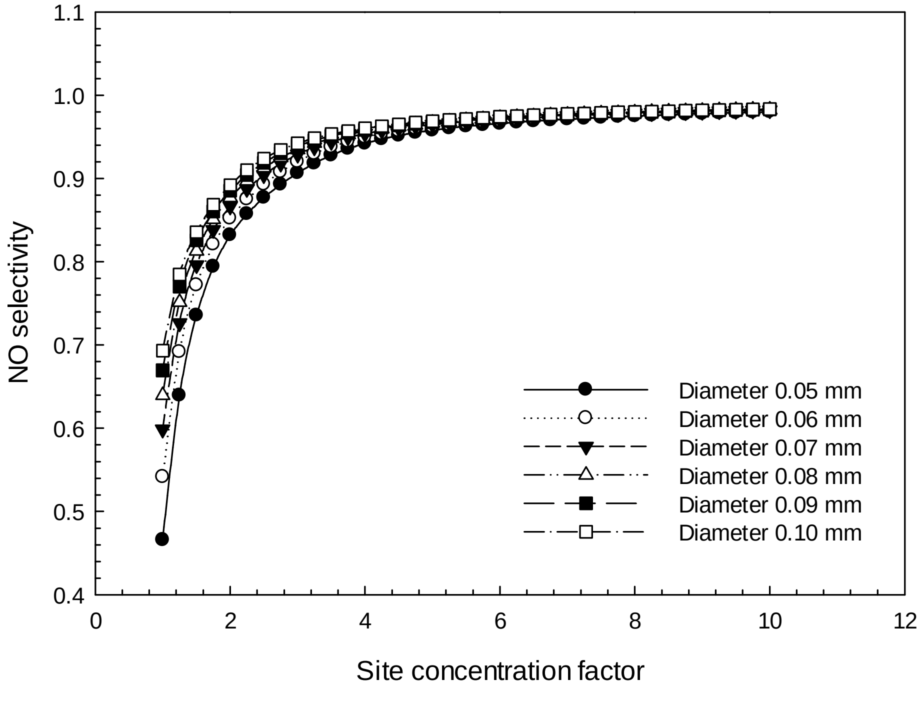

Figure 5.17 – Selectivity of the inline wire arrangement as a function of wire diameter and catalyst activity. Top, selectivity to N_2O and bottom, selectivity to NO.

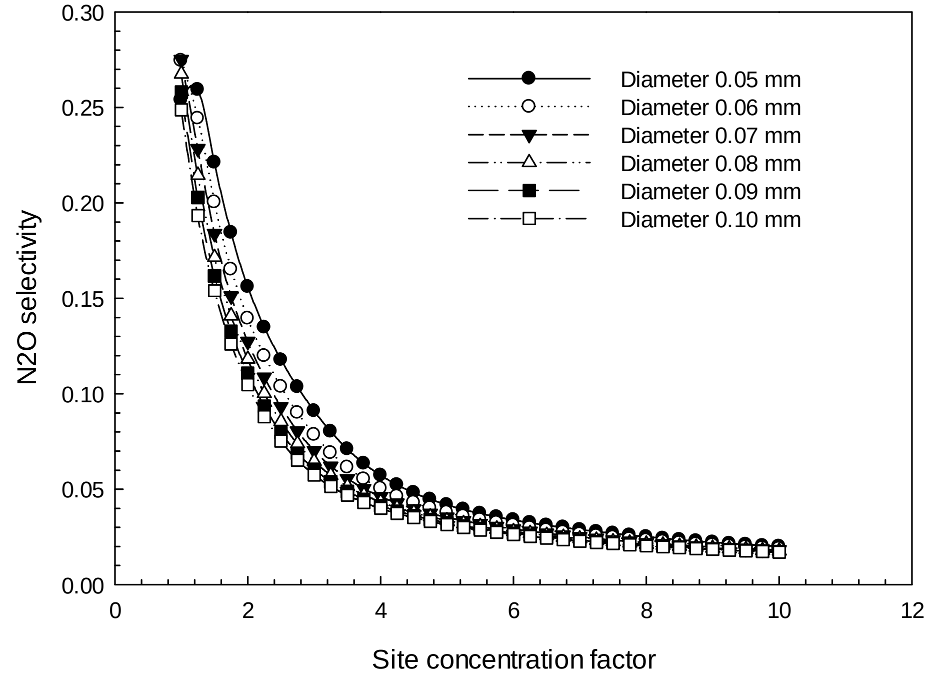

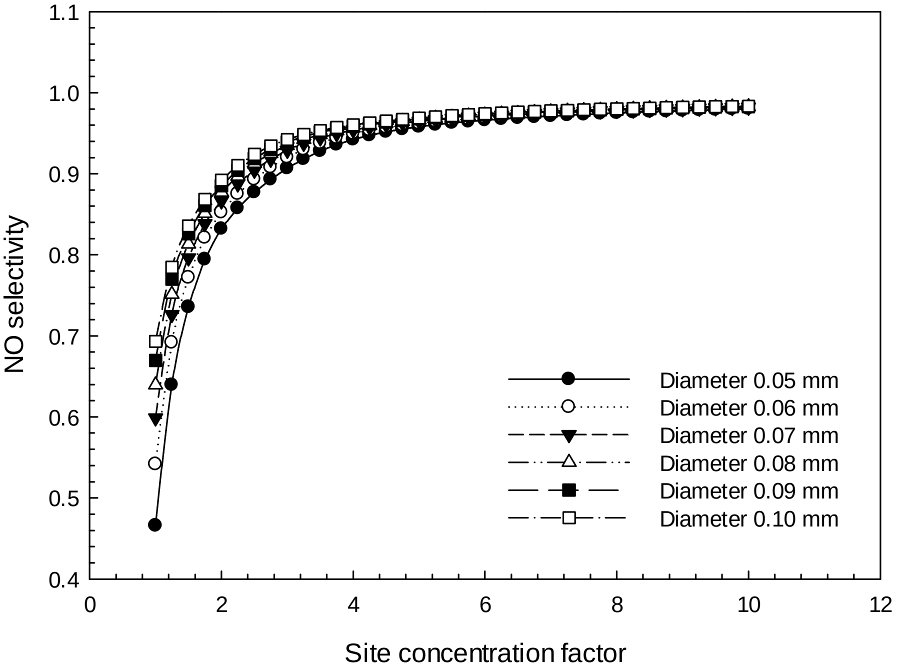

Figure 5.18 – Selectivity of the staggered wire arrangement as a function of wire diameter and catalyst activity. Top, selectivity to N_2O and bottom, selectivity to NO.

The total conversion of the ammonia decreases, however, as the wire diameter increases, see Figure 5.19 for the results for the two geometries. The outlet temperature, which is a direct function of the conversion, tracks the trend in the conversion, as shown in Figure 5.20. It is significant to note that the overall conversion is higher for the staggered arrangement, as is the outlet temperature. Note that the temperature values are close to the ones reported in the literature[20].

Prior to a discussion of the selectivity effects for each wire in the array, we present now some colour contour plots of the concentration of NH_3 and N_2O for the two geometries. Figure 5.21 shows the two concentration profiles for the inline geometry, while Figure 5.22 shows the same for the staggered arrangement. It is evident in all cases the concentration of NH_3 is relatively low at the surface, confirming the results obtained for the single wire case. All wires show strong mass transfer limitation, with the largest gradients for the first wire in both cases. Both of these figures pertain to a site concentration of 5.

It has been shown that selectivity depends on both the wire diameter as well as the catalyst activity. It was also observed that the selectivity varied around the wire perimeter (as it did for the case of the single wire). Furthermore, the selectivity changed from wire to wire, with the best selectivity to NO generally being seen on the wire that was nearest to the outlet.

It was shown for the single wire scenario that the selectivity varied around the perimeter of the wire. Figures 5.23 to 5.26 show how the selectivity varies not only around the perimeter of the wire, but also that it varies from wire to wire. Generally speaking, the selectivity is the worst at the front of the first wire. The downstream wires show a similar profile, with a decreasing selectivity towards N_2O. Obviously the wake from the upstream wires has an effect on the selectivity. The staggered arrangement is overall superior to the inline one.

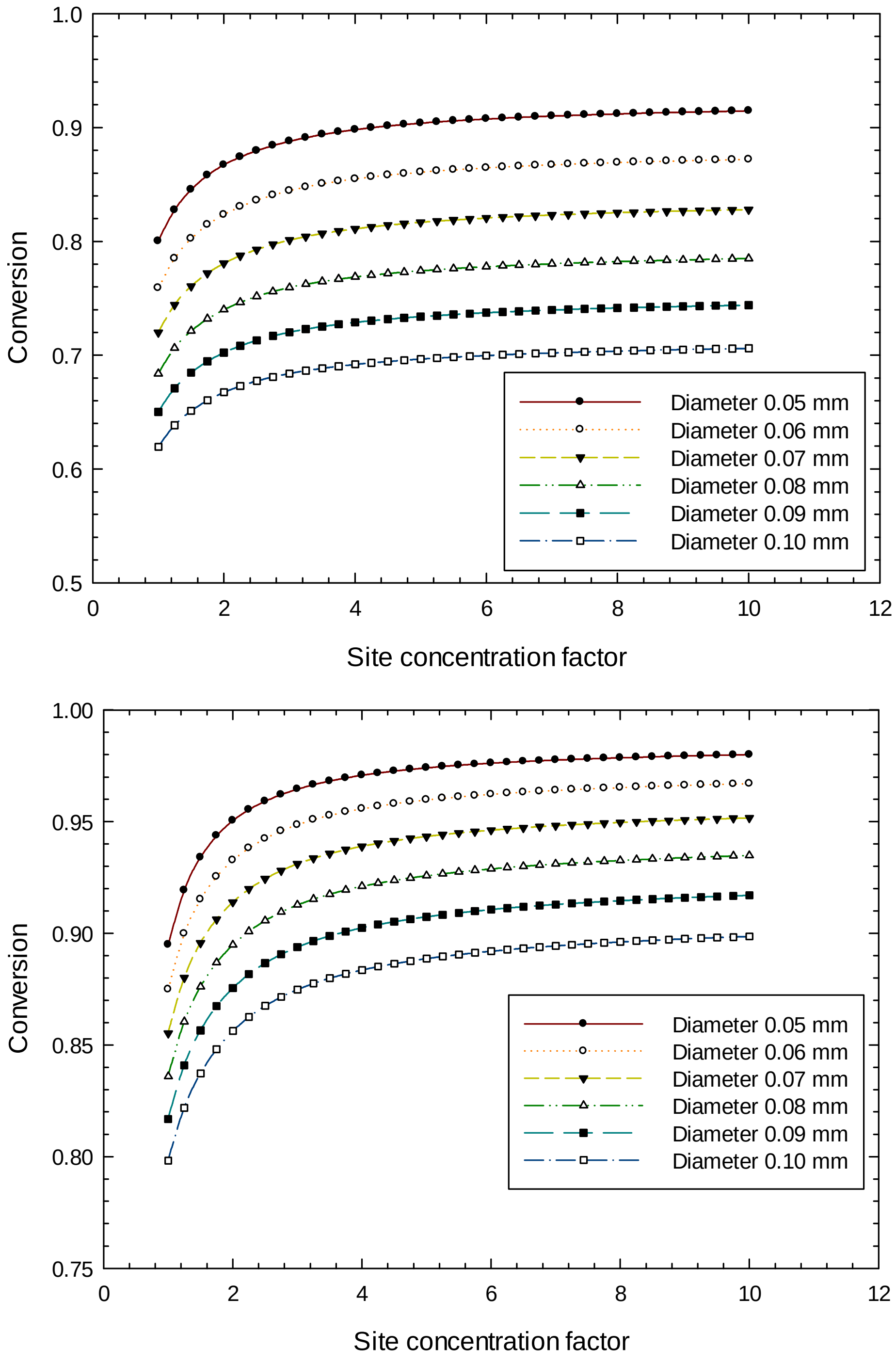

Figure 5.19 – Conversion as a function of catalyst activity and wire diameter for the two wire arrangements. Top, inline and bottom, staggered.

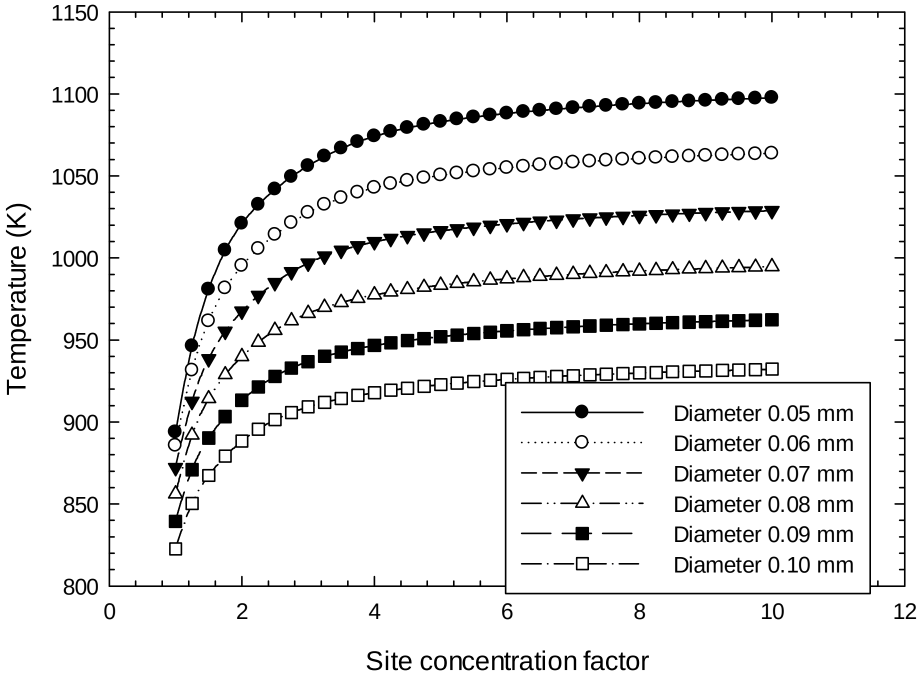

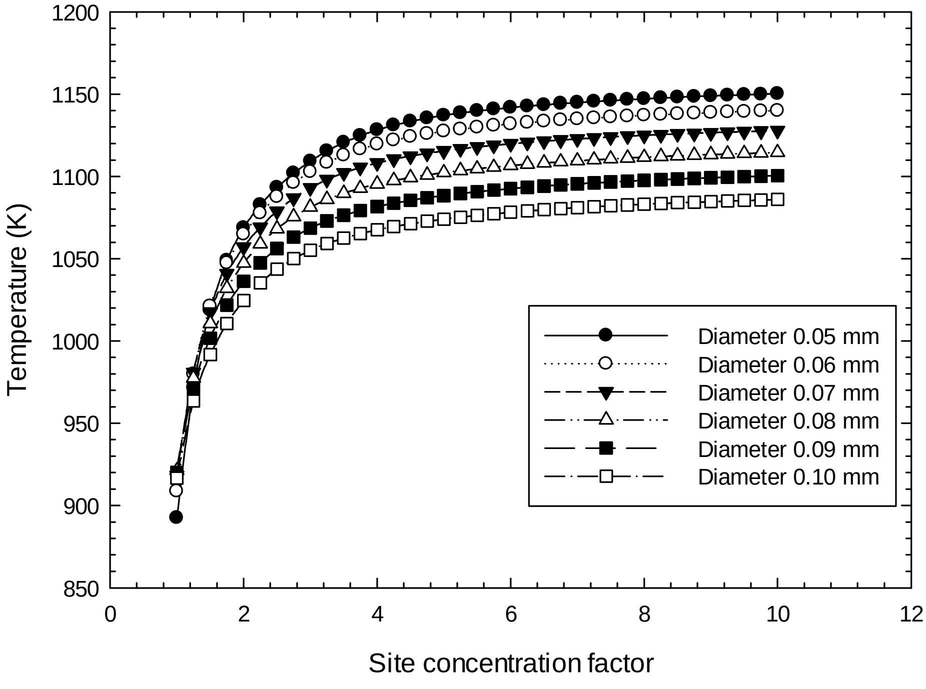

Figure 5.20 – Outlet temperature as a function of catalyst activity and wire diameter for the two wire arrangements. Top, inline and bottom, staggered.

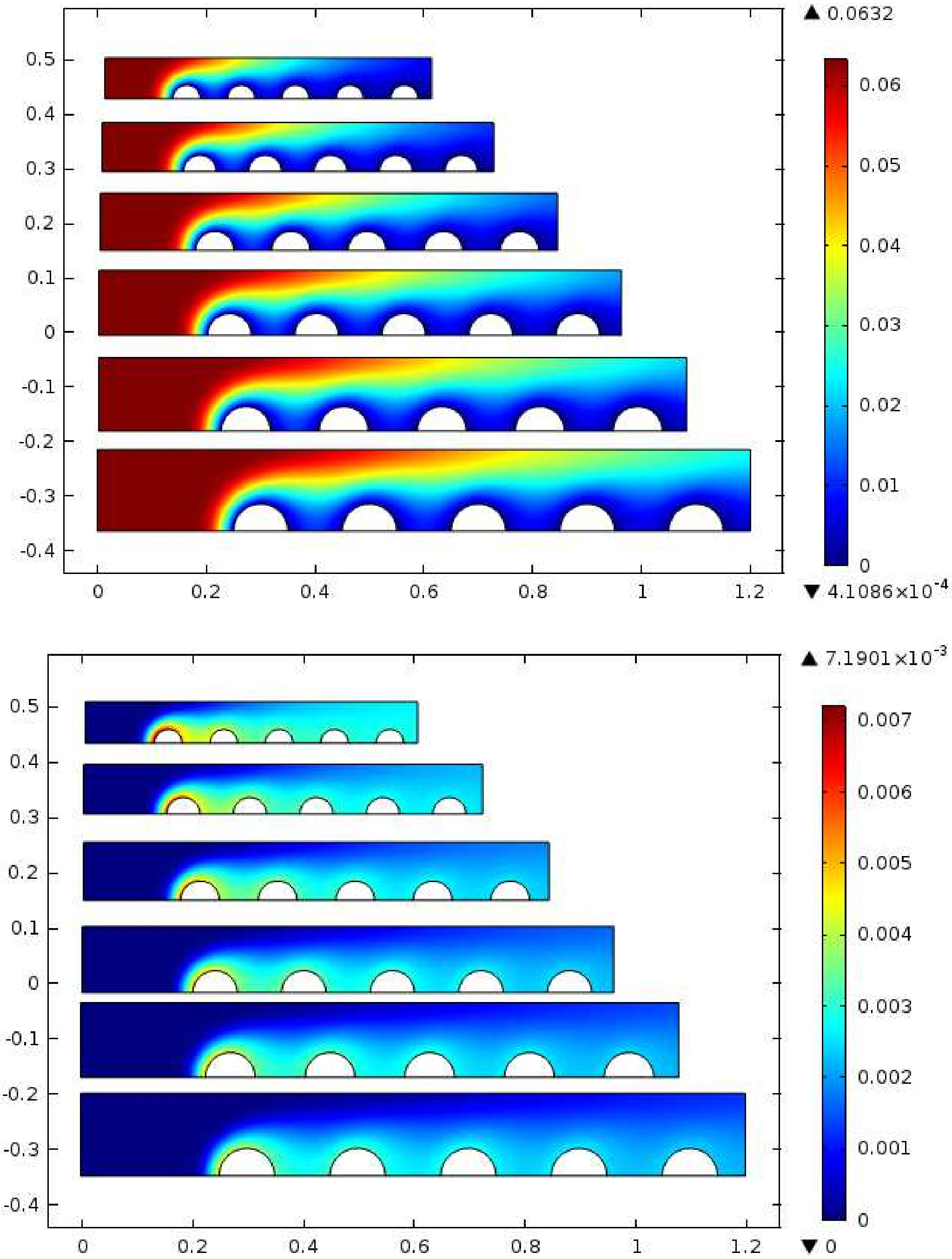

Figure 5.21 – Contour plots showing the mole fraction of ammonia (top) and nitrous oxide (bottom) for the inline wires as a function of wire diameter. The catalyst site concentration is five.

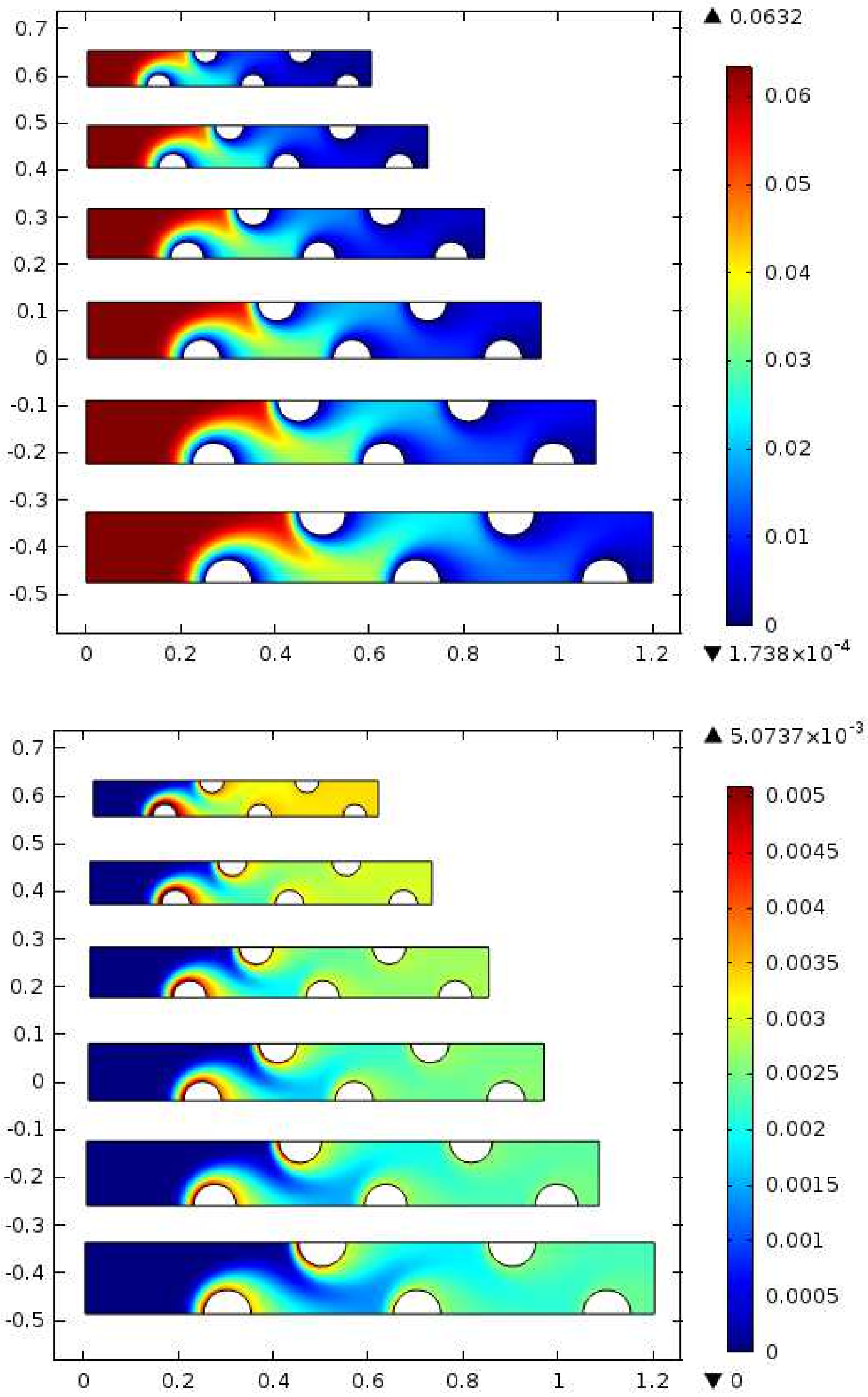

Figure 5.22 – Contour plots showing the mass fraction of ammonia (top) and nitrous oxide (bottom) for the staggered wires as a function of wire diameter. The catalyst site concentration is five.

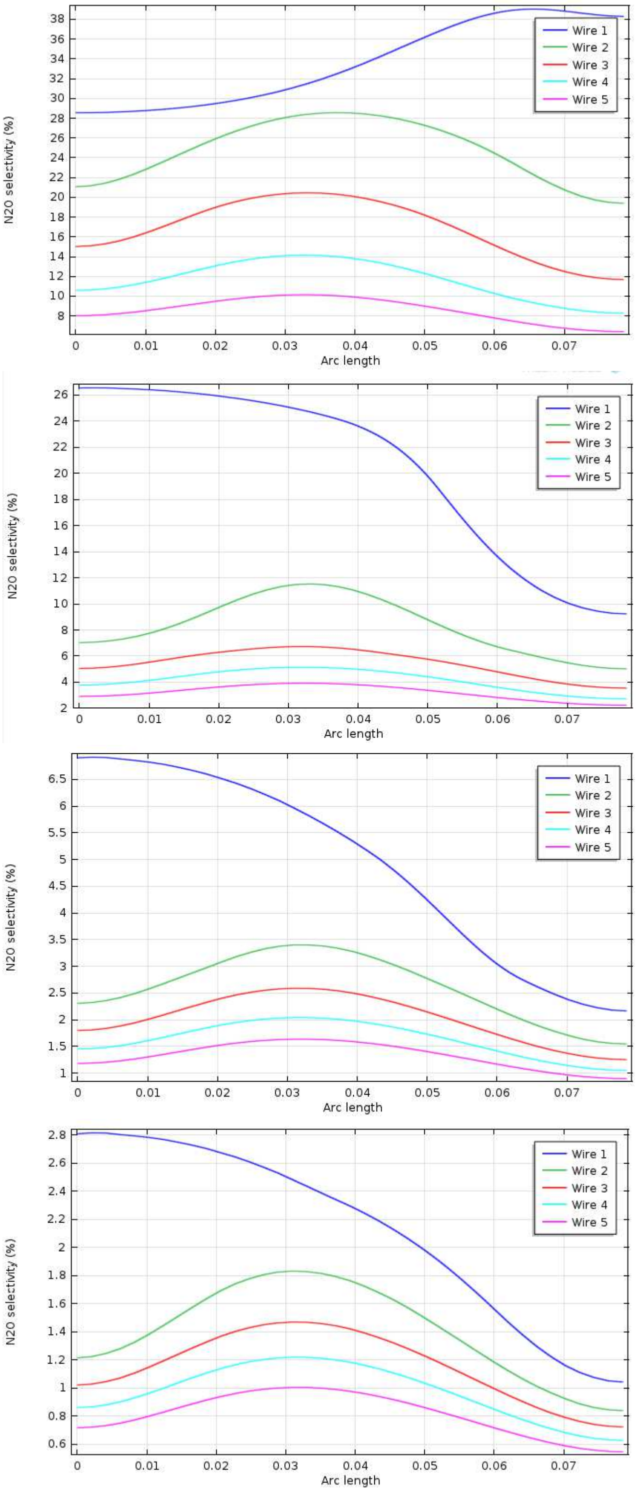

Figure 5.23 – Selectivity around the wire perimeter for the inline arrangement. The catalyst activity factor is, starting from the top, one, two, five and ten. The wire diameter is 0.05 mm.

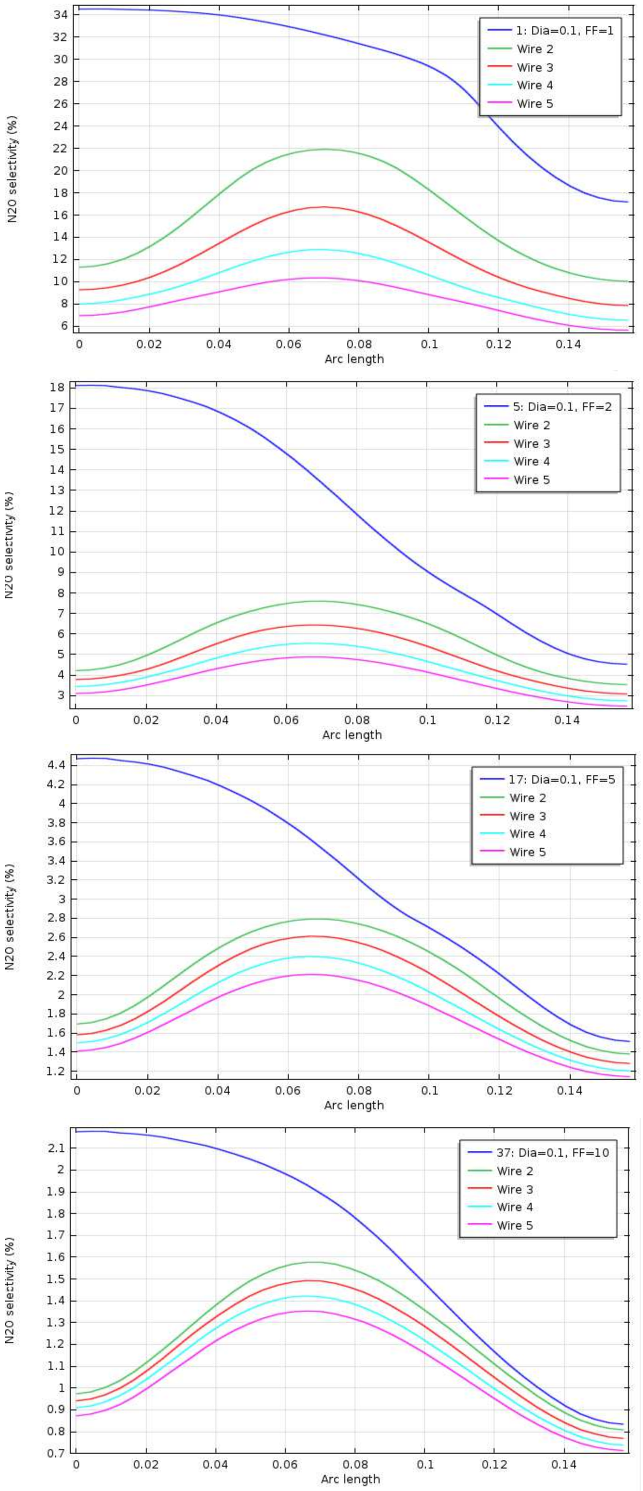

Figure 5.24 – Selectivity around the wire perimeter for the inline arrangement. The catalyst activity factor is, starting from the top, one, two, five and ten. The wire diameter is 0.10 mm.

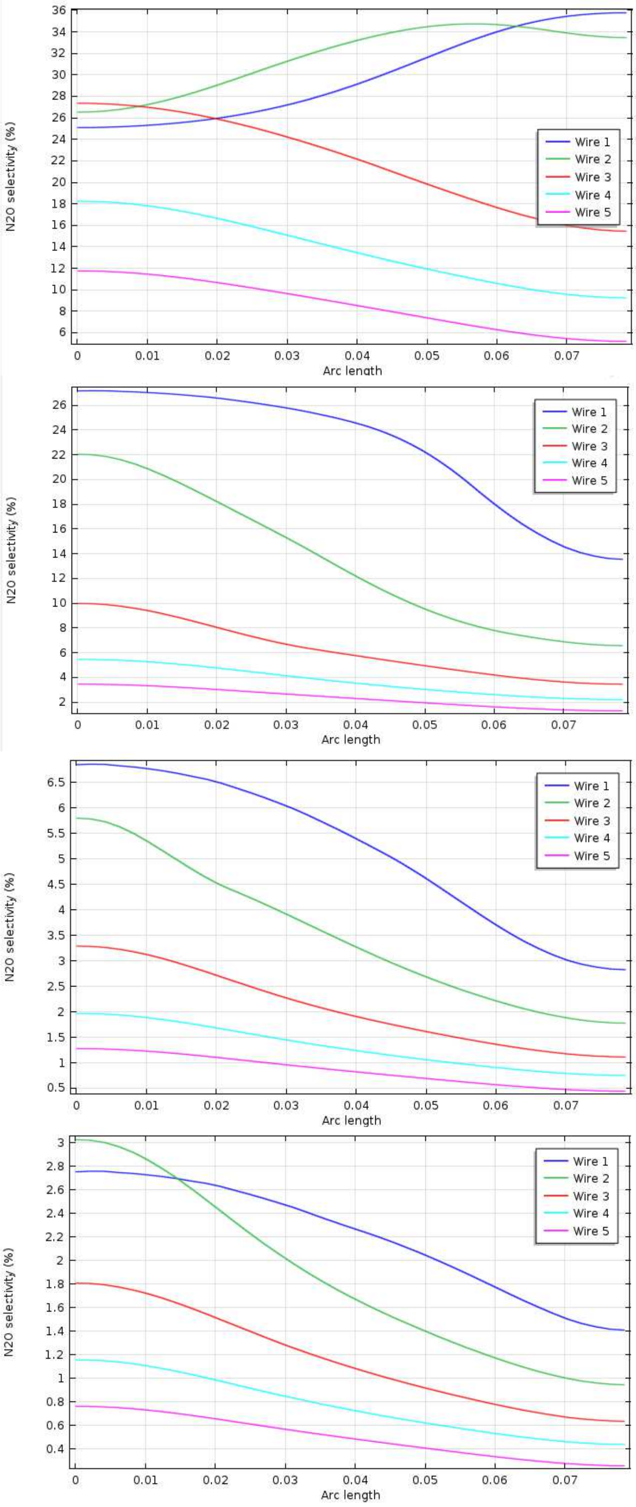

Figure 5.25 – Selectivity around the wire perimeter for the staggered arrangement. The catalyst activity factor is, starting from the top, one, two, five and ten. The wire diameter is 0.05 mm.

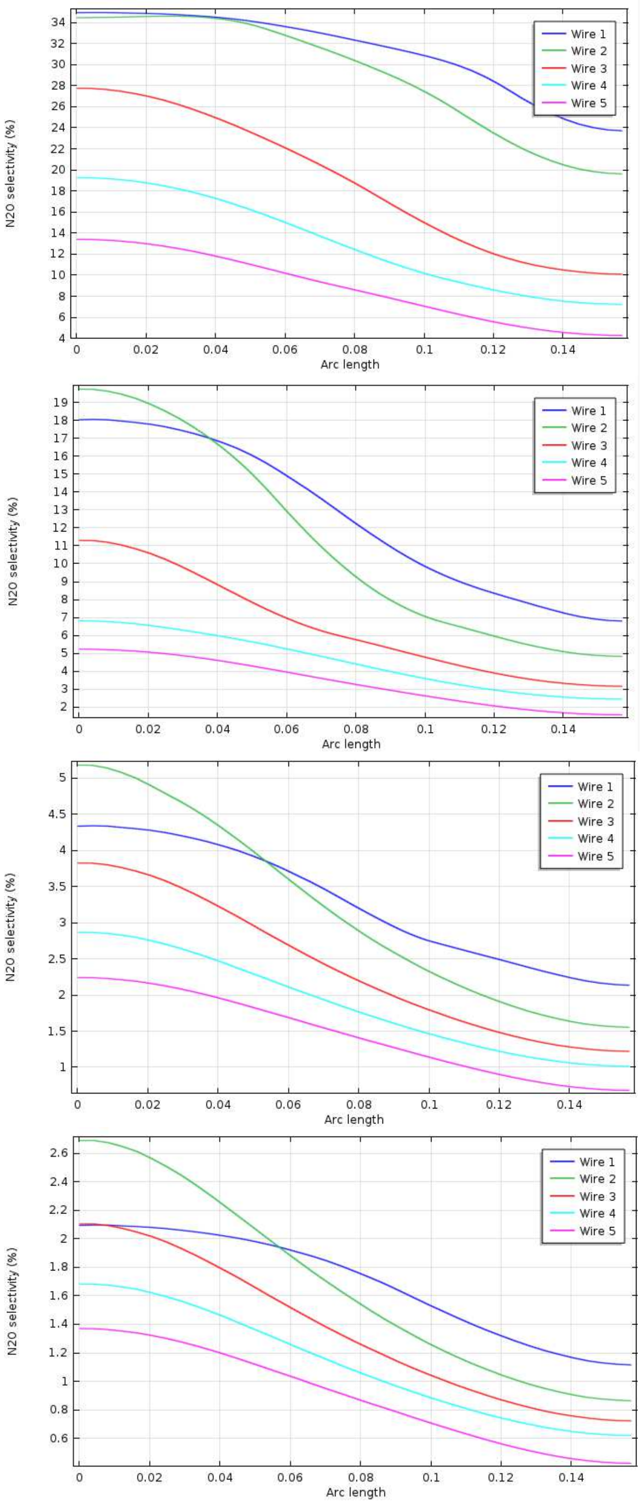

Figure 5.26 – Selectivity around the wire perimeter for the staggered arrangement. The catalyst activity factor is, starting from the top, one, two, five and ten. The wire diameter is 0.10 mm.

5.3.3 3D single wire parametric study.

The main features and trends of the reactor performance have been illustrated using the 2D configuration. However, the three dimensional case allows us to determine if there is an effect on the selectivity of the crossing of the wires, for example. The results shown here are based on a staggered arrangement of screens. The conceptual picture of this setup is shown in Figure 5.27. The top picture in this figure shows a frontal view of the screens. For a given layer of wires, the separation between two parallel wires is denoted by the distance 2*L*. The separation between two parallel wires in alternate layers is thus *L*, because of the staggered arrangement. Geometric symmetry allows for the frontal area described by the red box in Figure 5.27 to be used. The bottom picture in Figure 5.27 shows a perspective view, illustrating the total depth of the solution domain as twelve wires.

We show first the results obtained when only the first gauze layer (two orthogonal wires) are used. In this case the wire diameter was 0.10 mm and the spacing, *L*, was 0.15 mm. The activity factor was varied from 1 to 10 as before. The colour contour plot of the selectivity is given in Figure 5.28. The magnified view in the forefront illustrates that the selectivity varies in both directions. The flow patterns clearly have an effect on the selectivity.

Figure 5.29 shows the total ammonia conversion as a function of catalyst activity and wire spacing for the case of a single screen. As for the 2D case, we see that conversion rises as the wire spacing decreases and the catalyst activity rises. Figure 5.30 then shows the selectivity for NO and N_2O as the same variables are altered. In this case, over the range of parameters studied, there is not a significant change in selectivity with wire spacing.

Overall, the trends with the 3D single wire case are similar to the 2D case, except that we see a more complex geometrical dependence on the selectivity. In the next section, the case of six gauzes (twelve wires) is studied.

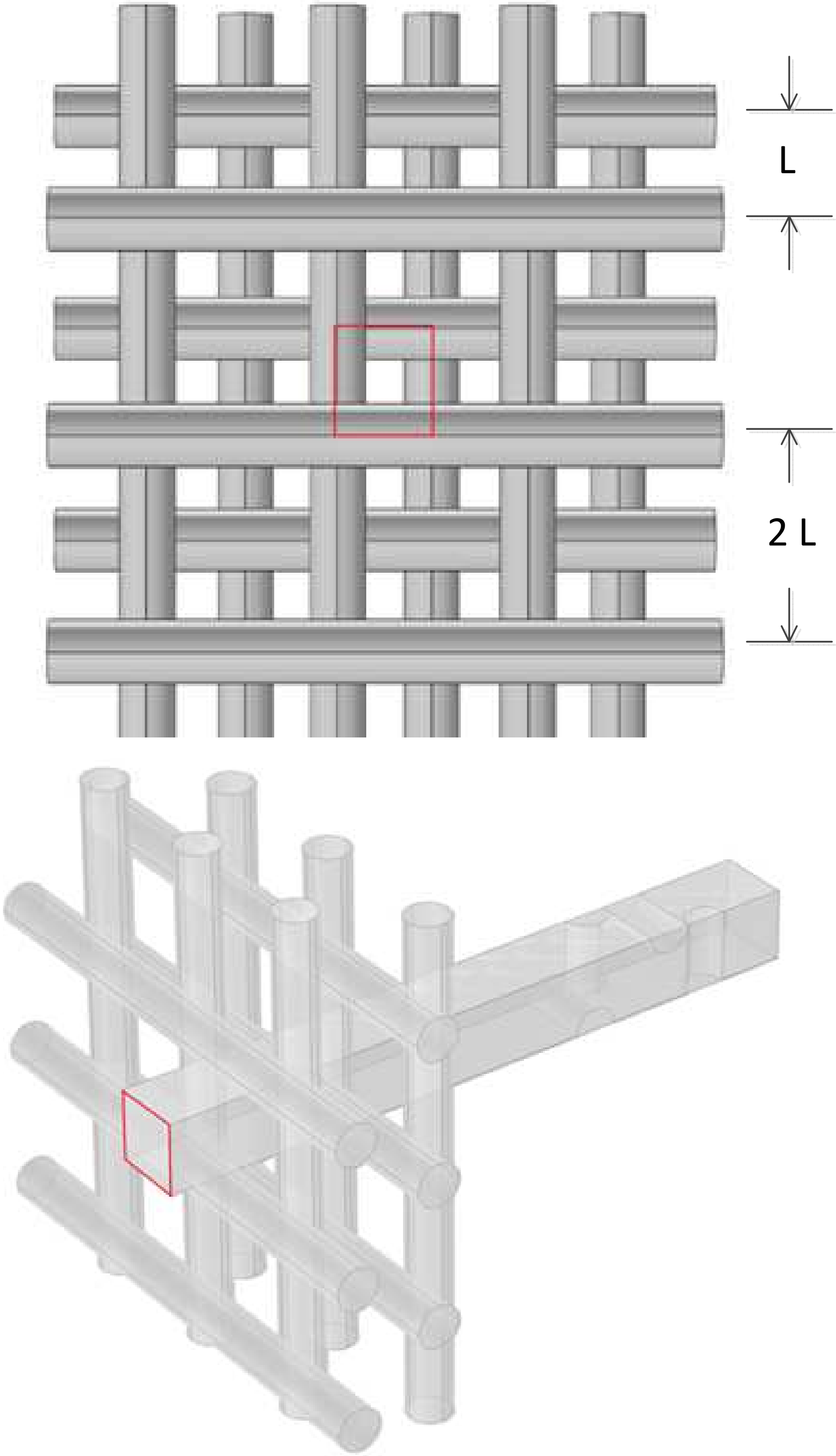

Figure 5.27 – 3D conceptualization of multiple screens with staggered arrangement. Top view shows the front view, whilst the bottom view shows the section used to form the 3D computational domain (red square).

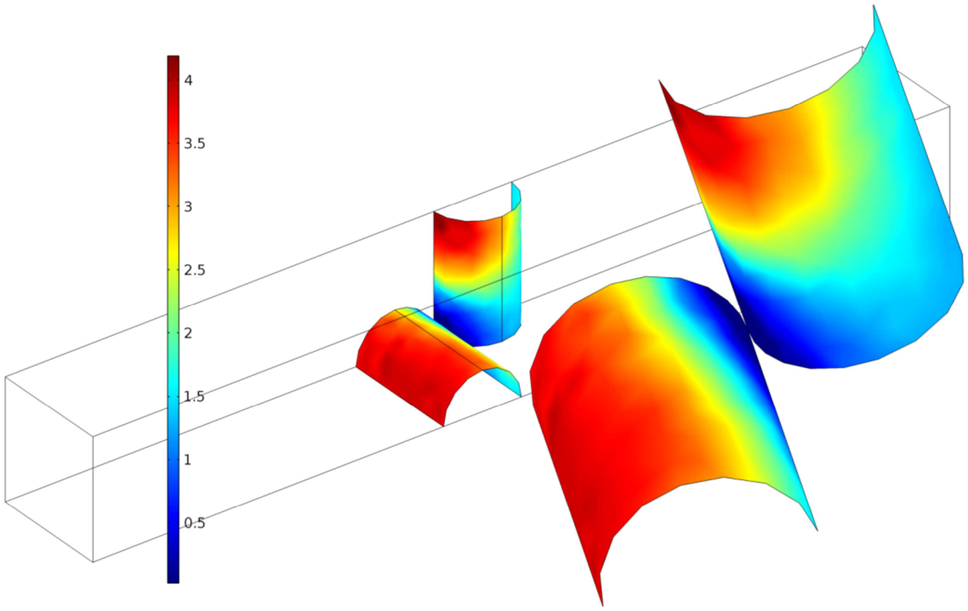

Figure 5.28 – Colour contours representing the selectivity to N_2O. The magnified view in the forefront illustrates that the selectivity varies in both directions. The flow patterns clearly have an effect on the selectivity. The wire diameter is 0.10 mm

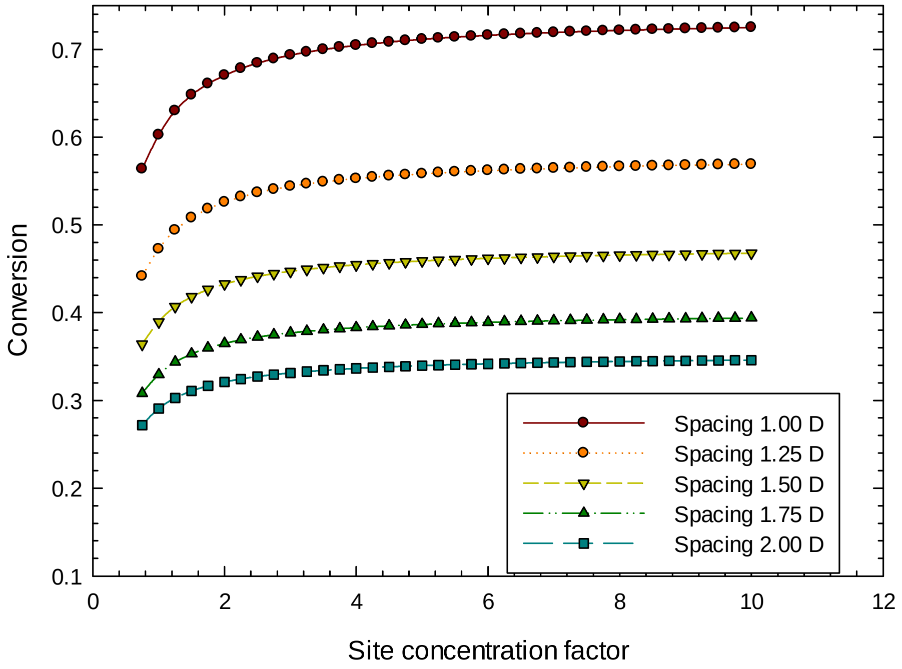

Figure 5.29 – Total ammonia conversion as a function of catalyst activity and wire spacing for the case of a single screen. The wire diameter was 0.10 mm.

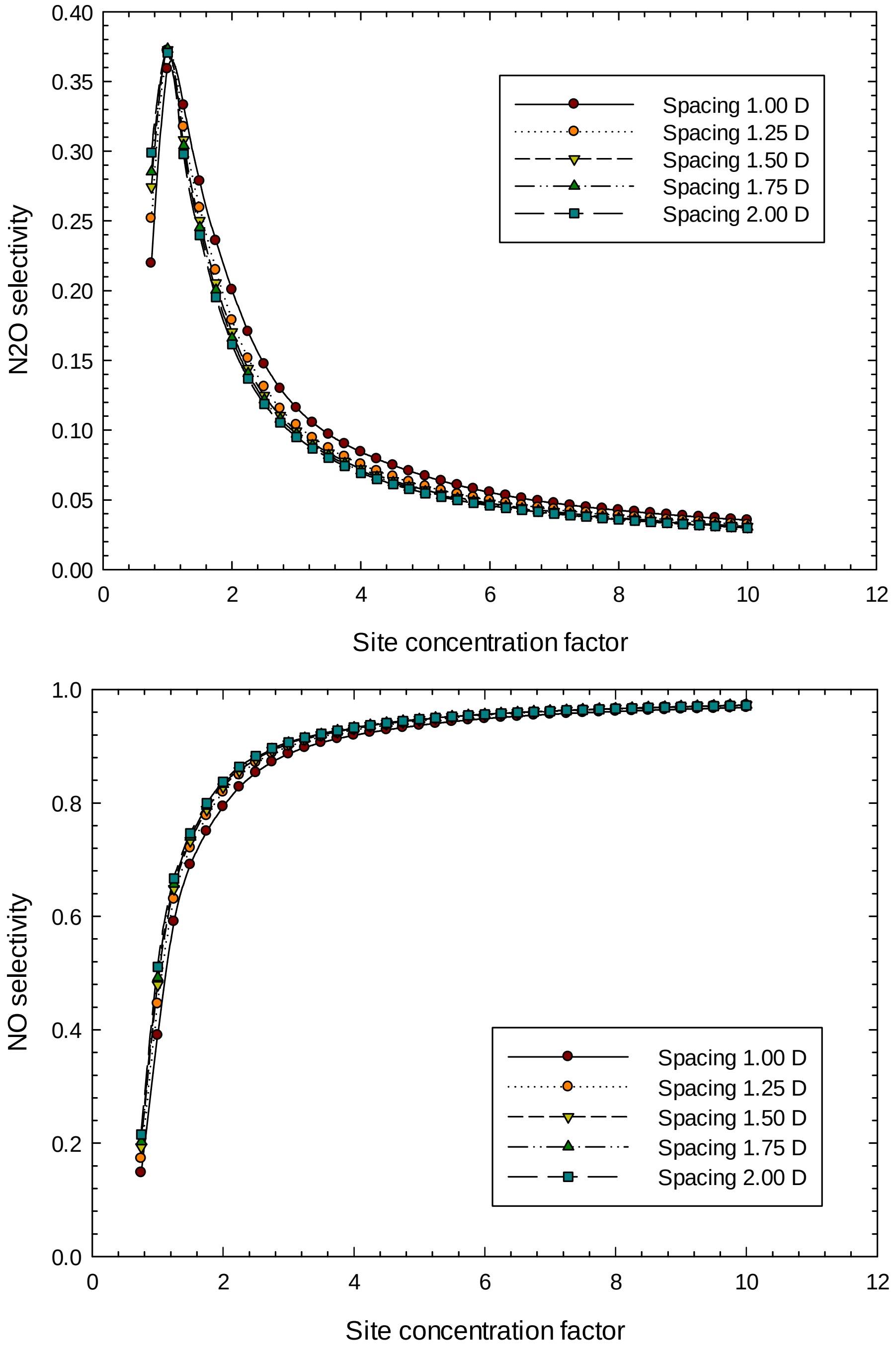

Figure 5.30 – Selectivity to N_2O (top) and NO (bottom) as a function of catalyst activity and wire spacing for the case of a single screen. The wire diameter was 0.10 mm.

5.3.4 3D multiple wire parametric study.

In this section we show the results obtained from six screens of two wires each (total of 12 wires) that are arranged in a staggered arrangement, see Figure 5.27. We present a series of results from a parametric study of this geometry. The wire diameter was fixed at either 0.05 or 0.10 mm, and the wire separation (distance *L*) was varied between one and two wire diameters. The site density range was 1 to 10 as before.

Figure 5.31 shows a colour contour plot of selectivity for the case of 0.100 mm diameter wire for a wire spacing of 0.175 mm and a site factor of 10. The plot clearly shows regions of high and low selectivity. Figure 5.32 then shows the conversion of ammonia as a function of activity and wire spacing. Figure 5.33 gives the details of the selectivity to N_2O and NO for the range of wire spacing and catalyst activity.

The next set of figures shows the performance for the six gauzes when the wire diameter is 0.05 mm. Figure 5.34 shows a colour contour plot of selectivity for the case of 0.050 mm diameter wire for a wire spacing of 0.175 mm and a site factor of 10. The plot clearly shows regions of high and low selectivity. Figure 5.35 then shows the conversion of ammonia as a function of activity and wire spacing. Figure 5.36 gives the details of the selectivity to N_2O and NO for the range of wire spacing and catalyst activity. The trends are the same as before.

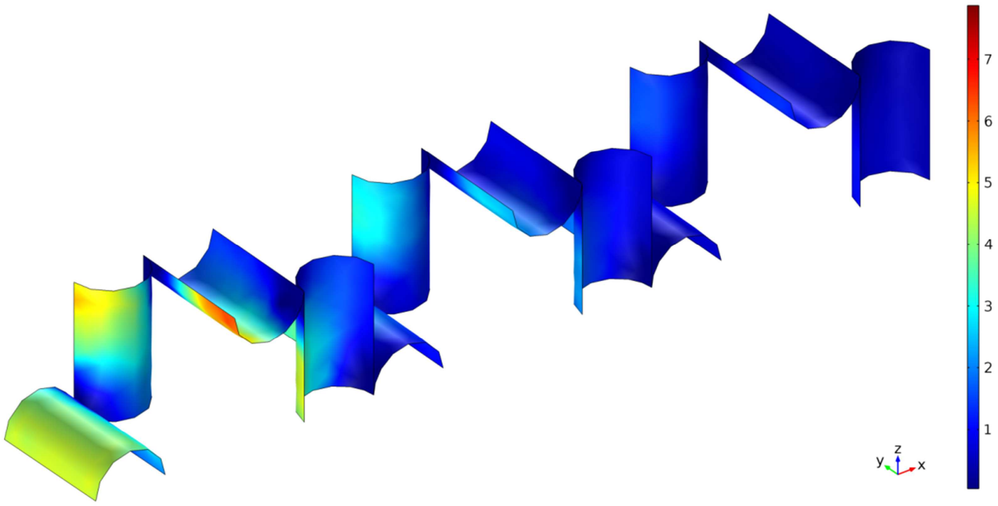

Figure 5.31 - Contour plot of selectivity for the case of 0.100 mm diameter wire for a wire spacing of 0.175 mm and a site factor of 10. The plot clearly shows regions of high and low selectivity.

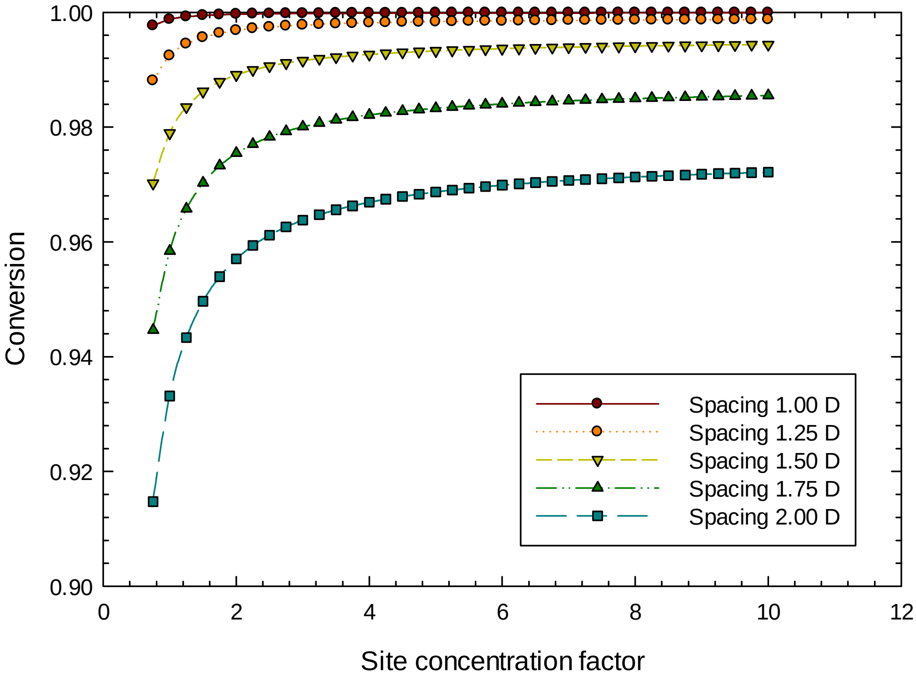

Figure 5.32 - Conversion of ammonia as a function of activity and wire spacing for a 0.10 mm wire diameter.

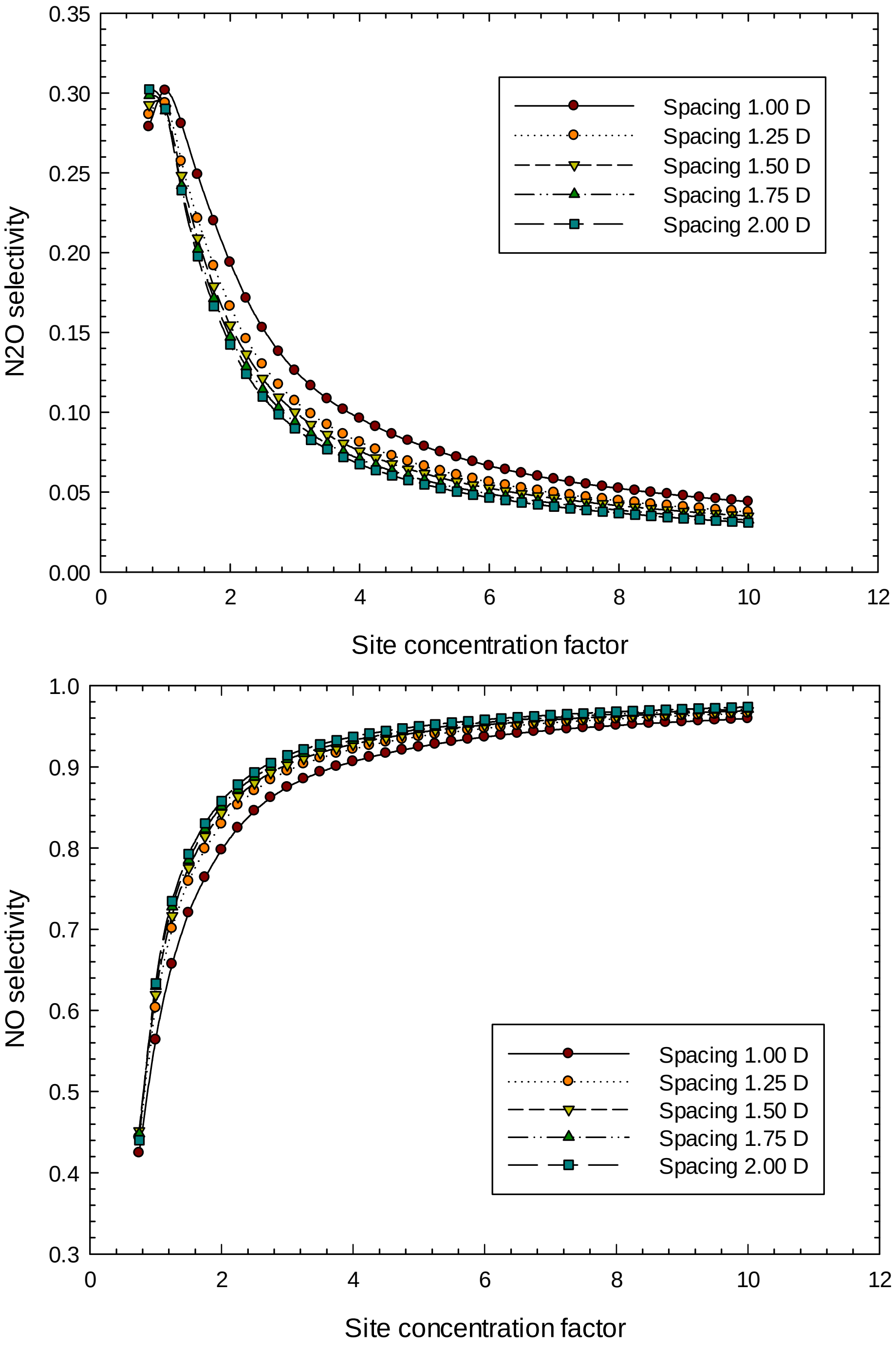

Figure 5.33 – Selectivity to N_2O (top) and NO (bottom) as a function of catalyst activity and wire spacing for the case of six screens. The wire diameter was 0.10 mm.

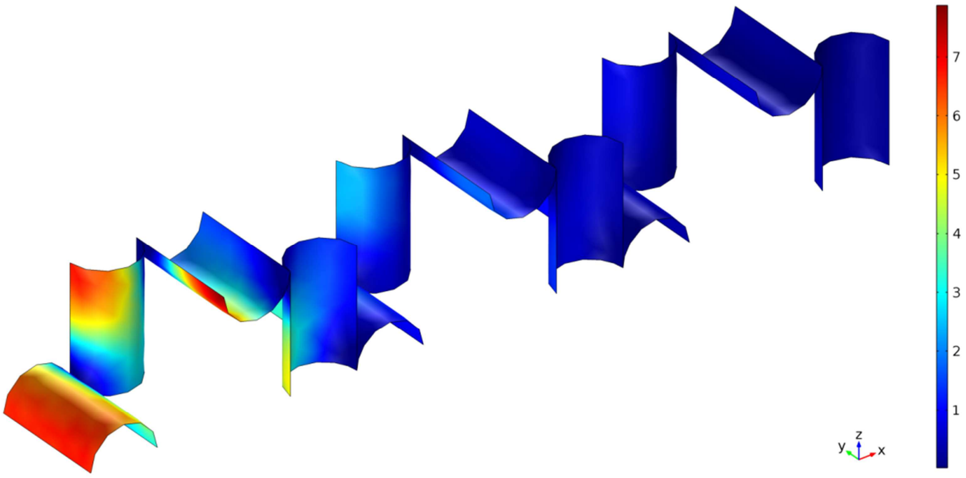

Figure 5.34 - Contour plot of selectivity for the case of 0.050 mm diameter wire for a wire spacing of 0.175 mm and a site factor of 10. The plot clearly shows regions of high and low selectivity.

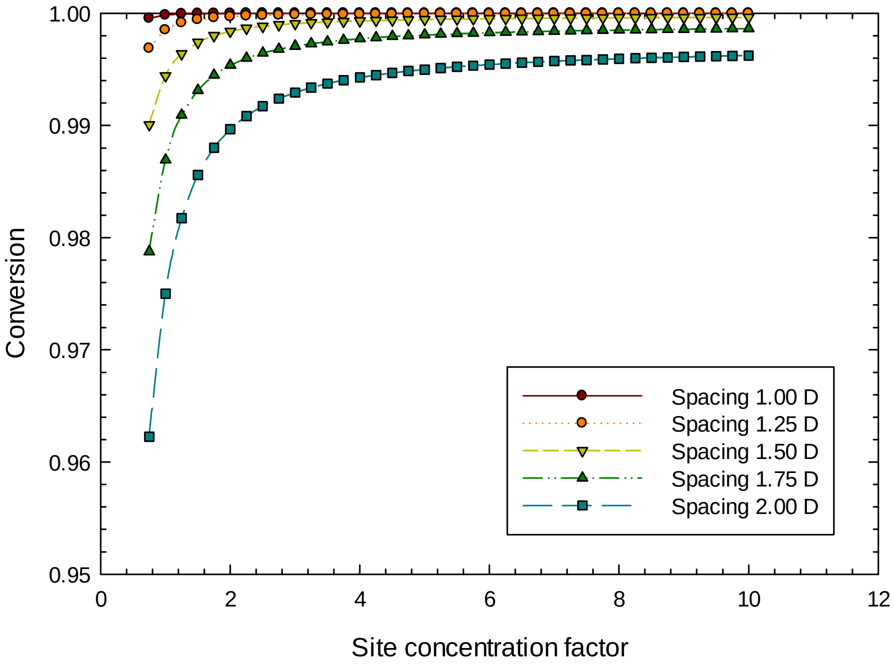

Figure 5.35 - Conversion of ammonia as a function of activity and wire spacing for a 0.05 mm wire diameter.

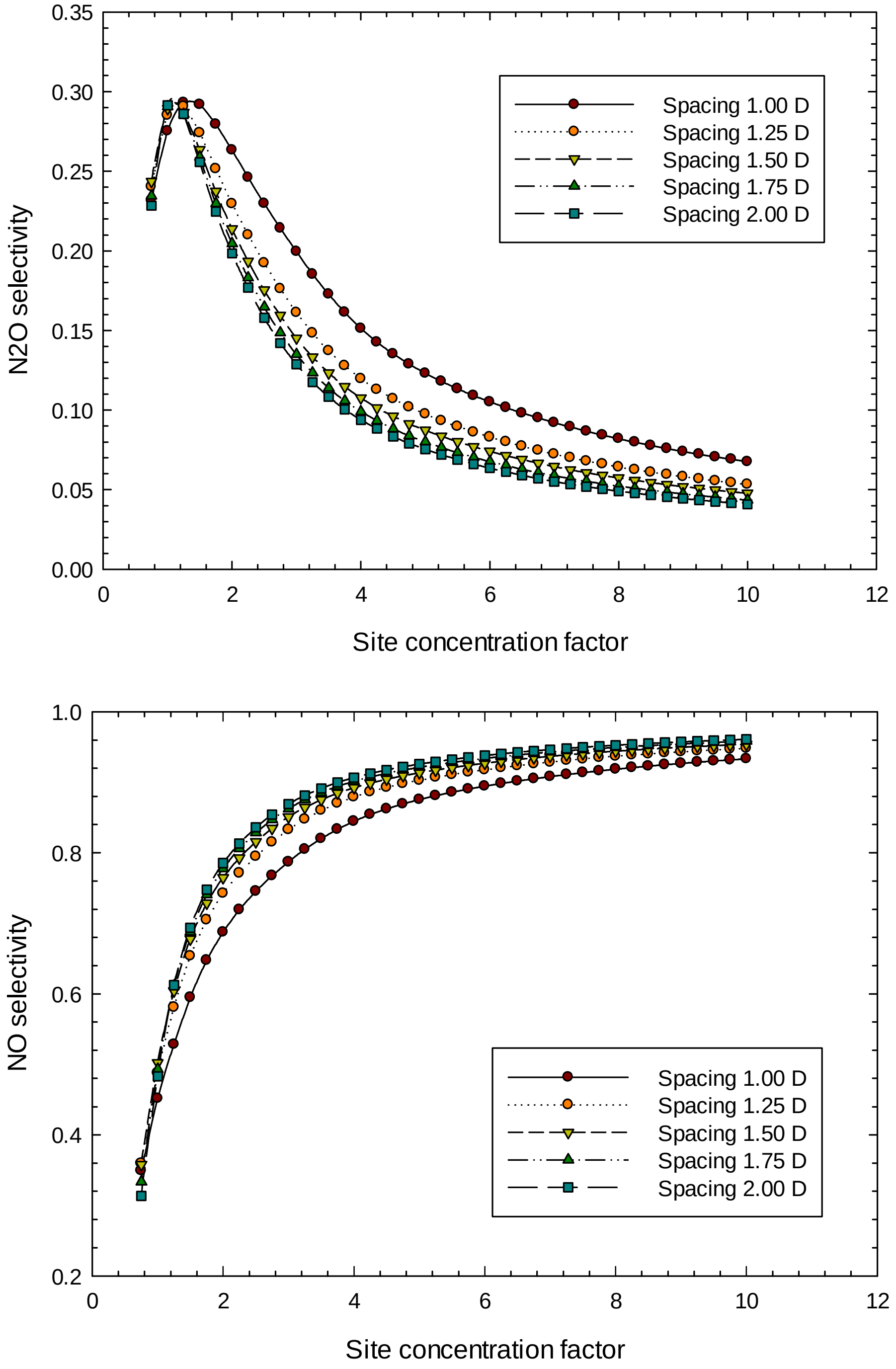

Figure 5.36 – Selectivity to N_2O (top) and NO (bottom) as a function of catalyst activity and wire spacing for the case of six screens. The wire diameter was 0.05 mm.

5.4 Look-up table validation

In this section we compare the results from the look-up table to the chemistry module. Figure 5.37 shows a colour contour plot for the 2D five wire staggered arrangement. The mole fractions of ammonia are shown, and the results are virtually indistinguishable. The minimum mole fraction of NH_3 was $2.7217\text{x}10^{-3}$ for the chemistry module and $2.7322\text{x}10^{-3}$ for the lookup table. The relative error is about 0.3% which is acceptable. The execution time was about one hour with the chemistry module and about one minute with the look-up table.

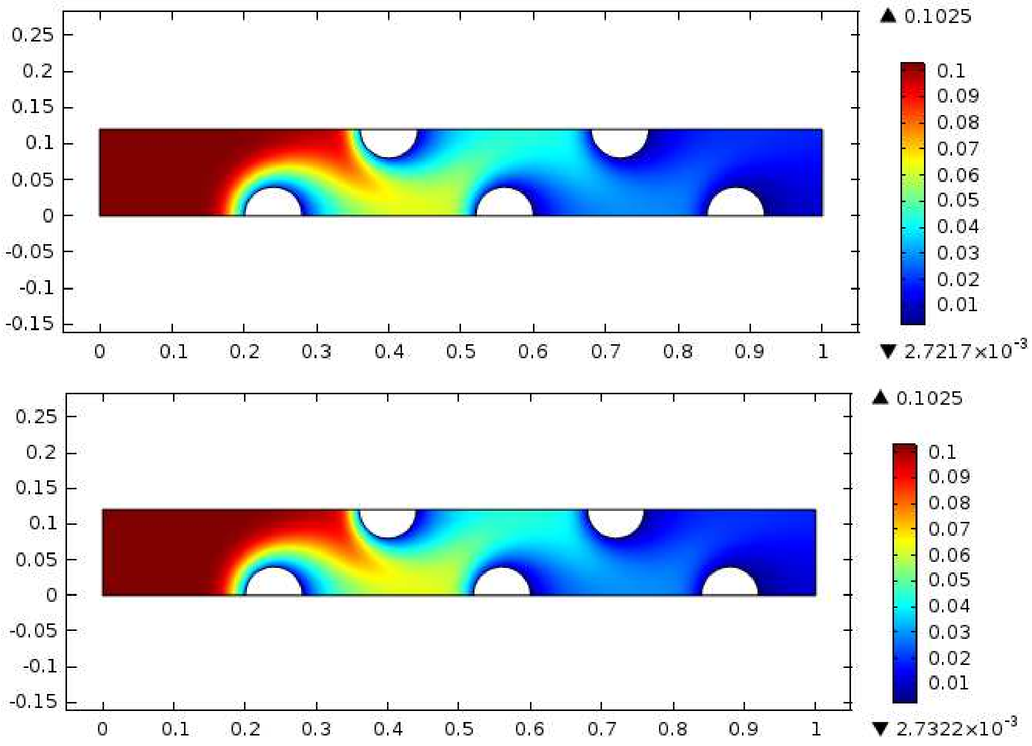

Figure 5.37 – Contour plots of ammonia mole fraction for the chemistry module (top) and the look-up table (bottom). The results are essentially the same.

5.5 Conclusions

In this chapter, we have developed a detailed, fully discrete, mathematical model for a gauze reactor used for the catalytic oxidation of NH_3. By using pre-computed rate data stored in a lookup table, it was possible to use a detailed mechanistic model which can give a guide to the product distribution. In particular, the execution of full three dimensional simulations was very time consuming if this table was not used. With these tools developed, we have the ability to perform detailed and realistic CFD studies of the gauze reactor. Such operating parameters as the gauze design, number of layers, mesh design, etc can be investigated.

It has been shown that the selectivity is a strong function of the geometry of the wires. Not only does the selectivity vary from wire to wire in the multiple wire case, but it also varies around the perimeter of the wire. In three dimensional simulations it was also seen that selectivity varies along the length of the wire.

It is clear from these results that shape optimization can be used to determine a wire shape and gauze arrangement that could give some ideas on how to minimize the emissions of N_2O. A serious consideration of gauze design could therefore be extremely beneficial.

Nomenclature

C_P	constant pressure heat capacity, J/(mol·K)
D_{ij}	binary diffusion coefficient, m^2/s
D_i^m	diffusion coefficient of *i* in mixture, m^2/s
$\left(\Delta H^0{}_R\right)_i$	enthalpy of reaction, J/mol
k	thermal conductivity, W/(m·K)
M	molar mass, g/mol
P	pressure, Pa
S	selectivity, dimensionless
T	temperature, K
u	velocity, m/s
w	mass fraction
x	mole fraction

Greek symbols

ν	diffusion volume of a species
ρ	density, kg/m^3
μ	viscosity, Pa·s

References

Ahlstrom-Silversand, A.F., Odenbrand, C.U.I., Modelling catalytic combustion of carbon monoxide and hydrocarbons over catalytically active wire meshes, Chem. Eng. J., 73 (1999) 205-216.

Amiri, S., Hayes, R.E., Nandakumar, K., Sarkar, P. , Modelling heat transfer for a tubular micro-solid oxide fuel cell with experimental validation, Journal of Power Sources, 233 (2013) 190-201.

Behnam, M., Dixon, A.G., Nijemeisland,M., Stitt, E.H., Catalyst deactivation in 3D CFD resolved particle simulations of propane dehydrogenation, Ind. Eng. Chem. Res. 49 (2010) 10641-10650

.L.J. Broadbelt, R.Q. Snurr, Applications of molecular modeling in heterogeneous catalysis research, Applied Catalysis A. 200 (2000) 23-46.

Dixon, A.G., Nijemeisland,M., Stitt, E.H., Packed tubular reactor modeling and catalyst design using computational fluid dynamics, Advances Chemical Engineering, 31 (2006) 307-389.

Dixon, A.G., Taskin, M.E., Nijemeisland,M., Stitt, E.H., CFD method to couple three-dimensional transport and reaction inside catalyst particles to the fixed flow field, Ind. Eng. Chem. Res. 49 (2010) 9012-9025.

Dumesic, J.A., Rudd, D.F., Aparicio, L.M. Rekoske, J.E., Trevino, A.A. The Microkinetics of Heterogeneous Catalysis, ACS, Washington, 1993.

Hannevold L., Nilsen O; Kjekshus, A; Fjellvåg, H. Reconstruction of platinum-rhodium catalysis during oxidation of ammonia. Applied Catalysis A: General 284 (2005). 163-176.

Fuller, E., Schettler, P., Giddings, J.C., A new method for prediction of binary gas-phase diffusion coefficients. Industrial & Engineering Chemistry 58, 18–27, 1966.

Heck, R.M. Farrauto, R.J. Gulati, S.T., Catalytic Air Pollution Control, Commercial Technology, Wiley, New York, 2009.

Hickman, D.A., Schmidt, L., Modeling catalytic gauze reactors: Ammonia oxidation, Ind. Eng. Chem. Res. 30 (1991) 50-55.

Hills T., Kons, G., Schwab, E., Mueller-Everbush, M., Knitted metal fabrics as thin layer atalysts: operational experience in a steamcracker gas phase hydrogenation. ICOSCAR2, Delft, 2005.

Imbhil, R., Scheibe, A. , Zeng, Y.F. Gunther, S., Kraehnert, R., Kondratenko, V.A. Baerns, M., Offermans, W.K., Jansen, A.P.J. Santen, R.A., Catalytic oxidation on platinum: mechanism and catalyst restructuring at high and low pressure, Physical Chemistry Chemical Physics, 9 (2007) 3522-3540.

Kolodziej, A., Jaroszynski, M., Janus, B., Kleszcz, T., Lojeswka, J., Lojeswka, T., An experimental study of the pressure drop in fluid flows through wire gauzes, Chem. Eng. Commun., 196 (2009) 932-949.

Kolodziej, A., Lojeswka, J., Experimental and modelling study on flow resistance of wire gauzes, Chem. Eng. and Processing: Process intensification, 48 (2008) 816-822.

Kolodziej, A., Lojeswka, J., Flow resistance of wire gauzes, AIChE Journal, 55 (2009) 264-267.

Kolodziej, A., J. Lojewska, M. Jaroszyäski, A. Gancarczyk, and P. Jodéowski. Heat transfer and flow resistance for stacked wire gauzes: Experiments and modelling. International Journal of Heat and Fluid Flow 33 (2012) 101-108.

Kondratenko, V.A., Baerns, M., Mechanistic insights into the formation of N2O and N2 in NO reduction by NH3 over a polycrystalline platinum catalyst. Applied Catalysis B. Environmental 70 (2007) 111-118.

Kopperud, T., Nitrous Oxide Greenhouse Gas Abatement Catalyst. Platinum Metals Rev. 50 (2006), 50, 2.

Krahnert R, Baerns M., Kinetics of ammonia oxidation over Pt foil studied in a micro-structured quartz-reactor. Chem Eng Journal 137 (2008) 361–375

Lyubvsky, M., Karim, H., Menacherry, P., Boorse, S. LaPierre, R., Pfefferle, W.C., Roychoudhury, S., Complete and partial catalytic oxidation of methane over substrates with enhanced transport properties, Catalysis Today, 83 (2003) 183-197.

Nien, T., Mmbaga, J.P., Hayes, R.E. Votsmeier, M. Hierarchical multi-scale model reduction in the simulation of catalytic converters. Catalysis Today 93 (2013) 362-375

Nilsen O., Kjekshus A., Fjellvåg H. Reconstruction and loss of platinum catalyst during oxidation of ammonia. Applied Catalysis A: General 207 (2001) 43–54

Pérez-Ramırez, J. Kapteijn, F. Schöffel, K. Moulijn, J.A. . Applied Catalysis B: Environmental 44 (2003) 117-151.

Perry and Green, Chemical Engineering Handbook, 7th Edition, McGraw-Hill, New York, 1984.

Quiceno R, Deutschmann O, Warnatz J, Perez-Ramirez J.. Rational modeling of the CPO of methane over platinum gauze Elementary gas-phase and surface mechanisms coupled with flow simulations. Catalysis Today 119 (2007) 311–316

Ranade, V.V., Computational flow modelling for chemical reactor engineering, (2001), Academic Press, New York.

Scheuer, A., Hirsch, O., Hayes, R.E., Vogel, H., Votsmeier, M.,, Efficient simulation of an ammonia oxidation reactor using a solution mapping approach, Catalysis Today, 175 (2011) 141-146.

Scheuer, A., Votsmeier, M., Schuler, A., Gieshoff, J., Drochner, A., Vogel, H. . NH_3-slip catalysts: Experiments versus mechanistic modelling**.** Topics in Catalysis. 52 (2009) 1847-1851.

Taylor, R., Krishna, R., Multicomponent mass transfer, John Wiley and Sons, New York, 1993.

Vanchurin,V.I.; Golovnya,E.V.; Yashchenko,A.V.. Oxidation of ammonia on woven and knitted platinoid gauzes. Catalysis today. 4 (2012) 105-109

Votsmeier, M.,. Efficient implementation of detailed surface chemistry into reactor models using mapped rate data. Chemical Engineering Science 64 (2009) 1384–1389.

Votsmeier, M., Scheuer, A., Drochner, A., Vogel, H., Gieshoff, J., Simulation of automotive NH_3 oxidation catalysts based on pre-computed rate data from mechanistic surface kinetics, Catalysis Today, 151 (2010) 271-277.

Waletzko, N., Schmidt, L.D., Modelling catalytic gauze reactors: HCN synthesis, AIChE Journal, 34 (1988) 1146-1156.

Chapter 6:

Conclusions and Recommendations

6.1 Summary

The focus of this thesis is on the use of look-up tables for the multi-scale modelling of heterogeneous catalytic reactors. It is been shown that by appropriate selection of sub-model for complex kinetics, or heat and mass transfer phenomena, considerable reductions in computational cost can be achieved without significant loss of accuracy. Thus in Chapter 2 it was seen that using a hierarchical approach for model reduction in a catalytic converter, it was possible to retain complex information about the smaller spatial scales in full scale reactor models. Cost savings of orders of magnitude can be achieved. Some of the more complex simulations can simply not be achieved using classical computing algorithms. In Chapters 3 and 4 two applications of catalytic converters were examined using the principles expounded in Chapter 2. In Chapter 5, another type of structured reactor was examined, the gauze reactor for ammonia oxidation. In this case, a slightly more complicated look-up table was developed to model the various reactions that occur in this system, and to study the effects of geometry on the selectivity of the reaction. It has been shown that the selectivity is indeed a strong function of geometry, and this finding is expected to lead to a major new research direction.

6.2 Recommendations and future direction

The power of the look-up table has been shown. One drawback of this method is that the size of the look-up table grows significantly as the number of dimensions increases. For the work presented here, the maximum size of the look-up table was four dimensions, and it was possible to obtain sufficient accuracy with a reasonably sized table. As the number of dimensions increases, the memory requirement also increases dramatically. During the course of this work, look-up tables were built with dimensions of six or seven which is possible with about 64

GB of RAM, however, it can also take a long time to build the table as the number of simulations required increases. It is recommended that for larger tables, the use of Matlab be avoided, and the splining function be written in a language such as Fortran. The use of parallel systems may also be advantageous for the construction of larger systems.

Appendix A:

Example

Here is an example of the smallest lookup table [2 2 2 2] in Chapter 2.
First, the following equation shows one-variable piecewise polynomial form of a spline of order k.

$$p_j(x) = \sum_{i=1}^{k} \left(x - \xi_j\right)^{k-i} c_{ji},\ j = 1:l$$

It provides a description in terms of its breaks $\xi_l \cdots \xi_{l+1}$ and the local polynomial coefficients c_{ij} of its l pieces.

In Chapter 2, there are four variables so that multivariate tensor product is used to evaluate.

$$F_{j_1,\cdots,j_m}(x_1,\cdots,x_m) = \prod_{i=1}^{m} p_{i,j_i}(x_i)$$

$F_{j_1,\cdots,j_m}$ is the objective value (i.e. reaction rate for lookup table T1) obtained by the polynomial, and j is the order of the spline method.

$$p_{m,j}(x) = \sum_{i=1}^{k_m} \left(x_m - \xi_{m,j}\right)^{k_m-i} c_{m,j,i}$$

In the simplest case, $m = 4$; $k_1 = k_2 = k_3 = k_4 = 2$ for linear spline. $j = 1$

$$\phi_i = \left(x_i - \xi_{i,j}\right)$$

$$\begin{aligned}&F_{1,1,1,1}(x_1,x_2,x_3,x_4) = \\ &c'(1)\phi_1\phi_2\phi_3\phi_4 + c'(2)\phi_2\phi_3\phi_4 + c'(3)\phi_1\phi_3\phi_4 + c'(4)\phi_3\phi_4 + c'(5)\phi_1\phi_2\phi_4 + c'(6)\phi_2\phi_4 \\ &+c'(7)\phi_1\phi_4 + c'(8)\phi_4 + c'(9)\phi_1\phi_2\phi_3 + c'(10)\phi_2\phi_3 + c'(11)\phi_1\phi_3 + c'(12)\phi_3 + \\ &c'(13)\phi_1\phi_2 + c'(14)\phi_2 + c'(15)\phi_1 + c'(16)\end{aligned}$$

The coefficients obtained by MATLAB spline toolbox are shown in Table A.1

Table A.1 The 16 terms of the smallest lookup table T1 in Chapter 2

$c'(1:16)$	
-1.7491E-01	$\phi_1\phi_2\phi_3\phi_4$
9.3410E-06	$\phi_2\phi_3\phi_4$
2.6350E+00	$\phi_1\phi_3\phi_4$
-1.4766E-04	$\phi_3\phi_4$
9.5038E-01	$\phi_1\phi_2\phi_4$
-4.2265E-05	$\phi_2\phi_4$
-1.7868E+01	$\phi_1\phi_4$
-5.0682E-04	ϕ_4
6.2143E+01	$\phi_1\phi_2\phi_3$
1.4490E-02	$\phi_2\phi_3$
-9.9615E+02	$\phi_1\phi_3$
-2.9771E-01	ϕ_3
-3.5359E+02	$\phi_1\phi_2$
9.1427E-01	ϕ_2
-1.2126E+04	ϕ_1
-2.0264E+01	1